

Rheology of some fluid extreme composites

Such as fresh self-compacting concrete



Lauge Fuglsang Nielsen
 Associate professor, Ph.D.
 Department of Civil Engineering, Building 118
 Technical University of Denmark
 DK-2800 Lyngby, Denmark
 E-mail: lfn@byg.dtu.dk

ABSTRACT

A method is developed by which the well-known Bingham description of flow in homogeneous liquids with yield stress is generalised to apply also for composite fluids. In the present context such fluids are defined as fluids mixed with very stiff particles of known shapes and size distributions.

In practice the composite aspects of the generalised Bingham description is a major advantage. Only three geometrical parameters for the particles and two material properties for the fluid matrix are required in order to describe the generalised Bingham behaviour of any composition of the composite fluid considered. The Bingham method normally used needs experimental calibration for any new composition.

Finally, it is indicated how the analysis presented can easily be generalised to apply also for composite fluids with soft particles (voids). This feature might be useful when tailoring the viscosity of SCC, for example by modifying the matrix properties by air entrainment.

Key words: Composite fluid, Bingham, Composite Bingham, Self-compacting concrete (SCC)

1. INTRODUCTION

This paper is part of an on-going project (1,2,3,4,18) on Self-Compacting Concrete (SCC) at the Department of Civil Engineering, Technical University of Denmark. The particular scope of the paper is to look at possibilities of establishing a composite method of predicting the rheology of SCC, which may serve as an alternative to the semi-empirical method, suggested by deLarrard (5). To the author's knowledge such approach has not yet been presented.

Composite fluids are considered mixtures of very stiff elastic particles (phase P) in a Maxwell fluid matrix (phase S). The basic shear stress-strain relations of the components are presented in Equation 1 where the rigidity and viscosity of the fluid are G_S and η_S respectively. The rigidity of the particle phase is denoted by G_P . Shear stress and strain are denoted by s and e respectively. The stress-strain relation for the fluid presented in Equation 1 is consistent with a similar expression

presented by Reiner (6).

$$\frac{de}{dt} = \frac{ds/dt}{2G_S} + \frac{s}{2\eta_S} \quad \text{Phase S : Maxwell fluid} \quad (1)$$

$$e = \frac{s}{2G_P} \quad \text{Phase P : Hooke solid}$$

Equation 2 defines the volume concentration of particles in composites considered with volumes denoted by V. In general subscripts P and S refer to particle phase and matrix phase S respectively. A complete list of symbols is presented at the end of this paper.

$$c = \frac{V_P}{V_P + V_S} \quad \text{Volume concentration of particles} \quad (2)$$

2. COMPOSITE FLUID

It can be shown by a composite theory developed in (7,8) that a Maxwell fluid with very stiff particles added will act as a Maxwell fluid itself. The constitutive equation becomes Equation 3 with particles influencing the composite properties (G and η) as described in Equation 4. The average phase P stress (s_P) and average phase S stress (s_S) are presented in Equation 5. (The theoretical steps to obtain these results are summarised in the Appendix at the end of this paper).

$$\frac{de}{dt} = \frac{ds/dt}{2G} + \frac{s}{2\eta} \quad \text{Composite Maxwell fluid with } G_P \gg G_S \quad (3)$$

$$\frac{\eta}{\eta_S} = \frac{G}{G_S} = \frac{1 + \gamma_\infty c}{1 - c} \quad \text{with } \gamma_\infty = \begin{cases} \frac{3}{2} \frac{\mu_P + \mu_S - 1}{\mu_S} & c < c_S \\ \infty & c > c_S \end{cases} \quad (4)$$

$$\frac{s_P}{s} = \frac{1 + \gamma_\infty}{1 + c \gamma_\infty}, \quad \frac{s_S}{s} = \frac{1}{1 + c \gamma_\infty} \quad (5)$$

The composite geometry (particle shape and size distribution) is considered by the so-called geometry function (γ_∞) and shape functions (μ_P, μ_S), explained and determined in the Appendix. Principal parameters for the description of geometry in this paper are aspect ratio (A = length/diameter) and the critical concentration c_S of ellipsoidal particles considered ($c_S \approx$ maximum packing density \approx eigenpacking). Normally, we may expect improved quality of particle size distribution (smoothness and density) to be associated with higher c_S . An extra parameter, the so-called interaction power, M, is used in the Appendix to consider the interaction between particles. If not otherwise stated M = 1 (moderate interaction) is assumed.

2.1 Composite Newton fluid

The stress-strain relation for a so-called composite Newton fluid is obtained from the Maxwell solution letting the rigidity G_S approach infinity. The result is presented in Equation 6 with viscosity and stresses kept as expressed by Equations 4 and 5 respectively.

$$\frac{de}{dt} = \frac{s}{2\eta} \quad \text{composite Newton fluid } (G_S \rightarrow \infty \Rightarrow G \rightarrow \infty) \quad (6)$$

2.2 Composite Bingham fluid

Homogeneous Newton fluids were considered by Bingham (10) who suggested that viscous behaviour first appears when stress has become greater than a certain so-called yield stress S . We adopt the idea of Bingham's in the following way: Viscous behaviour of the composite Newton liquid first appears when the matrix stress (s_s in Equation 5) exceeds the matrix yield stress S_s . Then Equation 6 becomes modified as shown in Equation 7 with viscosities kept as expressed by Equation 4. Formally the original- and the generalised Bingham expression look alike.

$$\frac{de}{dt} = \frac{s - S}{2\eta} \Rightarrow s = S + 2\eta \frac{de}{dt} \quad \text{composite Bingham fluid with} \quad (7)$$

$$\text{Yield stress : } S = S_s(1 + \gamma_\infty c) \quad \text{and} \quad \text{Viscosity : } \eta = \eta_s \frac{1 + \gamma_\infty c}{1 - c}$$

Curiosum: The relative viscosity predicted by Equation 4 agrees with Equation 8 developed by Einstein (11) in his study of the viscosity of dilute sugar solutions. The expression also agrees with data obtained from experiments on mixtures made of fluids with finite particle concentrations. Two empirical descriptions (Eilers and Brinkman) for such data are presented in Equation 9 reproduced from (12,13). In Figure 1 the latter results are compared graphically with the results obtained by the present theory. In Figure 2 is shown, additionally, how relative yield stress predicted by Equation 7 varies with particle concentrations.

$$\frac{\eta}{\eta_s} = 1 + 2.5c \quad \text{dilute solution with spherical particles} \quad (8)$$

$$\frac{\eta}{\eta_s} = \begin{cases} \left(1 + \frac{1.25c}{1 - 1.28c}\right)^2 & \text{Eilers} \\ (1 - c)^{-5/2} & \text{Brinkman} \end{cases} \quad \text{spherical particles} \quad (9)$$

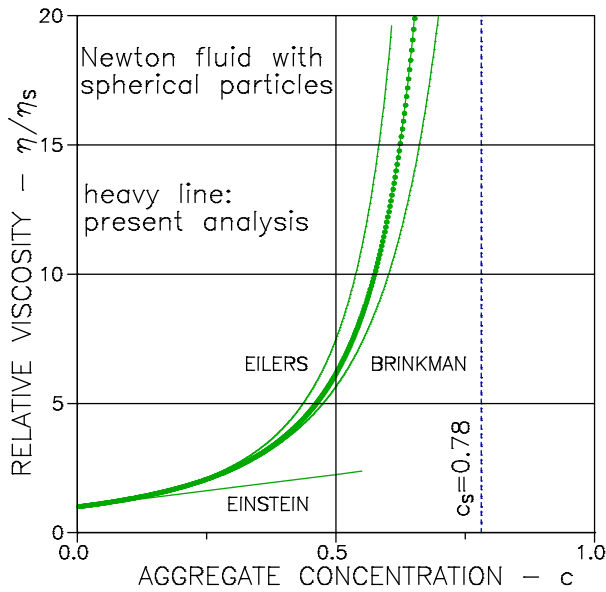


Figure 1. Spherical particles ($A = 1$) in a viscous matrix. Present analysis and empirical descriptions by Eilers and Brinkman.

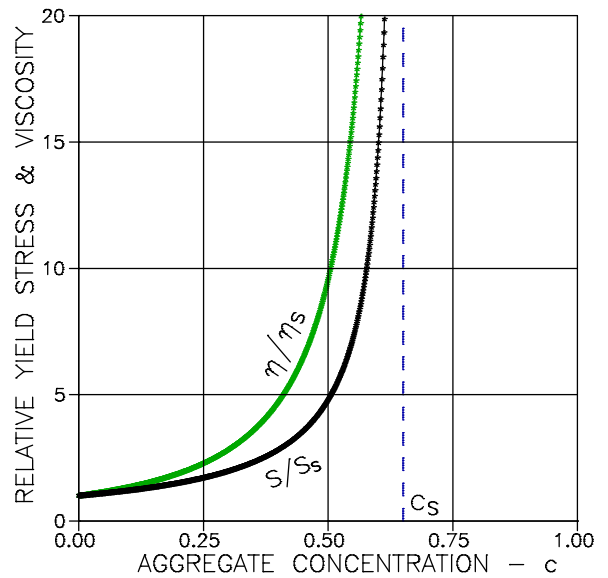


Figure 2. Relative quantities of composite viscosity and yield stress. Aggregates: $(A, c_s) = (2, 0.65)$.

3. ILLUSTRATIVE EXAMPLES

The theoretical influence of ellipsoidal particle shapes and quality of size distributions on the rheology of SCC are illustrated in the following Figures 3 - 6. All composites are assumed to have a mortar (phase S) with a viscosity of $\eta_S = 2.5 \text{ Pa}\cdot\text{sec}$ and a yield stress of $S_S = 1.0 \text{ Pa}$. In the analysis of both viscosity and yield stress it is assumed that interaction is moderate ($M = 1$).

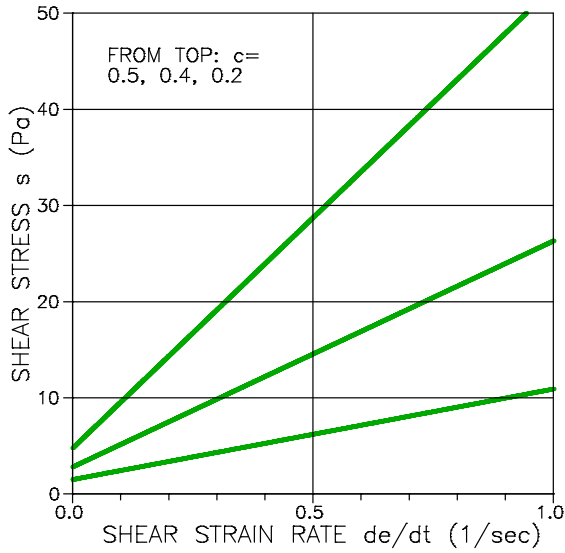


Figure 3. Composite Bingham material with various contents of aggregates with $A = 2$. Well graded with $c_S = 0.65$.

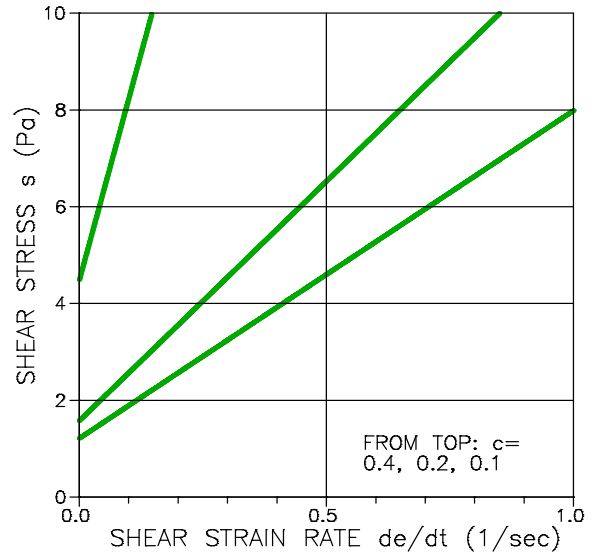


Figure 4. Composite Bingham material with various contents of aggregates with $A = 2$. Badly graded with $c_S = 0.5$.

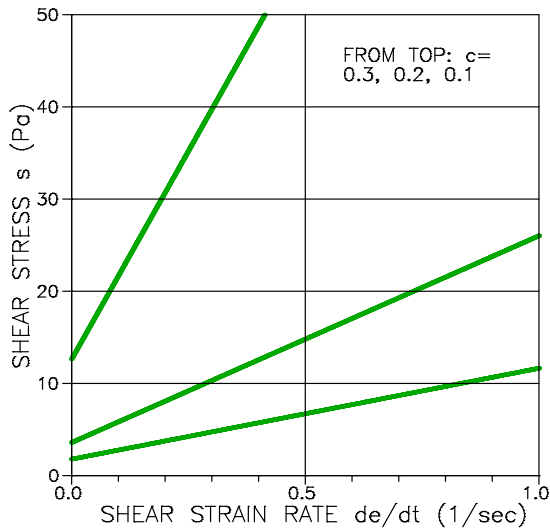


Figure 5. Composite Bingham material with various contents of aggregates with $A = 10$. Well graded with $c_S = 0.35$.

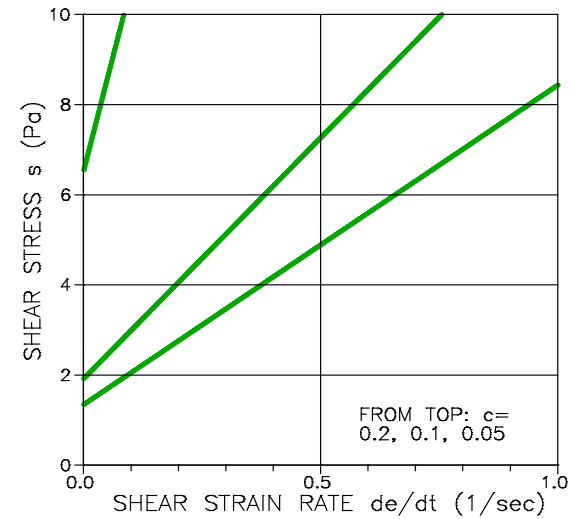


Figure 6. Composite Bingham material with various contents of aggregates with $A = 10$. Badly graded with $c_S = 0.25$.

Discussion

It is observed from Figures 3 - 6 that a particle aspect ratio increasingly different from $A = 1$ (spheres) and a bad particle size distribution (lower c_s) increase viscosity and yield stress of composites. These deductions agree with experimental observations made in (3). Also observed in (3) is that normalised viscosity varies as presented in Figure 2.

4. CALIBRATION

As previously mentioned the particles primarily assumed in this paper are smooth ellipsoidal particles. Recognizing that this assumption is not very realistic in practice, we must accept that geometrical information on particles must be determined by calibration with experimental data. In this section it is shown where theoretical modifications can be made without hurting the basic idea of a sound composite approach to the rheological quantification of particulate fluids. Obviously, the targets of calibration are the shape quantifications: 1) Shape factors and 2) Shape functions.

1) Other shape factors than for ellipsoidal particles can be calculated as demonstrated in (2, Fig. 2). Mixtures involving a variety of aspect ratios are considered in (9). In the present theoretical presentation, however, we suggest that shape deviations from ellipsoidal can be calibrated using Equation A4 with a simple multiplication of an aspect ratio A , estimated from particles averaged to be ellipsoidal.

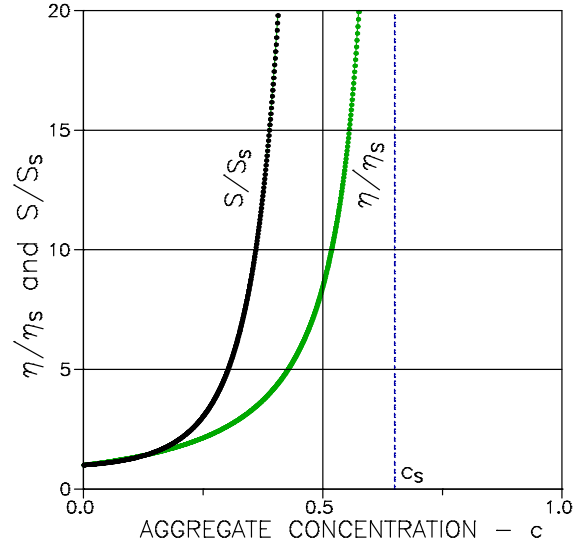


Figure 7. Normalised viscosity (with $M_v = 1$) and normalised yield stress (with $M_s = 3.5$). $(A, c_s) = (1, 0.65)$

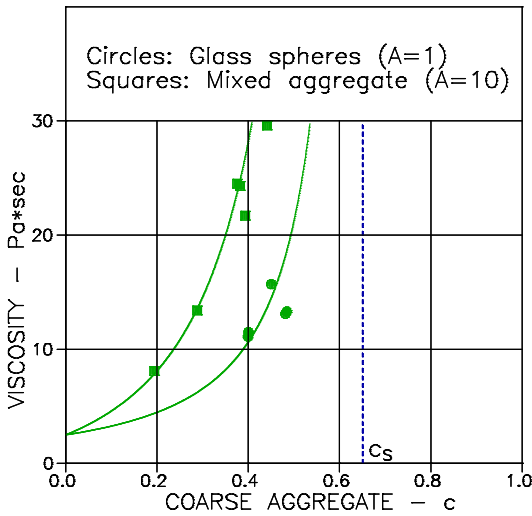


Figure 8. Viscosity of concrete as related to volume fraction of coarse aggregates (18). Solid lines are predicted with $M_v = 1$. Mortar viscosity is $\eta_s = 2.5 \text{ Pa}\cdot\text{sec}$. $c_s = 0.65$.

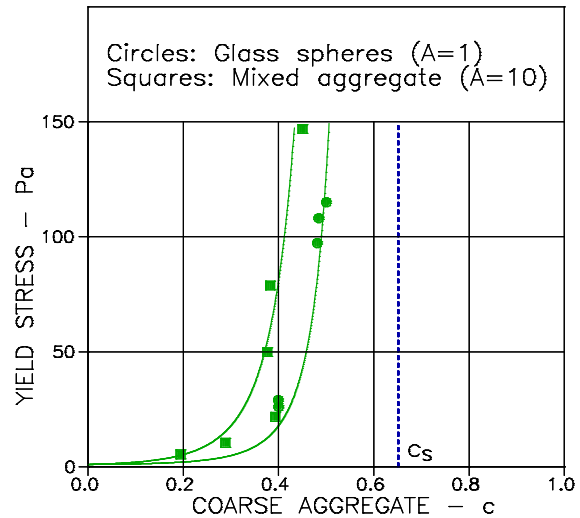


Figure 9. Yield stress of concrete as related to volume fraction of coarse aggregates (18). Solid lines are predicted with $M_s = 3.5$. Mortar yield stress is $S_s = 1 \text{ Pa}$. $c_s = 0.65$.

2) As previously indicated in Chapter 2 we have, until now considered interaction between particles to be moderate ($M = 1$). Higher or lower states of interaction can be considered with $M > 1$ and $M < 1$ respectively (see Appendix). We must expect that different M s may apply when viscosity and when yield stress respectively are considered. Interaction may be different between moving and not moving aggregates. We introduce M_S and M_V for interaction powers applying in yield stress analysis and in viscosity analysis respectively.

It is demonstrated, comparing Figures 2 and 7, how relative viscosity and relative yield stress reverse their orders of magnitudes by increasing the interaction power (M_S) in the yield stress analysis. Incidentally, Figure 7 compares positively with experimental data reported in (3).

Remark: As previously indicated, the present paper is part of an on-going SCC project at the Technical University of Denmark. A parallel experimental study has been made on the influence of coarse aggregates on the rheology of fresh concrete. A prime purpose of this study has been to investigate the applicability of the model developed in this paper. The study is reported in (18) from which Figures 8 and 9 are reproduced. The aspect ratios (A) and the interaction powers (M) used are calibrated in (18) according to the considerations made above.

5. FINAL REMARKS

The well-known Bingham description of the rheology of homogeneous fluids has been generalised in this paper also to include the rheological description of composite fluids. The advantage of such generalisation is obvious: With three parameters (shape factor μ_P^0 , packing density c_S , and interaction power M) to describe the composite geometry, only two material properties (viscosity η_S , and yield stress S_S) of the fluid matrix are required to describe the generalised Bingham behaviour at any composition of the composite fluid considered. The traditional Bingham model needs experimental calibration for any new composition considered. It is worthwhile noticing that shapes and size distribution of particles are considered by the three geometrical parameters mentioned.

The theory presented in this paper is based on global solutions for the mechanical/physical behavior of composite materials with any isotropic geometry. A numerical quantification of specific composite geometries is needed in this analysis, which is, at the present, most accurately developed for particulate composites with ellipsoidal particles. Recognizing, however, that such particles are not very realistic in practice, the theory is 'calibrated' to consider particle shapes others than ellipsoidal.

We re-call from the introduction: The scope of this note is to explore the possibility of establishing a method by which the rheological properties of SCC can be predicted by composite theory. The conclusion is that it is very likely that such prediction can be made.

Finally: The analysis made in this note on composite liquids with stiff particles can easily be generalised to apply also for composite fluids with soft particles (voids). Only a few obvious modifications have to be introduced into the analysis of extreme composites made by the author in (2). This feature might be useful when tailoring the viscosity of SCC, for example by modifying the matrix properties by air entrainment.

6. NOTATIONS

Abbreviations and subscripts

V	Volume
P	Phase P
S	Phase S
No subscript	Composite material

Geo-parameters

$c = V_P/(V_P+V_S)$	Volume concentration of phase P
A	Aspect ratio, length/diameter of ellipsoidal particle
μ^0	Shape factor
μ	Shape function
$c_{P,CS}$	Critical concentrations
γ	Geo-function
M	Interaction power in general
M_S	Interaction power in yield stress analysis
M_V	Interaction power in viscosity analysis

Stiffness and other properties (shear)

G	Stiffness
$n_g = G_P/G_S$	Stiffness ratio
η	Viscosity
C(t)	Creep function (with time t)
$\tau = \eta/G$	Relaxation time
S	Yield stress

Stress (shear)

s	External stress
s_P	Phase P stress caused by external stress
s_S	Phase S stress caused by external stress

REFERENCES

1. Bager, D.H., Geiker, M.R., and Jensen, R.M.: "Rheology of Self Compacting Mortars – Influence of particle grading", Nordic Concrete Research, 1(2001).
2. Nielsen, L. Fuglsang: "Rheology of extreme composites", In "Papers in Structural Engineering and Materials - A Centenary Celebration", 179-187, Dept. of Struct. and Materials, Tech. Univ. Denmark, 2000.
3. Brandl, M. and Thrane, L. Nyholm: "Rheological properties of Self Compacting Concrete (SCC)", M.Sc. thesis, Department of Civil Engineering, Tech. Univ. Denmark, 2001.
4. Geiker, M.R., Brandl, M., Thrane, L. Nyholm, Bager, D.H., and Wallevik, O.: On the effect of measuring procedure on the apparent rheological properties of self-compacting concrete. Submitted for publication to Cement and Concrete Research, August 2001.
5. deLarrard, F.: "Concrete Mixtures Proportioning: A Scientific Approach", Modern Concrete Technology Series, E&FN SPON, London 1999.

6. Reiner, M.: "Lectures on theoretical rheology" (third edition), North-Holland Publishing Company, Amsterdam, 1960.
7. Nielsen, L. Fuglsang: "Elastic Properties of Two-Phase Materials", *Materials Science and Engineering*, 52(1982), 39-62.
8. *Idem*: "Stiffness and other physical properties of composites as related to phase geometry and connectivity - Part I: Methods of analysis" (pages 725-734) and "... Part II: Quantification of geometry" (pages 735-743) in proceedings Vol. 2 (Ed. B. Saxhof) of the 3rd Symposium on Building physics in the Nordic countries, Copenhagen, Sept. 13-15, 1993, Thermal Insulation Laboratory, Technical University of Denmark 1993.
9. *Idem*: "Composite Materials - Mechanical and physical behaviour as influenced by phase geometry", Monograph, Department of Civil Engineering, Tech. Univ. Denmark, in press 2001.
10. Bingham, E.C.: "An investigation of the laws of plastic flow", *Bur. of Standards Bull.*, 13(1916), 309. 'Colloid types', *Fifth Coll. Symp. Monograph*, 1(1928), 219.
11. Einstein, A.: "Eine neue Bestimmung der Moleküldimensionen", *An. Physik*, 19(1906), 289 and 34(1911), 104.
12. Holliday, L. (ed): "Composite materials", Elsevier Publishing Company, New York, 1966, (p. 34, Chapter on Inclusions in a Viscous Matrix).
13. Eirich, R.F. (ed): "Rheology, Theory and Applications", Academic Press Inc., New York, 1958, (p. 363, Chapter on Rheological Properties of Asphalt).
14. Flügge, W.: "Viscoelasticity", Blaisdell Publ. Comp., London 1967.
15. Nielsen, L. Fuglsang: "Rheologische Eigenschaften für isotrope linear-viscoelastische Kompositmaterialien", *Cement and Concrete Research*, 3(1973), 751 - 766.
16. *Idem*: Strength and Stiffness of Porous Materials, *Journ. Am. Ceramic Soc.*, 73(1990), 2684-89.
17. *Idem*: On strength of porous material – simple systems and densified systems, *Materials and Structures*, 31(1998), 651-661.
18. Geiker, M.R., Brandl, M., Thrane, L. Nyholm, and Nielsen, L. Fuglsang: "Effect of coarse aggregate fraction and shape on the rheological properties of self-compacting concrete". Submitted for publication in *ASTM, Cement Concrete and Aggregates*, September 2001.

APPENDIX: Composite behaviour versus geometry

A composite theory presented in (7,8) is summarised operationally by the following Equations A1, A2¹⁾, and A3¹⁾ which apply in general (globally) for any isotropic composite material composed by phase P and phase S. As written they apply for the shear behaviour (Shear modulus) of composites.

Composite stiffness G is predicted by Equation A1 with the geometry function, γ , introduced from Equation A2. A variety of composite geometries are considered by this function where specific composite geometries are quantified by shape functions (μ_P , μ_S) expressed by Equation A3 and illustrated in Figure A1.

$$G = G_S \frac{n_g + \gamma[1 + c(n_g - 1)]}{n_g + \gamma - c(n_g - 1)} \quad \text{with} \quad n_g = \frac{G_P}{G_S} \quad (\text{A1})$$

$$\frac{s_P}{s} = \frac{n_g(1 + \gamma)}{n_g + \gamma[1 + c(n_g - 1)]} \quad ; \quad \frac{s_S}{s} = \frac{n_g + \gamma}{n_g + \gamma[1 + c(n_g - 1)]}$$

$$\gamma = \frac{\gamma_S}{2} \left[\mu_P + n_g \mu_S + \sqrt{(\mu_P + n_g \mu_S)^2 + 4n_g(1 - \mu_P - \mu_S)} \right] \quad (\text{for } \nu_P = \nu_S) \quad (\text{A2})$$

and $\gamma_S = \frac{7 - 5\nu_S}{2(4 - 5\nu_S)}$ (with Poisson's ratios ν_P and ν_S)

$$\mu_S = \mu_S^o \left(1 - \frac{c}{c_S} \right)^M \quad ; \quad \mu_P = \mu_P^o \left(1 - \frac{c}{c_P} \right)^M \quad \text{with} \quad c_P = -\frac{\mu_P^o}{\mu_S^o} c_S \quad (c \leq c_S) \quad (\text{A3})$$

where M is a so-called interaction power, see comments below. The shape of the particles considered are quantified by the shape factors $0 \leq \mu_P^o \leq 1$ and $0 \geq \mu_S^o \geq -1$ (2,9). In the case of ellipsoidal particles the factors can be determined by Equation A4 introducing the aspect ratio, A = length/diameter of particles. As usual volume concentration of particles is denoted by c. The critical concentration of particles (maximum packing density or eigenpacking) is denoted by c_S . Particles start interfering (blocking) at this concentration. The critical concentration tells about the quality (smoothness and density) of particles size distribution. The quality of distribution increases with increasing c_S .

$$\mu_P^o = \begin{cases} \frac{3A}{A^2 + A + 1} & A \leq 1 \\ 3 \frac{A^2 - A + 1}{4A^2 - 5A + 4} & A > 1 \end{cases} \quad ; \quad \mu_S^o = - \begin{cases} \mu_P^o & A \leq 1 \\ 4\mu_P^o - 3 & A > 1 \end{cases} \quad (\text{A4})$$

¹⁾ As the result of recent research (9,16,17), Equations A2 and A3 are modified slightly relative to the original versions in (7). The modifications and the introduction of the interaction factor, M, are of no principle significance in the present theoretical presentation.

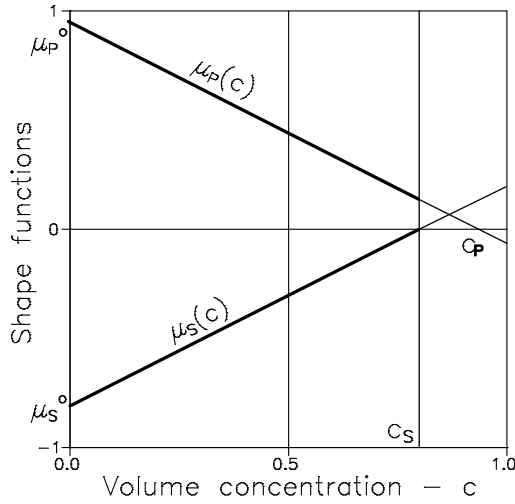


Figure A1. Shape functions (μ_p, μ_s) with $M = 1$ and critical concentration c_s (concentration of solid phase in a pile of particles).

Comments: Normally (2,16,9) an interaction power of $M = 1$ is used in composite analysis assuming a 'moderately' increasing state of interaction between aggregates at increasing concentration. It comes from (16,9) that lower interaction and higher interaction can be described with $M < 1$ and $M > 1$ respectively. Research on shape functions in details has only been made on very special composites (17). Unless otherwise stated, a moderate interaction with $M = 1$ is used in this paper. If otherwise stated M_s and M_v indicate interaction powers used in yield stress analysis and in viscosity analysis respectively.

Extreme composites

The above complex of expressions reduce considerably when composites are considered where phase P is very stiff, meaning that $n_g \rightarrow \infty$. When incompressible components are considered additionally (fluid phase S with $v_s = 0.5$) we get

$$\frac{G}{G_s} = \frac{1 + \gamma_\infty c}{1 - c} \quad \text{with} \quad \gamma_\infty = \begin{cases} \frac{3}{2} \frac{\mu_p + \mu_s - 1}{\mu_s} & \text{for } c < c_s \\ \infty & \text{for } c \geq c_s \end{cases} \quad (\text{A5})$$

$$\frac{s_p}{s} = \frac{1 + \gamma_\infty}{1 + c \gamma_\infty}; \quad \frac{s_s}{s} = \frac{1}{1 + c \gamma_\infty}$$

Viscoelasticity

It comes from the "Correspondence Principle" (elastic-viscoelastic analogy), presented in (14), that Equation A5 can be used also to predict the shear creep functions $C(t)$ of viscoelastic extreme composites. (A creep function is strain caused by stress $s \equiv 1$). The simple result is shown in Equation A6 with relative shear modulus G/G_s introduced from Equation A5.

$$\frac{C_s(t)}{C(t)} = \frac{G}{G_s} \quad (\text{A6})$$

For the Maxwell composite considered in this paper we then have the following relations between the matrix creep function (C_s) and the composite creep function (C), and between the matrix viscosity and the composite viscosity.

$$C_s = \frac{1}{2G_s} + \frac{t}{2\eta_s} = \frac{1}{2G_s} \left(1 + \frac{t}{\tau_s} \right) \quad \text{with } \tau_s = \frac{\eta_s}{G_s} \Rightarrow \quad (A7)$$

$$C = \frac{G_s}{G} \left[\frac{1}{2G_s} + \frac{1}{2\eta_s} \right] = \frac{1}{2G} \left(1 + \frac{t}{\tau} \right) \quad \text{with } \tau = \frac{\eta}{G} = \tau_s$$

$$\frac{\eta}{\eta_s} = \frac{G}{G_s} = \frac{1 + \gamma_\infty c}{1 - c} \quad (A8)$$

These expressions tell that the type of matrix viscoelasticity is maintained also to apply for the composite considered. This statement agrees positively with a creep analysis of concrete made by the author in (15). The phase stresses keep their values from Equation A5.

Monitoring - Summary of a Concrete Café at the 18th Nordic Concrete Research Meeting, Elsinore, Denmark



Chairman Carsten Henriksen
cfh@vd.dk

The Danish Road Directorate
Skanderborg, Denmark

ABSTRACT

The paper is a summary of the Concrete Café held at the NCRM. Four papers were presented to kick-start a discussion on monitoring of concrete structures.

The paper gives a brief summary of the content of the café and highlights topics discussed during the session.

Key words: Moisture, Corrosion, Deterioration, Responsibility.

1. INTRODUCTION

The definition of monitoring of structures includes a widespread number of activities - from special investigation of a structure to the surveying of the condition of a structure over time.

The four papers presented very well illustrated the variety of the subject including 2 papers devoted to survey (Per Goltermann and Viggo Jensen), 1 paper to special investigation of structures (Joachim Jeppsson and Nils Ryden) and 1 paper devoted to service life evaluation and monitoring (Odd Gjølrv).

In the following section 2 the content of the café is summarised and selected topics are highlighted in an overall way as the papers in detail can be found in the proceedings.

App. 25 participants attended the café.

2. MONITORING

Monitoring of a structure is carried out to fulfil one or more of the following reasons:

1. Assessment of the condition and the remaining service life of an existing structure
2. To prove design criteria
3. Quality control (repair works, fresh concrete control etc.)
4. Research and development
5. Management

Monitoring of a structure involves a sampling of data.

Monitoring can be carried out either as a single test program carried out manually to the structure or data can be automatically sampled over time using build-in sensors.

Whether monitoring is carried out for the one or the other reason it involves issues to be discussed and evaluated before the carrying out of the monitoring:

1. **Choice of test areas** - monitoring has to be limited to selected representative areas. How to define a representative area?
2. **Responsibility** - when a monitoring program has been established the owner/the society expects that no unforeseen events will take place. How to ensure that the monitoring program reveals representative and reliable data?
3. **Cost/benefit**. The benefit to the owner/the society has to be proven. If the monitoring requires too extensive special inspections prior to the installation and later to calibrate the sensors and prove the results the benefit is in question.

Throughout the last decade a number of test methods and sensors have been developed to help monitoring parameters critical to in particular the durability - moisture, chloride penetration, carbonation, corrosion activity etc.

A vast experience additionally has been accumulated through a number of monitoring projects as illustrated by the presented papers and the following discussion.

The discussion however revealed that the experience and knowledge sampled and accumulated to some extent have difficulties to be used in an optimum way. Valuable and well-documented experience has not been implemented to an optimum extent.

The participants expressed a certain frustration due to this fact. The owner has to play a more active role in the future to ensure the implementation of new knowledge and experience in codes and standards and in the management of existing structures.

REFERENCES

- | | |
|-------------------------------|--|
| Gjørsv, Odd E.; Gussiås, Arne | Service Life Management of Concrete Harbour Structures. Proceedings Nordic Concrete Research meeting, Elsinore, Denmark, June 2002 |
| Goltermann, Per | SMART STRUCTURES: Monitoring of concrete Structures. Proceedings Nordic Concrete Research meeting, Elsinore, Denmark, June 2002 |
| Jensen, Viggo | Relative Humidity measured by wooden stick method in Norwegian Concrete Structures with and without Surface Protection. Proceedings Nordic Concrete Research meeting, Elsinore, Denmark, June 2002 |
| Jeppsson, Joakim; Ryden, Nils | Destructive and Non-Destructive Assessment of Concrete. Proceedings Nordic Concrete Research meeting, Elsinore, Denmark, June 2002 |

Rheology of some fluid extreme composites

Such as fresh self-compacting concrete



Lauge Fuglsang Nielsen
 Associate professor, Ph.D.
 Department of Civil Engineering, Building 118
 Technical University of Denmark
 DK-2800 Lyngby, Denmark
 E-mail: lfn@byg.dtu.dk

ABSTRACT

A method is developed by which the well-known Bingham description of flow in homogeneous liquids with yield stress is generalised to apply also for composite fluids. In the present context such fluids are defined as fluids mixed with very stiff particles of known shapes and size distributions.

In practice the composite aspects of the generalised Bingham description is a major advantage. Only three geometrical parameters for the particles and two material properties for the fluid matrix are required in order to describe the generalised Bingham behaviour of any composition of the composite fluid considered. The Bingham method normally used needs experimental calibration for any new composition.

Finally, it is indicated how the analysis presented can easily be generalised to apply also for composite fluids with soft particles (voids). This feature might be useful when tailoring the viscosity of SCC, for example by modifying the matrix properties by air entrainment.

Key words: Composite fluid, Bingham, Composite Bingham, Self-compacting concrete (SCC)

1. INTRODUCTION

This paper is part of an on-going project (1,2,3,4,18) on Self-Compacting Concrete (SCC) at the Department of Civil Engineering, Technical University of Denmark. The particular scope of the paper is to look at possibilities of establishing a composite method of predicting the rheology of SCC, which may serve as an alternative to the semi-empirical method, suggested by deLarrard (5). To the author's knowledge such approach has not yet been presented.

Composite fluids are considered mixtures of very stiff elastic particles (phase P) in a Maxwell fluid matrix (phase S). The basic shear stress-strain relations of the components are presented in Equation 1 where the rigidity and viscosity of the fluid are G_S and η_S respectively. The rigidity of the particle phase is denoted by G_P . Shear stress and strain are denoted by s and e respectively. The stress-strain relation for the fluid presented in Equation 1 is consistent with a similar expression

presented by Reiner (6).

$$\frac{de}{dt} = \frac{ds/dt}{2G_S} + \frac{s}{2\eta_S} \quad \text{Phase S : Maxwell fluid} \quad (1)$$

$$e = \frac{s}{2G_P} \quad \text{Phase P : Hooke solid}$$

Equation 2 defines the volume concentration of particles in composites considered with volumes denoted by V. In general subscripts P and S refer to particle phase and matrix phase S respectively. A complete list of symbols is presented at the end of this paper.

$$c = \frac{V_P}{V_P + V_S} \quad \text{Volume concentration of particles} \quad (2)$$

2. COMPOSITE FLUID

It can be shown by a composite theory developed in (7,8) that a Maxwell fluid with very stiff particles added will act as a Maxwell fluid itself. The constitutive equation becomes Equation 3 with particles influencing the composite properties (G and η) as described in Equation 4. The average phase P stress (s_P) and average phase S stress (s_S) are presented in Equation 5. (The theoretical steps to obtain these results are summarised in the Appendix at the end of this paper).

$$\frac{de}{dt} = \frac{ds/dt}{2G} + \frac{s}{2\eta} \quad \text{Composite Maxwell fluid with } G_P \gg G_S \quad (3)$$

$$\frac{\eta}{\eta_S} = \frac{G}{G_S} = \frac{1 + \gamma_\infty c}{1 - c} \quad \text{with } \gamma_\infty = \begin{cases} \frac{3}{2} \frac{\mu_P + \mu_S - 1}{\mu_S} & c < c_S \\ \infty & c > c_S \end{cases} \quad (4)$$

$$\frac{s_P}{s} = \frac{1 + \gamma_\infty}{1 + c \gamma_\infty}, \quad \frac{s_S}{s} = \frac{1}{1 + c \gamma_\infty} \quad (5)$$

The composite geometry (particle shape and size distribution) is considered by the so-called geometry function (γ_∞) and shape functions (μ_P, μ_S), explained and determined in the Appendix. Principal parameters for the description of geometry in this paper are aspect ratio (A = length/diameter) and the critical concentration c_S of ellipsoidal particles considered ($c_S \approx$ maximum packing density \approx eigenpacking). Normally, we may expect improved quality of particle size distribution (smoothness and density) to be associated with higher c_S . An extra parameter, the so-called interaction power, M, is used in the Appendix to consider the interaction between particles. If not otherwise stated M = 1 (moderate interaction) is assumed.

2.1 Composite Newton fluid

The stress-strain relation for a so-called composite Newton fluid is obtained from the Maxwell solution letting the rigidity G_S approach infinity. The result is presented in Equation 6 with viscosity and stresses kept as expressed by Equations 4 and 5 respectively.

$$\frac{de}{dt} = \frac{s}{2\eta} \quad \text{composite Newton fluid } (G_S \rightarrow \infty \Rightarrow G \rightarrow \infty) \quad (6)$$

2.2 Composite Bingham fluid

Homogeneous Newton fluids were considered by Bingham (10) who suggested that viscous behaviour first appears when stress has become greater than a certain so-called yield stress S . We adopt the idea of Bingham's in the following way: Viscous behaviour of the composite Newton liquid first appears when the matrix stress (s_s in Equation 5) exceeds the matrix yield stress S_s . Then Equation 6 becomes modified as shown in Equation 7 with viscosities kept as expressed by Equation 4. Formally the original- and the generalised Bingham expression look alike.

$$\frac{de}{dt} = \frac{s - S}{2\eta} \Rightarrow s = S + 2\eta \frac{de}{dt} \quad \text{composite Bingham fluid with} \quad (7)$$

$$\text{Yield stress : } S = S_s(1 + \gamma_\infty c) \quad \text{and} \quad \text{Viscosity : } \eta = \eta_s \frac{1 + \gamma_\infty c}{1 - c}$$

Curiosum: The relative viscosity predicted by Equation 4 agrees with Equation 8 developed by Einstein (11) in his study of the viscosity of dilute sugar solutions. The expression also agrees with data obtained from experiments on mixtures made of fluids with finite particle concentrations. Two empirical descriptions (Eilers and Brinkman) for such data are presented in Equation 9 reproduced from (12,13). In Figure 1 the latter results are compared graphically with the results obtained by the present theory. In Figure 2 is shown, additionally, how relative yield stress predicted by Equation 7 varies with particle concentrations.

$$\frac{\eta}{\eta_s} = 1 + 2.5c \quad \text{dilute solution with spherical particles} \quad (8)$$

$$\frac{\eta}{\eta_s} = \begin{cases} \left(1 + \frac{1.25c}{1 - 1.28c}\right)^2 & \text{Eilers} \\ (1 - c)^{-5/2} & \text{Brinkman} \end{cases} \quad \text{spherical particles} \quad (9)$$

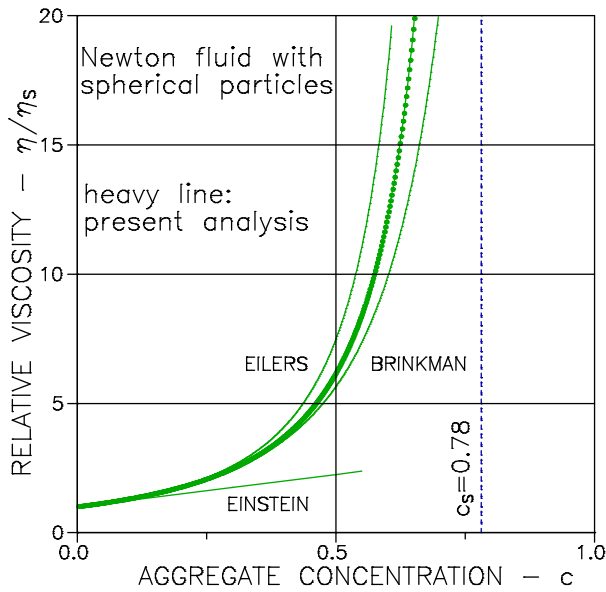


Figure 1. Spherical particles ($A = 1$) in a viscous matrix. Present analysis and empirical descriptions by Eilers and Brinkman.

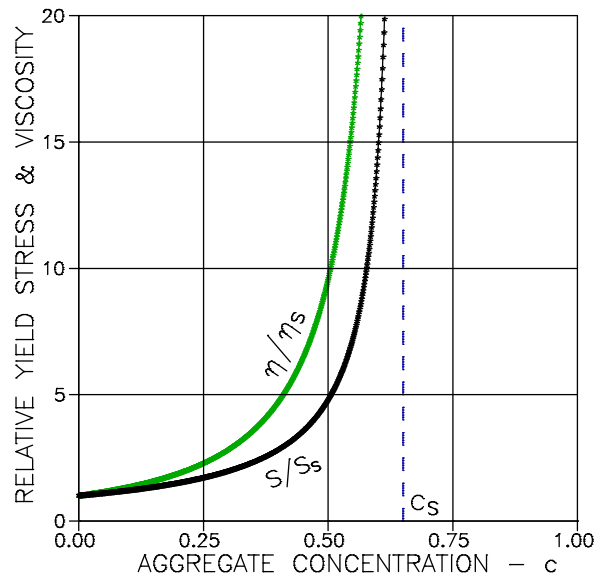


Figure 2. Relative quantities of composite viscosity and yield stress. Aggregates: $(A, c_s) = (2, 0.65)$.

3. ILLUSTRATIVE EXAMPLES

The theoretical influence of ellipsoidal particle shapes and quality of size distributions on the rheology of SCC are illustrated in the following Figures 3 - 6. All composites are assumed to have a mortar (phase S) with a viscosity of $\eta_S = 2.5 \text{ Pa}\cdot\text{sec}$ and a yield stress of $S_S = 1.0 \text{ Pa}$. In the analysis of both viscosity and yield stress it is assumed that interaction is moderate ($M = 1$).

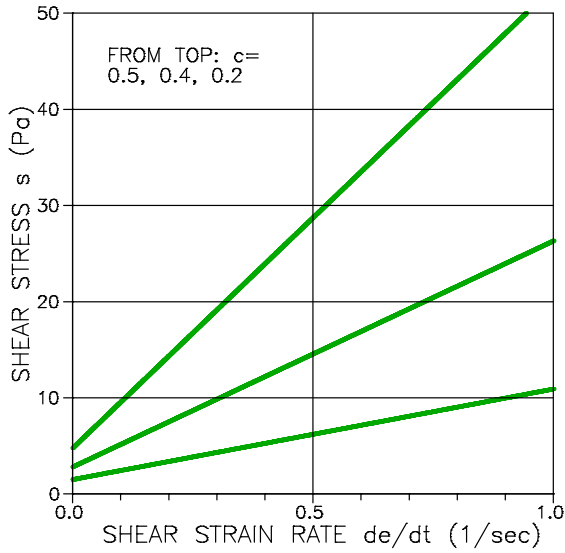


Figure 3. Composite Bingham material with various contents of aggregates with $A = 2$. Well graded with $c_S = 0.65$.

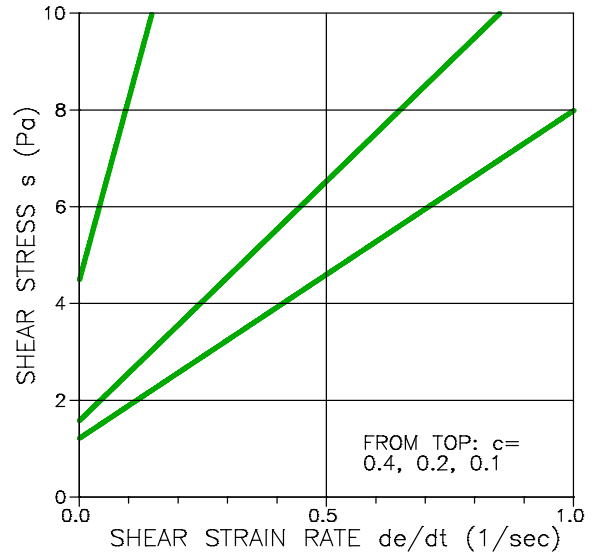


Figure 4. Composite Bingham material with various contents of aggregates with $A = 2$. Badly graded with $c_S = 0.5$.

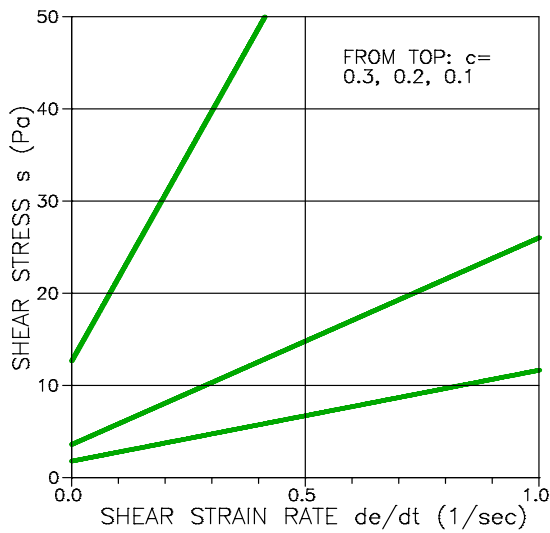


Figure 5. Composite Bingham material with various contents of aggregates with $A = 10$. Well graded with $c_S = 0.35$.

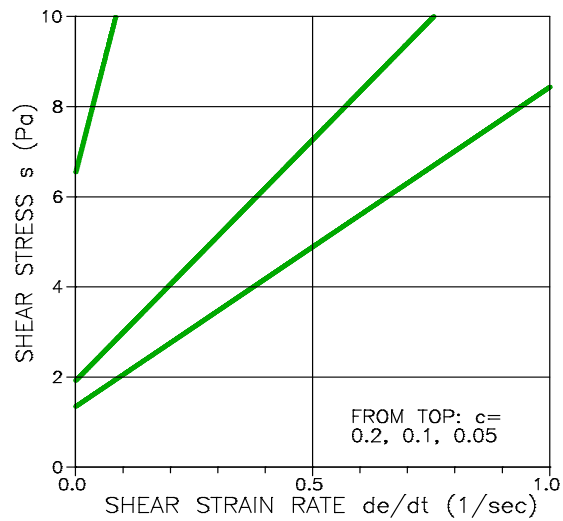


Figure 6. Composite Bingham material with various contents of aggregates with $A = 10$. Badly graded with $c_S = 0.25$.

Discussion

It is observed from Figures 3 - 6 that a particle aspect ratio increasingly different from $A = 1$ (spheres) and a bad particle size distribution (lower c_s) increase viscosity and yield stress of composites. These deductions agree with experimental observations made in (3). Also observed in (3) is that normalised viscosity varies as presented in Figure 2.

4. CALIBRATION

As previously mentioned the particles primarily assumed in this paper are smooth ellipsoidal particles. Recognizing that this assumption is not very realistic in practice, we must accept that geometrical information on particles must be determined by calibration with experimental data. In this section it is shown where theoretical modifications can be made without hurting the basic idea of a sound composite approach to the rheological quantification of particulate fluids. Obviously, the targets of calibration are the shape quantifications: 1) Shape factors and 2) Shape functions.

1) Other shape factors than for ellipsoidal particles can be calculated as demonstrated in (2, Fig. 2). Mixtures involving a variety of aspect ratios are considered in (9). In the present theoretical presentation, however, we suggest that shape deviations from ellipsoidal can be calibrated using Equation A4 with a simple multiplication of an aspect ratio A , estimated from particles averaged to be ellipsoidal.

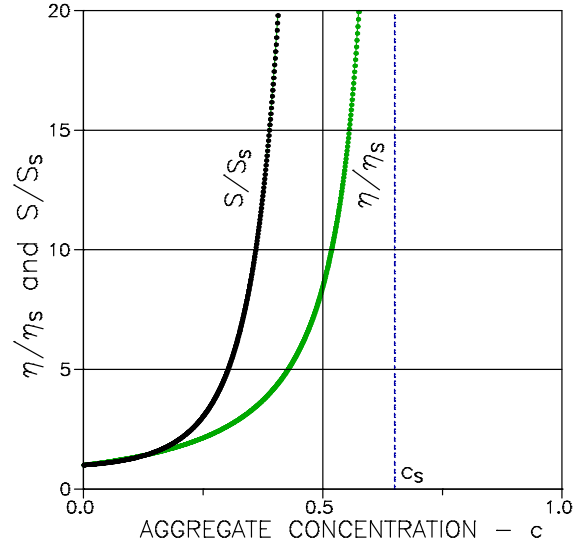


Figure 7. Normalised viscosity (with $M_v = 1$) and normalised yield stress (with $M_s = 3.5$). $(A, c_s) = (1, 0.65)$

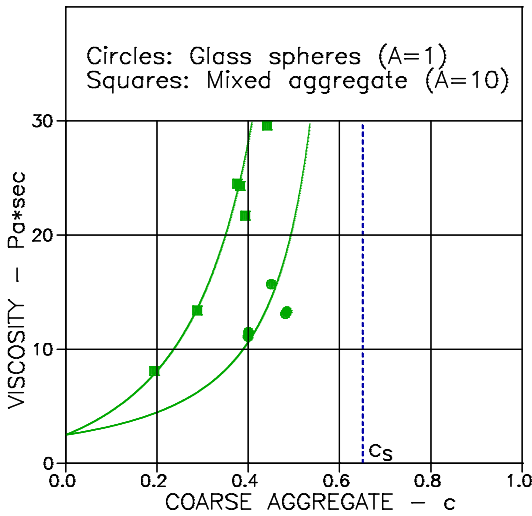


Figure 8. Viscosity of concrete as related to volume fraction of coarse aggregates (18). Solid lines are predicted with $M_v = 1$. Mortar viscosity is $\eta_s = 2.5 \text{ Pa}\cdot\text{sec}$. $c_s = 0.65$.

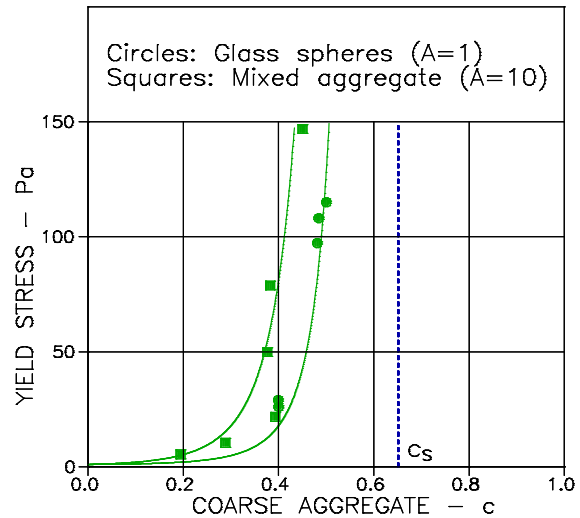


Figure 9. Yield stress of concrete as related to volume fraction of coarse aggregates (18). Solid lines are predicted with $M_s = 3.5$. Mortar yield stress is $S_s = 1 \text{ Pa}$. $c_s = 0.65$.

2) As previously indicated in Chapter 2 we have, until now considered interaction between particles to be moderate ($M = 1$). Higher or lower states of interaction can be considered with $M > 1$ and $M < 1$ respectively (see Appendix). We must expect that different M s may apply when viscosity and when yield stress respectively are considered. Interaction may be different between moving and not moving aggregates. We introduce M_S and M_V for interactions powers applying in yield stress analysis and in viscosity analysis respectively.

It is demonstrated, comparing Figures 2 and 7, how relative viscosity and relative yield stress reverse their orders of magnitudes by increasing the interaction power (M_S) in the yield stress analysis. Incidentally, Figure 7 compares positively with experimental data reported in (3).

Remark: As previously indicated, the present paper is part of an on-going SCC project at the Technical University of Denmark. A parallel experimental study has been made on the influence of coarse aggregates on the rheology of fresh concrete. A prime purpose of this study has been to investigate the applicability of the model developed in this paper. The study is reported in (18) from which Figures 8 and 9 are reproduced. The aspect ratios (A) and the interaction powers (M) used are calibrated in (18) according to the considerations made above.

5. FINAL REMARKS

The well-known Bingham description of the rheology of homogeneous fluids has been generalised in this paper also to include the rheological description of composite fluids. The advantage of such generalisation is obvious: With three parameters (shape factor μ_P^0 , packing density c_S , and interaction power M) to describe the composite geometry, only two material properties (viscosity η_S , and yield stress S_S) of the fluid matrix are required to describe the generalised Bingham behaviour at any composition of the composite fluid considered. The traditional Bingham model needs experimental calibration for any new composition considered. It is worthwhile noticing that shapes and size distribution of particles are considered by the three geometrical parameters mentioned.

The theory presented in this paper is based on global solutions for the mechanical/physical behavior of composite materials with any isotropic geometry. A numerical quantification of specific composite geometries is needed in this analysis, which is, at the present, most accurately developed for particulate composites with ellipsoidal particles. Recognizing, however, that such particles are not very realistic in practice, the theory is 'calibrated' to consider particle shapes others than ellipsoidal.

We re-call from the introduction: The scope of this note is to explore the possibility of establishing a method by which the rheological properties of SCC can be predicted by composite theory. The conclusion is that it is very likely that such prediction can be made.

Finally: The analysis made in this note on composite liquids with stiff particles can easily be generalised to apply also for composite fluids with soft particles (voids). Only a few obvious modifications have to be introduced into the analysis of extreme composites made by the author in (2). This feature might be useful when tailoring the viscosity of SCC, for example by modifying the matrix properties by air entrainment.

6. NOTATIONS

Abbreviations and subscripts

V	Volume
P	Phase P
S	Phase S
No subscript	Composite material

Geo-parameters

$c = V_P/(V_P+V_S)$	Volume concentration of phase P
A	Aspect ratio, length/diameter of ellipsoidal particle
μ^0	Shape factor
μ	Shape function
c_{P,C_S}	Critical concentrations
γ	Geo-function
M	Interaction power in general
M_S	Interaction power in yield stress analysis
M_V	Interaction power in viscosity analysis

Stiffness and other properties (shear)

G	Stiffness
$n_g = G_P/G_S$	Stiffness ratio
η	Viscosity
C(t)	Creep function (with time t)
$\tau = \eta/G$	Relaxation time
S	Yield stress

Stress (shear)

s	External stress
s_P	Phase P stress caused by external stress
s_S	Phase S stress caused by external stress

REFERENCES

1. Bager, D.H., Geiker, M.R., and Jensen, R.M.: "Rheology of Self Compacting Mortars – Influence of particle grading", Nordic Concrete Research, 1(2001).
2. Nielsen, L. Fuglsang: "Rheology of extreme composites", In "Papers in Structural Engineering and Materials - A Centenary Celebration", 179-187, Dept. of Struct. and Materials, Tech. Univ. Denmark, 2000.
3. Brandl, M. and Thrane, L. Nyholm: "Rheological properties of Self Compacting Concrete (SCC)", M.Sc. thesis, Department of Civil Engineering, Tech. Univ. Denmark, 2001.
4. Geiker, M.R., Brandl, M., Thrane, L. Nyholm, Bager, D.H., and Wallevik, O.: On the effect of measuring procedure on the apparent rheological properties of self-compacting concrete. Submitted for publication to Cement and Concrete Research, August 2001.
5. deLarrard, F.: "Concrete Mixtures Proportioning: A Scientific Approach", Modern Concrete Technology Series, E&FN SPON, London 1999.

6. Reiner, M.: "Lectures on theoretical rheology" (third edition), North-Holland Publishing Company, Amsterdam, 1960.
7. Nielsen, L. Fuglsang: "Elastic Properties of Two-Phase Materials", *Materials Science and Engineering*, 52(1982), 39-62.
8. *Idem*: "Stiffness and other physical properties of composites as related to phase geometry and connectivity - Part I: Methods of analysis" (pages 725-734) and "... Part II: Quantification of geometry" (pages 735-743) in proceedings Vol. 2 (Ed. B. Saxhof) of the 3rd Symposium on Building physics in the Nordic countries, Copenhagen, Sept. 13-15, 1993, Thermal Insulation Laboratory, Technical University of Denmark 1993.
9. *Idem*: "Composite Materials - Mechanical and physical behaviour as influenced by phase geometry", Monograph, Department of Civil Engineering, Tech. Univ. Denmark, in press 2001.
10. Bingham, E.C.: "An investigation of the laws of plastic flow", *Bur. of Standards Bull.*, 13(1916), 309. 'Colloid types', *Fifth Coll. Symp. Monograph*, 1(1928), 219.
11. Einstein, A.: "Eine neue Bestimmung der Moleküldimensionen", *An. Physik*, 19(1906), 289 and 34(1911), 104.
12. Holliday, L. (ed): "Composite materials", Elsevier Publishing Company, New York, 1966, (p. 34, Chapter on Inclusions in a Viscous Matrix).
13. Eirich, R.F. (ed): "Rheology, Theory and Applications", Academic Press Inc., New York, 1958, (p. 363, Chapter on Rheological Properties of Asphalt).
14. Flügge, W.: "Viscoelasticity", Blaisdell Publ. Comp., London 1967.
15. Nielsen, L. Fuglsang: "Rheologische Eigenschaften für isotrope linear-viscoelastische Kompositmaterialien", *Cement and Concrete Research*, 3(1973), 751 - 766.
16. *Idem*: Strength and Stiffness of Porous Materials, *Journ. Am. Ceramic Soc.*, 73(1990), 2684-89.
17. *Idem*: On strength of porous material – simple systems and densified systems, *Materials and Structures*, 31(1998), 651-661.
18. Geiker, M.R., Brandl, M., Thrane, L. Nyholm, and Nielsen, L. Fuglsang: "Effect of coarse aggregate fraction and shape on the rheological properties of self-compacting concrete". Submitted for publication in *ASTM, Cement Concrete and Aggregates*, September 2001.

APPENDIX: Composite behaviour versus geometry

A composite theory presented in (7,8) is summarised operationally by the following Equations A1, A2¹⁾, and A3¹⁾ which apply in general (globally) for any isotropic composite material composed by phase P and phase S. As written they apply for the shear behaviour (Shear modulus) of composites.

Composite stiffness G is predicted by Equation A1 with the geometry function, γ , introduced from Equation A2. A variety of composite geometries are considered by this function where specific composite geometries are quantified by shape functions (μ_P , μ_S) expressed by Equation A3 and illustrated in Figure A1.

$$G = G_S \frac{n_g + \gamma[1 + c(n_g - 1)]}{n_g + \gamma - c(n_g - 1)} \quad \text{with} \quad n_g = \frac{G_P}{G_S} \quad (\text{A1})$$

$$\frac{s_P}{s} = \frac{n_g(1 + \gamma)}{n_g + \gamma[1 + c(n_g - 1)]} \quad ; \quad \frac{s_S}{s} = \frac{n_g + \gamma}{n_g + \gamma[1 + c(n_g - 1)]}$$

$$\gamma = \frac{\gamma_S}{2} \left[\mu_P + n_g \mu_S + \sqrt{(\mu_P + n_g \mu_S)^2 + 4n_g(1 - \mu_P - \mu_S)} \right] \quad (\text{for } \nu_P = \nu_S) \quad (\text{A2})$$

and $\gamma_S = \frac{7 - 5\nu_S}{2(4 - 5\nu_S)}$ (with Poisson's ratios ν_P and ν_S)

$$\mu_S = \mu_S^o \left(1 - \frac{c}{c_S} \right)^M \quad ; \quad \mu_P = \mu_P^o \left(1 - \frac{c}{c_P} \right)^M \quad \text{with} \quad c_P = -\frac{\mu_P^o}{\mu_S^o} c_S \quad (c \leq c_S) \quad (\text{A3})$$

where M is a so-called interaction power, see comments below. The shape of the particles considered are quantified by the shape factors $0 \leq \mu_P^o \leq 1$ and $0 \geq \mu_S^o \geq -1$ (2,9). In the case of ellipsoidal particles the factors can be determined by Equation A4 introducing the aspect ratio, A = length/diameter of particles. As usual volume concentration of particles is denoted by c. The critical concentration of particles (maximum packing density or eigenpacking) is denoted by c_S . Particles start interfering (blocking) at this concentration. The critical concentration tells about the quality (smoothness and density) of particles size distribution. The quality of distribution increases with increasing c_S .

$$\mu_P^o = \begin{cases} \frac{3A}{A^2 + A + 1} & A \leq 1 \\ 3 \frac{A^2 - A + 1}{4A^2 - 5A + 4} & A > 1 \end{cases} \quad ; \quad \mu_S^o = - \begin{cases} \mu_P^o & A \leq 1 \\ 4\mu_P^o - 3 & A > 1 \end{cases} \quad (\text{A4})$$

¹⁾ As the result of recent research (9,16,17), Equations A2 and A3 are modified slightly relative to the original versions in (7). The modifications and the introduction of the interaction factor, M, are of no principle significance in the present theoretical presentation.

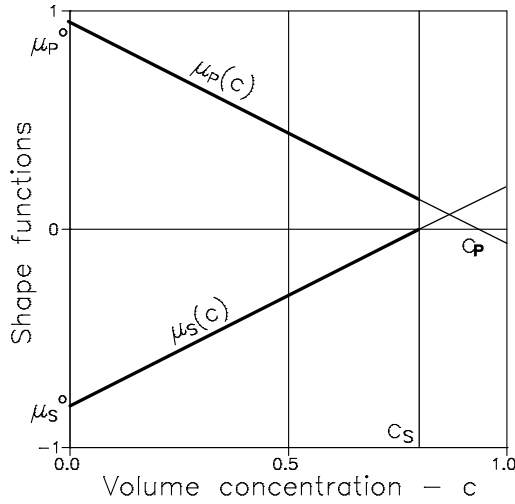


Figure A1. Shape functions (μ_p, μ_s) with $M = 1$ and critical concentration c_s (concentration of solid phase in a pile of particles).

Comments: Normally (2,16,9) an interaction power of $M = 1$ is used in composite analysis assuming a 'moderately' increasing state of interaction between aggregates at increasing concentration. It comes from (16,9) that lower interaction and higher interaction can be described with $M < 1$ and $M > 1$ respectively. Research on shape functions in details has only been made on very special composites (17). Unless otherwise stated, a moderate interaction with $M = 1$ is used in this paper. If otherwise stated M_s and M_v indicate interaction powers used in yield stress analysis and in viscosity analysis respectively.

Extreme composites

The above complex of expressions reduce considerably when composites are considered where phase P is very stiff, meaning that $n_g \rightarrow \infty$. When incompressible components are considered additionally (fluid phase S with $v_s = 0.5$) we get

$$\frac{G}{G_s} = \frac{1 + \gamma_\infty c}{1 - c} \quad \text{with} \quad \gamma_\infty = \begin{cases} \frac{3}{2} \frac{\mu_p + \mu_s - 1}{\mu_s} & \text{for } c < c_s \\ \infty & \text{for } c \geq c_s \end{cases} \quad (\text{A5})$$

$$\frac{s_p}{s} = \frac{1 + \gamma_\infty}{1 + c \gamma_\infty}; \quad \frac{s_s}{s} = \frac{1}{1 + c \gamma_\infty}$$

Viscoelasticity

It comes from the "Correspondence Principle" (elastic-viscoelastic analogy), presented in (14), that Equation A5 can be used also to predict the shear creep functions $C(t)$ of viscoelastic extreme composites. (A creep function is strain caused by stress $s \equiv 1$). The simple result is shown in Equation A6 with relative shear modulus G/G_s introduced from Equation A5.

$$\frac{C_s(t)}{C(t)} = \frac{G}{G_s} \quad (\text{A6})$$

For the Maxwell composite considered in this paper we then have the following relations between the matrix creep function (C_s) and the composite creep function (C), and between the matrix viscosity and the composite viscosity.

$$C_s = \frac{1}{2G_s} + \frac{t}{2\eta_s} = \frac{1}{2G_s} \left(1 + \frac{t}{\tau_s} \right) \quad \text{with } \tau_s = \frac{\eta_s}{G_s} \Rightarrow$$

$$C = \frac{G_s}{G} \left[\frac{1}{2G_s} + \frac{1}{2\eta_s} \right] = \frac{1}{2G} \left(1 + \frac{t}{\tau} \right) \quad \text{with } \tau = \frac{\eta}{G} = \tau_s \quad (\text{A7})$$

$$\frac{\eta}{\eta_s} = \frac{G}{G_s} = \frac{1 + \gamma_\infty c}{1 - c} \quad (\text{A8})$$

These expressions tell that the type of matrix viscoelasticity is maintained also to apply for the composite considered. This statement agrees positively with a creep analysis of concrete made by the author in (15). The phase stresses keep their values from Equation A5.

A combined temperature scanning calorimeter and dilatometer for studies of freeze/thaw effects in porous materials



Katja Fridh
MSc.
Building Materials, Lund Institute of Technology
Box 118, 221 00 Lund
E-mail: katja.fridh@byggtek.lth.se

Sture Lindmark¹
Dr.
Building Materials, Lund Institute of Technology
Box 118, 221 00 Lund



Lars Wadsö
Dr.
Building Materials, Lund Institute of Technology
Box 118, 221 00 Lund
E-mail: lars.wadso@byggtek.lth.se

ABSTRACT



In this paper we present a new combined temperature scanning calorimeter and dilatometer for the study of frost damage in relatively large samples (length 150 mm, diameter 40 mm) of cement-based materials. The two measuring techniques have been calibrated and tested both separately and combined. Measurements performed for testing the equipment show a satisfactory accuracy. The equipment is suitable for studies of frost deterioration mechanisms.

Key words: temperature scanning calorimeter, dilatometer, calibration, mortar, concrete.

1. INTRODUCTION

Frost damage of concrete and other porous materials is a major problem in outdoor structures, e.g. facades, bridges, dams and roads. Frost damage occurs both as surface scaling in which layers of the material are gradually scaled off from the material, and as internal deterioration in which ice formation creates hydraulic pressure and ice pressure on pore walls inside porous materials.

In the field of salt frost scaling substantial research was done in the 1980's and 1990's. Much of the research was performed within the RILEM TC 117 FDC 'Freeze Thaw and De-icing Salt Resistance'. Recently, damage hypotheses of surface scaling were presented by Lindmark [1]

¹ Presently at Icopal AB, Box 848, 201 80 Malmö, Sweden. E-mail: sture.lindmark@icopal.se.

and by Jepsen [2], both hypotheses were based on the theory of ice lens growth [3]. Jacobsen [4] performed extensive experimental research on ordinary Portland cement concretes and on concrete containing silica fume. Kaufmann [5] made extensive studies on the basis of which a qualitative discussion of destruction mechanisms was made. Rønning [6] carried out a large investigation about moisture uptake during freeze/thaw experiments and on the connection between laboratory testing and field exposure. A theoretical analysis of this water uptake process has been reported by Setzer [7].

The deterioration mechanisms responsible for surface and internal attack are fundamentally the same: water is transformed into ice, a process causing stresses in the material, as a consequence of which micro-cracking and reduced strength can occur [8]. The material's ability to accommodate the ice, to transport excess water and to hold unfrozen water decides how well it will perform during sub-zero temperatures. A major factor for frost damage is of course the water content in the material [9].

The mechanisms behind frost damage are complex, and the most important influencing factors can be divided into two groups, external and internal factors. The external factors are the freeze-thaw cycle (lowest temperature, duration, freezing rate) and the outer salt concentration. Among the internal factors the most important are pore size distribution, permeability and degree of saturation.

To explain the mechanism of internal frost attack several measuring equipments have been developed, many of them for the study of dilation (length changes) e.g. Valore [10]. Powers and Helmuth [3] formulated the theory of ice lens growth that not only explained observed phenomena but also provided the theory on which the salt frost scaling deterioration process by Lindmark [1] is based. Large investigations regarding length-change during freezing and thawing have also been carried out by Fagerlund [9] and Vourinen [11].

The study of ice-formation and melting using sensitive differential temperature scanning calorimeters was first carried out by Bager and Sellevold [12,13,14]. Their work was followed by studies of Fontenay [15], Matala [16], Kaufmann [5] and others.

As internal frost damage is caused by the phase transition of water to ice and possibly also ice to water, the combination of dilation and ice formation/melting (calorimetry) measurements is a very powerful way to investigate frost damage mechanisms. Verbeck and Klieger [17] presented the first equipment of this kind in 1958. Fagerlund [18] presented his combined measurement equipment in 1973. Penttala [19,20] placed strain gauges on samples tested in a temperature scanning calorimeter manufactured by Setaram.

In this paper the design of a new equipment for simultaneous measurements of ice formation/melting and expansion/contraction will be presented together with some test results. The calorimeter gives information on how much ice that forms (and at which temperature) in a concrete with a certain degree of saturation. The dilatometer gives information on to what extent this ice formation affects the material and how large damage it causes. This is very important information for the modelling of the relation between ice formation and loss of strength.

A problem with using the available temperature scanning calorimeters is the small specimen sizes (typically $d=14$ mm, $l=60$ mm). Our instrument can handle specimens with a diameter of 40 mm and a length of 150 mm. This makes it possible to study concrete samples. The preparation

of the specimens is also uncomplicated and rapid which is important with regards to minimizing the moisture loss.

The equipment will be used to study the effect of different freezing rates, lowest temperatures, durations and degrees of saturation on the internal frost resistance of micro-concrete. The objective with this work is to explain the mechanisms behind internal frost deterioration.

2. INSTRUMENT

The instrument is a combination of a temperature scanning calorimeter of the heat-conduction type and a LVDT (Linear Variable Differential Transducer) dilatometer. It simultaneously measures heat production/consumption during freezing and thawing and the associated length changes. Figures 1 and 2 show cross sections of the instrument.

The heat-flow is measured with eight thermo-couple plates (CP 1-127-08, Melcor, Trenton NJ, USA) surrounding the aluminium vessel holder (a total of 1016 semi-conductor thermo-couples). The sample (height 150 mm, diameter 40 mm) is placed in a cylindrical Invar vessel that is placed in the vessel holder (Fig. 2). Invar, a metal alloy containing 36% Ni and 64% Fe, has a low coefficient of thermal expansivity ($2 \cdot 10^{-6}$ 1/K). The sample is placed between a cylindrical stud (diameter 2 mm) on the bottom and the LVDT dilatometer (see section 3.1) at the top.

The instrument is a twin calorimeter with a reference sample placed in an identical calorimeter (Fig. 1). The reference should have approximately the same thermal properties as the sample, but not show any phase transitions in the temperature region of the measurement. The sample and the reference calorimeters are connected differentially so that disturbances that enter both calorimeters will be compensated for.

Each calorimeter has two aluminium heat sinks and the whole instrument is housed in a box made of 2 mm aluminium. Most empty volumes in the instrument are filled with insulation of extruded polystyrene.

The instrument is placed in a programmable low-temperature freezer with an internal fan (305/80-180 DU, Weiss Umwelttechnik GMBH, Lindenstruth, Germany). It is the temperature surrounding the calorimeter that controls its temperature. Normally the temperature is scanned quite slowly, e.g. 3 K/h.

The LVDT dilatometers are fastened in the lids of the Invar vessels (Fig. 2). Temperature is measured at five points inside the calorimeter with thermo-couples type K. The points are; sample, vessel holder, sample heat sink, reference vessel holder, and reference heat sink (the locations are shown in Fig. 2).

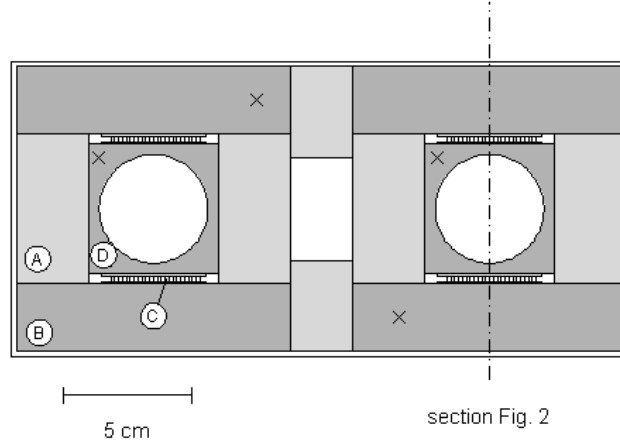


Figure 1 - Schematic drawing of instrument (horizontal cross section). (A) Insulation, (B) Heat sink, (C) Heat flow sensor, (D) Vessel holder. The sample is placed in the left vessel holder and a reference sample is placed in the right vessel holder. The x:s indicates the positions of the thermocouples for temperature measurement. The empty space in the center of the calorimeter houses the electrical wiring.

3. CALIBRATION

3.1 Measurements of length changes

The LVDT dilatometer (GTX2500, RDP Electrosense Inc., Pottstown PA, USA) has a linear stroke of ± 2.5 mm and a stated repeatability of $0.15 \mu\text{m}$. It is placed on top of the sample in the calorimeter (Fig. 2). The output from the dilatometer, a length L (mm), can for the present set-up be written as a function of the reference length L (mm) and thermal expansivity α (1/K) of a sample (subindex 1) and the sample holder (subindex 2):

$$\frac{dL}{dT} = L_1\alpha_1(T) - L_2\alpha_2(T) + K(T) \quad (\text{Eq. 1})$$

Here, K (mm/K) is the thermal expansion of the dilatometer itself. Note that α_1 , α_2 and K are functions of the temperature. The expansion properties of the sample holder and the dilatometer are not well known, and are therefore grouped together as one calibration parameter β (mm/K). Thus, Eq. 1 can be rewritten as:

$$\frac{dL}{dT} = L_1\alpha_1(T) + \beta(T) \quad (\text{Eq. 2})$$

To calibrate the equipment, a measurement with a sample with known L_1 and α_1 is made and $\beta(T)$ is calculated. This β is then used to calculate $\alpha_1(T)$ of a sample after a measurement:

$$\alpha_1(T) = \frac{dL/dT - \beta(T)}{L_1} \quad (\text{Eq. 3})$$

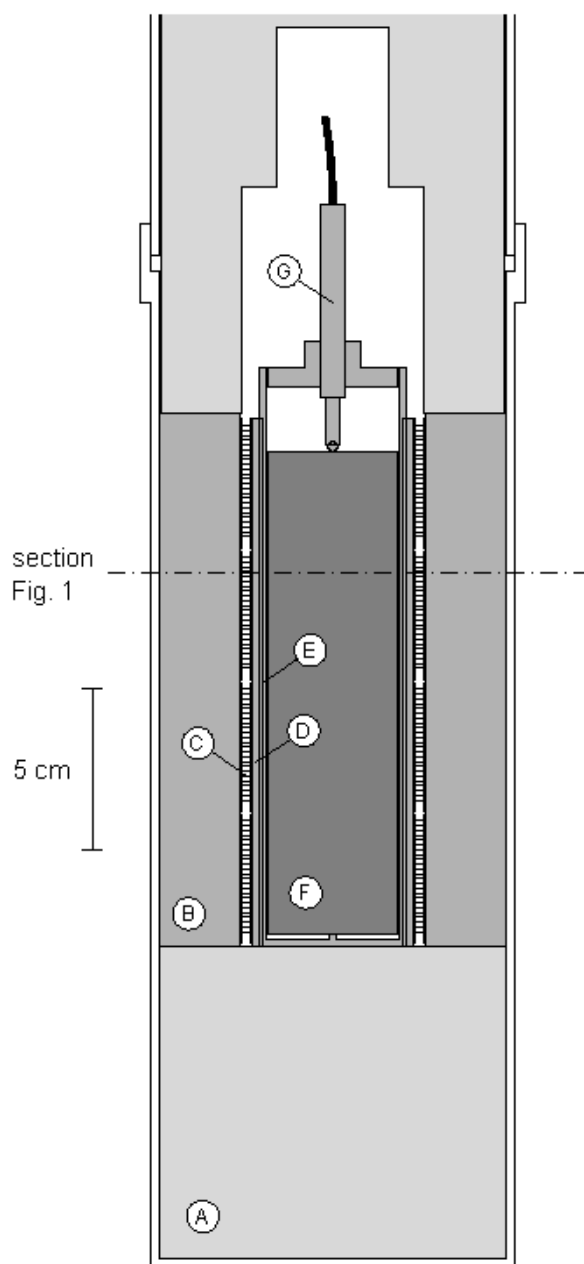


Figure 2 - Schematic drawing of instrument (vertical cross section). (A) Insulation, (B) Heat sink, (C) Heat flow sensor, (D) Vessel holder, (E) Vessel, (F) Sample, (G) LVDT Dilatometer. The top part of the calorimeter (with insulation) is not shown.

The dilatometer was calibrated with a 152 mm borosilicate glass square rod (Standard Reference Material 731L3, NIST, Gaithersburg MD, USA) using the thermal expansivity provided by NIST as a third order equation in the temperature range $-173 - +20^{\circ}\text{C}$. In the calibration, β was found to be rather constant in the temperature range $-60^{\circ}\text{C}-+20^{\circ}\text{C}$, with a value of $3.4 \cdot 10^{-4}$ mm/K.

3.2 Heat flow

The calibration of the calorimeter was made electrically while the calorimeter was kept at three temperatures, $+21^{\circ}\text{C}$, -18.3°C and -57.5°C . At each temperature a heat pulse was made and the resulting output signal was observed. For the calibration, we used a precision resistor of $100.0 \pm 0.1 \Omega$ centrally placed in a sample made from polyoxymethylene (POM) polymer that has similar thermal properties as cement mortar. The resistance of the heater did not change by more than 0.04Ω when the temperature changed from $+20^{\circ}\text{C}$ to -60°C .

The heat Q (J) released in each calibration pulse is:

$$Q = I^2 R \Delta t \quad (\text{Eq. 4})$$

Here, I (A) is the current through the heater, R (Ω) is the resistance of the heater, and Δt (s) is the duration of each pulse. The corresponding output from the calorimeter is the integral in units of (Vs) of the signal U (V) from the heat flow sensors. The calibration coefficient ε (W/V), used to convert the signal from the calorimeter to heat flow, is the ratio of Q and the integral of the signal from the heat flow sensors:

$$\varepsilon = \frac{Q}{\int U dt} \quad (\text{Eq. 5})$$

Figure 3 shows the result of the calibration of the calorimeter. Note that the calibration coefficient is temperature dependent.

4. TEST MEASUREMENTS

To test the length-change equipment a test measurement was performed on a bar of aluminium alloy with a diameter of 40 mm and a length of 145 mm (unknown type of alloy). The coefficient of thermal expansion directly obtained by the dilatometer is seen in Fig. 4 as a thin line. This signal was then adjusted with β and the thick line was obtained. This calculated coefficient of thermal expansion is somewhat higher than handbook values for pure aluminium. However, freeze/thaw dilations are substantially larger than those of aluminium and will be easy to detect (cf. Fig. 6).

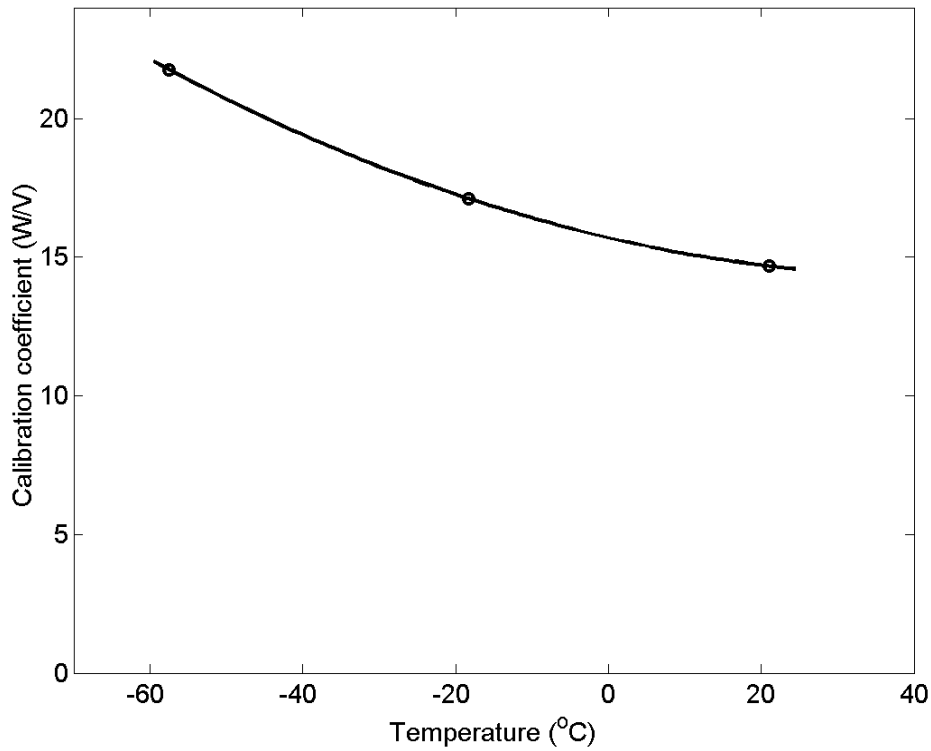


Figure 3 - Result of calibration of the calorimeter.

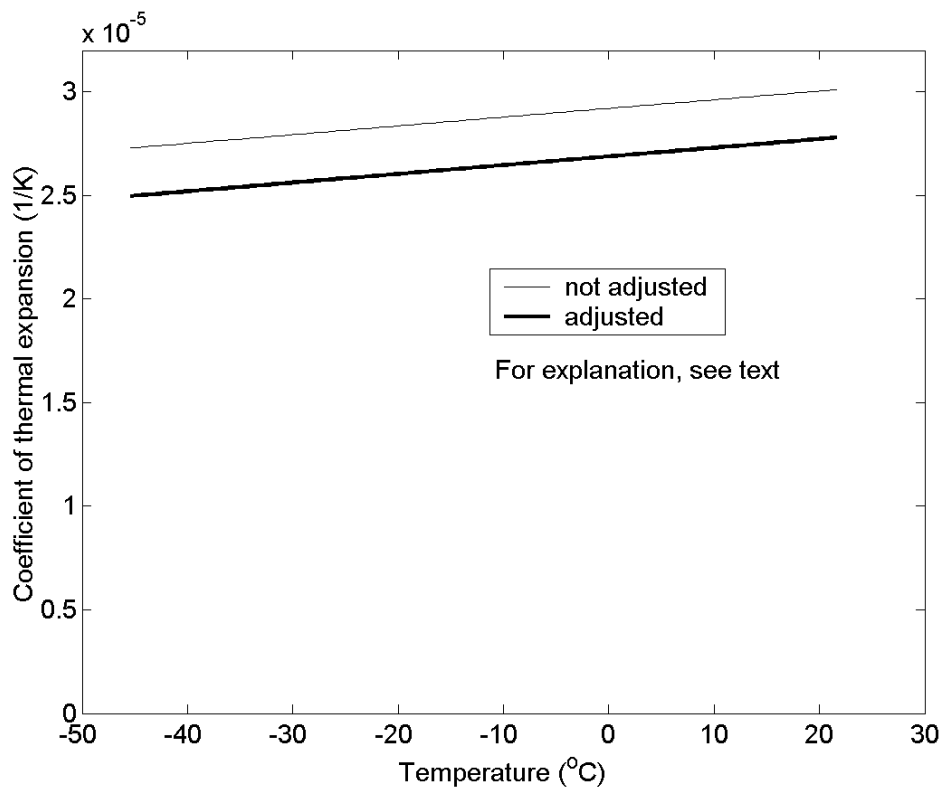


Figure 4 - Coefficient of thermal expansion at test measurement on a rod of aluminium alloy. Comparison between direct measured value and value corrected for the thermal expansivity of the equipment.

A measurement with a sample of 10.82 g of water placed in a plastic vessel was also made. The result is shown in Fig. 5. It is seen that the shape of the freezing peak is different from the shape of the melting peak. This test experiment is further discussed in the next section of the paper.

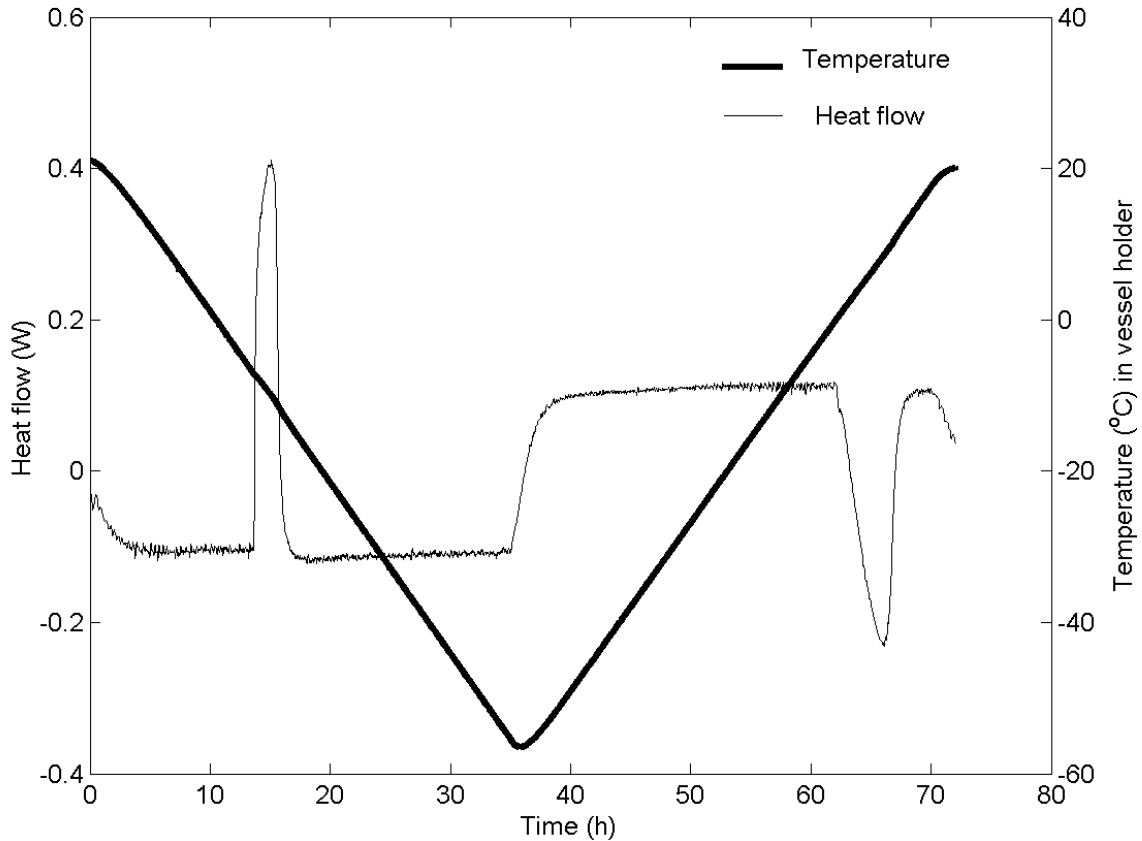


Figure 5 - Test measurement on 10.82 g of water: heat flow and temperature in vessel holder.

The equipment was made for the study of ice formation and length-change in cement-based materials. A first result of this type of measurement is presented in Fig. 6. A cylinder of micro-concrete, w/c-ratio 0.45 with an air content of 6% was dried at +105°C and thereafter vacuum saturated with water. A hole for the thermocouple had been made so the temperature could be measured in the center of the specimen. Before the start of the measurement the sample was wrapped in plastic foil to keep the moisture inside the specimen. There is no way to stop the water from moving from the inside of the specimen to the surface during freezing, but the plastic foil makes sure that most of the water goes back into the sample again during thawing. A piece of glass was glued on the top of the specimen to ensure free movement of the LVDT dilatometer. The sample was placed in the calorimeter and tested during a freeze-thaw cycle from +20°C to -70°C with a temperature scanning rate of 4.2 K/h and an isothermal period of seven hours at the lowest temperature.

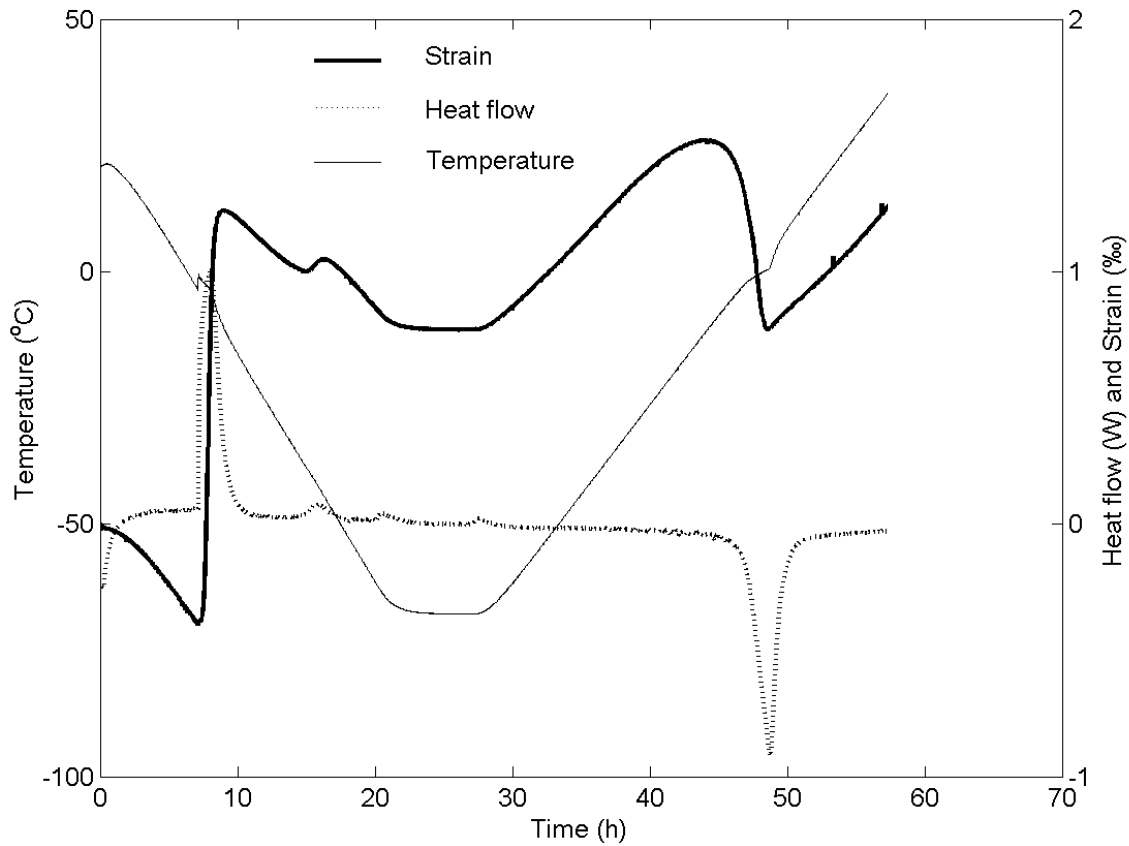


Figure 6 - Test measurement on micro-concrete. The temperature was measured in the center of the sample.

The length measurement shows that during the first large ice formation occurring at -4°C a large expansion takes place simultaneously with the large heat flow (ice formation). The smaller second peak in the heat flow measurement results in a minor expansion. Just before and after the isothermal period at -70°C small variations in the heat flow can be seen, but they are artefacts of the temperature cycle and do not result in any expansion. A large expansion during temperature increase, probably caused by the difference in thermal expansivity between the micro-concrete and the ice, is seen before the large contraction that occurs when the ice melts at about 0°C . When the temperature in the sample returns to $+20^{\circ}\text{C}$, a permanent length change of about 1% indicates that the sample has suffered internal damage.

Even if there is still work to do to increase the sensitivity and to improve the calibration coefficients it is already possible to study the different phenomena that occur during freezing and thawing of micro-concrete and their consequences.

5. COMPUTER SIMULATIONS

A thermal model of the calorimeter with heat capacities connected by thermal conductances was developed. It is a simple model that only includes the essential factors to model the overall temperature development during a measurement. The sample is modelled as two (isothermal) heat capacities and the reference is modelled as one (Fig. 7). The heat capacities used in the

model were calculated from the geometry, density and specific heat capacities of each part (Table 1).

The thermal conductances are more difficult to assess as they depend on thermal conductivities of the materials and their contact zones, air gap geometries, radiation, possible convective heat flow etc. For the present case initial parameters were calculated. Some of these were modified to get a better fit between simulation and measurement for the freezing peak (Table 2).

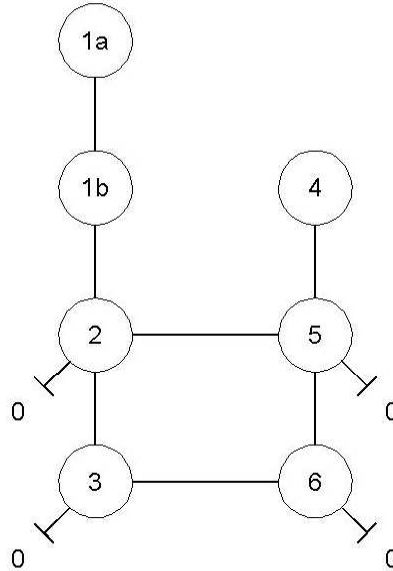


Figure 7 - The thermal model of the calorimeter. Each circle is a heat capacity (J/K) of a part of the calorimeter: sample and vessel (1a and 1b), vessel holder (2), sample side heat sink (3), reference and vessel (4), reference vessel holder (5) and reference side heat sink (6). The lines connecting the circles are thermal conductances (W/K). The short lines ending with a short perpendicular line are thermal conductances to the surrounding (0, the air of the freezer).

A simulation was made of the behaviour of the calorimeter during the measurement with 10.82 g water being cooled from +20°C to -60°C and back again. In the simulation the temperature at which water freezes was set to -7°C (the super-cooling freezing temperature observed during the measurement). The melting temperature was set to 0°C.

The simulation was made with forward differences in which at each time step the heat flow q_{ij} (W) between two heat capacities i and j are calculated with:

$$q_{ij} = k_{ij}(T_i - T_j) \quad (\text{Eq. 6})$$

Here, k_{ij} (W/K) is the thermal conductance between i and j . The temperature in heat capacity i is then updated with:

$$T_{i,new} = T_{i,old} + \frac{\Delta t}{C_i} \sum q \quad (\text{Eq. 7})$$

Here, $\sum q$ is the sum of all heat flows to heat capacity i , Δt (s) is the time-step in the simulation and C_i (J/K) is the heat capacity of i . In the present simulation a time step of 10 s was used and the ambient temperature was taken from the measurement file.

The freezing was modelled by checking if the temperature was below freezing temperature (-7°C) at the same time as 1a or 1b contained liquid water. If this was the case, an amount of water corresponding to the temperature decrease below the freezing temperature was frozen and the temperature was set back to the freezing temperature. The temperature thus stayed constant (at -7°C) during the freezing period. Melting was modelled in a similar way. The following data was used for the water: specific heat capacity (liquid): 4.18 J/g/K , specific heat capacity (ice): 2.2 J/g/K , and heat of fusion: 334 J/g .

As it has been difficult to theoretically calculate the thermal conductivities of the calorimeter (except for the conductivities of the thermo-couple plates) these were fitted to the experimental data in two steps. First the external conductances between air of freezer and heat sinks (0-3 and 0-6, cf. Fig. 7) were fitted so that the simulation results agreed with the temperature measured in the heat sinks. After that the internal conductances between the sample and the sample vessel holder (1a-1b and 1b-2) and between the reference and the reference vessel holder (4-5) were fitted to get a good agreement between the simulation results and the experimentally measured freezing peak.

Figure 8 shows the result of the simulation together with the result of the measurement. The double peaks in the simulation results are artefacts of that the sample is modelled in two parts. The outer part (1b) has to freeze first and stays at the freezing temperature until all water has frozen. It then takes some time before the freezing of the inner part (1a) takes place at the same rate. A similar phenomenon takes place during melting in the simulation.

It is seen that the whole process is modelled quite well by the simulation model, except the melting that is slower than the freezing, i.e. that melting cannot be modelled with the same simulation parameters as the freezing. Integration of the peaks gives:

- Freezing simulation: $3440 + 150 = 3590\text{ J} \rightarrow 10.7\text{ g water}$
- Freezing measurement: $3423 + 150 = 3573\text{ J} \rightarrow 10.7\text{ g water}$
- Melting simulation: $3540\text{ J} \rightarrow 10.6\text{ g water}$
- Melting measurement: $3732\text{ J} \rightarrow 11.2\text{ g water}$

Here the mass of water has been calculated with the heat of fusion at 0°C of 334 J/g , and the correction of 150 J for the freezing was calculated as:

$$(c_l - c_s)(T_m - T_f)m \quad (\text{Eq. 8})$$

Here c_l and c_s (J/g/K) are the specific heat capacities of liquid water and ice, T_m and T_f (K) are the temperatures of melting and freezing, and m (g) is the mass of water. This corrects for that the freezing peak is smaller than the melting peak because heat has been used to supercool liquid water from T_m to T_f (from 0 to -7°C).

The use of a model such as this is mainly to increase the understanding of how the instrument works. It can for example be used to simulate the calorimeter output from a calibration pulse or a freezing process. More detailed descriptions of the sample, e.g. for a mortar sample, can be developed and used to test phase-change models. The model can also give information on which factors that we need to investigate more closely, e.g. in the present model all parameters seems physically relevant except the surprisingly low thermal conductivities between sample/reference and the sample/reference vessel holders. The fact that the present model accurately models freezing, but not thawing is an indication that the model cannot handle cases both with and

without supercooling. Fitting the result to the equilibrium thawing instead of the non-equilibrium freezing (as was done in the present paper) will only give even lower thermal conductivities between sample/reference and the sample/reference vessel holder. The modelling of the freezing of supercooled water could probably also be improved. Here further investigations are needed.

Table 1 - Heat capacities C (J/K) used in the simulation model of the calorimeter. The figures have been calculated from the volumes and heat capacities of the different parts.

	C / J/K
1a inner part of sample	75 ¹
1b outer part of sample and vessel	75 ¹
2 sample vessel holder	450
3 sample side heat sink	2600
4 reference and vessel	320 ²
5 reference vessel holder	450
6 reference side heat sink	2600

1. For 10.82 g water used in experiment and simulation (no mortar sample).
2. For the plastic reference used during test measurement with 10.82 g water.

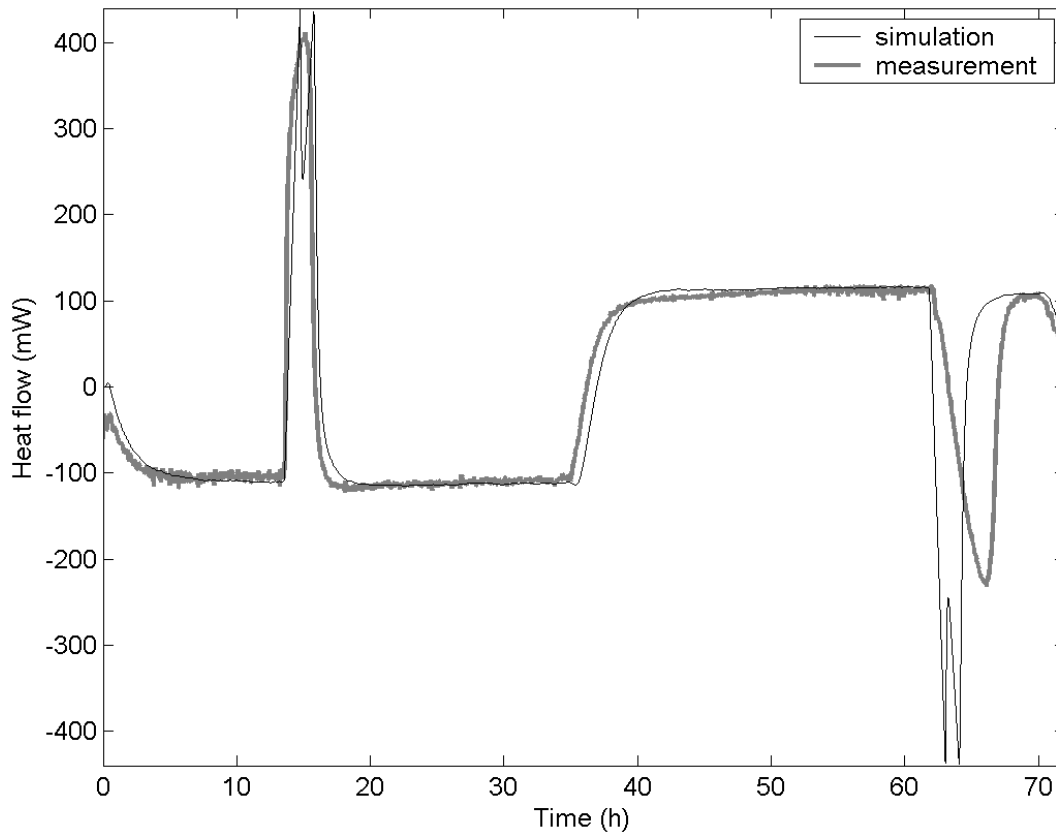


Figure 8 - Results from measurements with 10.82 g of water placed in a plastic container in the vessel. The double peaks seen in the simulation results are artefacts of the two-compartment model of the sample.

Table 2 - Thermal conductances k (W/K) used in the simulation model. The numbers refer to the different parts of the calorimeter (cf. Fig. 7). Most figures have been calculated from the thermal conductivity and geometry of the insulation (cf. table footnotes).

		k / W/K
1a-1b	in sample ¹	0.29
1b-2	sample and vessel to sample vessel holder ¹	0.29
2-3	heat flow sensors ²	1.70
2-5	through insulation	0.005
3-6	through insulation	0.013
4-5	reference and vessel to reference vessel holder ³	0.14
5-6	heat flow sensors ²	1.70
0-2	through insulation	0.010
0-3	through boundary layer ⁴	1.1
0-5	through insulation	0.010
0-6	through boundary layer ⁴	1.1

1. Fitted parameter.

2. Calculated from data from manufacturer (Thermoelectric Handbook 2002 [21]).

3. Fitted parameter.

4. Calculated with an apparent heat transfer coefficient of 25 W/m²/K between the heat sinks and the air of the freezer.

As seen in Table 2 some conductances are much lower than the others (0-2, 0-5, 2-5, and 3-6) and can probably be set to zero in a future simulation model.

6. CONCLUSIONS

A combined scanning calorimeter and dilatometer has been developed. At this early stage it shows promising results and can be used to study different phenomena occurring during freezing and thawing of cement based materials and other porous materials. The advantages with this instrument are the relatively large sample size, the simultaneous measurement of heat flow and dilation, and the easy and fast preparation of the specimens. This paper also contains construction details and calibration data.

7. FUTURE WORK

The combined scanning calorimeter and dilatometer will be used for measurements on mortar and concrete samples. Comparison with earlier measurements will also be made but these may be difficult as different measurement techniques and sample sizes have been used.

The following factors could be further investigated to improve the equipment:

- Electrical calibrations and measurements on water to more accurately determine the calorimetric calibration coefficients.
- Further work to investigate the discrepancy in the dilation measurements (discussed in connection with Fig. 4).
- Further work to improve the thermal model of the calorimeter.
- Developing a thermal model for mortar samples with which we can test phase-change models.

REFERENCES

1. Lindmark, S., 'Mechanisms of salt frost scaling of Portland cement-bound materials: Studies and hypothesis', Doctoral thesis, Division of Building Materials, Lund Institute of Technology, 1998.
2. Jepsen Tange, M., 'Salt frost scaling – interaction of transport mechanisms and ice formation in concrete', Doctoral thesis, Building Technology, Danish Technological Institute and Aalborg University, 2002.
3. Powers, T.C and Helmuth, R.A., 'Theory of volume changes in hardened Portland-cement paste during freezing', Proceedings, Highway Research Board 32, Bull. 46 1953.
4. Jacobsen, S., 'Scaling and cracking in unsealed freeze/thaw testing of Portland cement and silica fume concretes', Doctoral thesis, Division of Structural Engineering, Concrete section, The Norwegian Institute of Technology, 1995.
5. Kaufmann, J., 'Experimental Identification of Damage Mechanisms in Cementitious Porous Materials on Phase Transition of Pore Solution under Frost De-Icing Salt Attack', École Polytechnique Fédéral de Lausanne, Thèse No 2037, 1999.
6. Rønning, T., 'Freeze-thaw resistance of concrete, effect of: curing conditions moisture exchange and materials', Doctoral thesis, Department of Structural Engineering, Faculty of Civil and Environmental Engineering, Norwegian University of Science and Technology, Trondheim 2001.
7. Setzer, M.J., 'Development of the micro-ice-lens model', Frost Resistance of Concrete, Proceedings, Editors, Setzer, M.J., Auberg, R., Keck, H-J., Rilem Publications S.A.R.L, Canchan, 2002.
8. EU-project CONTECVET. Manual for assessing concrete structures affected by frost. Annex E: Effect of internal frost damage on mechanical properties of concrete, Div. of Building Materials, Lund Institute of Technology 2001.
9. Fagerlund, G., 'Critical degrees of saturation at freezing of porous and brittle materials', Doctoral thesis, Division of Building Material, Lund Institute of Technology, report 34, 1972.
10. Valore, R.C., 'Volume changes in small concrete cylinders during freezing and thawing', Journal of American Concrete Institute, vol 21, no 6, 1950.
11. Vourinen, J., 'On the behaviour of hardened concrete during freezing', The State Institute for Technical Research, Finland 1969.
12. Bager, D.H. and Sellevold, E.J., 'Ice Formation in Hardened Cement Paste, Part I – Room Temperature Cured Pastes With Variable Moisture Contents' Cement and Concrete Research, vol 16, pp. 709-720, 1986.

-
13. Bager, D.H. and Sellevold, E.J., 'Ice Formation in Hardened Cement Paste, Part II – Drying and Resaturation on Room Temperature Cured Pastes' Cement and Concrete Research, vol 16, pp. 835-844, 1986.
 14. Bager, D.H. and Sellevold, E.J., 'Ice Formation in Hardened Cement Paste, Part III – Slow Resaturation of Room Temperature Cured Pastes' Cement and Concrete Research, vol 17, pp. 1-11, 1987.
 15. Le Sage de Fontenay, C., 'Isdannelse i hærnet Cementpasta', Building Materials Laboratory, Department of Civil Engineering, Technical University of Denmark, 1982.
 16. Matala, S. 'Effects of carbonation on the pore structure of granulated blast furnace slag concrete', Concrete Technology, Faculty of Civil Engineering and Surveying, Helsinki University of Technology, 1995.
 17. Verbeck, G. & Klieger, P., 'Calorimeter-Strain Apparatus for Study of Freezing and Thawing Concrete', Bulletin 176, Highway Research Board, Washington, 1958.
 18. Fagerlund, G., 'Significance of critical degree of saturation at freezing of porous and brittle materials', ACI Symposium "Durability of concrete", Ottawa 1973, ACI Special publications, Detroit 1975.
 19. Penttala, V., 'Freezing-Induced Strains and Pressures in Wet Porous Materials and Especially in Concrete Mortars', Advanced Cement based Materials, vol 7, nr 1, 1998, pp 8-19.
 20. Penttala, V., 'Strains and Pressures Induced by Freezing Mortars Exposed in Sodium Chloride Solution', Concrete Science and Engineering, vol 1, pp 2-14, 1999
 21. Thermoelectric Handbook 2002, www.melcor.com

Partial Coefficient for Thermal Cracking Problems Determined by a Probabilistic Method



Martin Nilsson
Doctoral Student, Tech. Lic.
Department of Civil and Mining Engineering
Division of Structural Engineering
Luleå University of Technology
SE-971 87 Luleå, Sweden
E-mail: Martin.Nilsson@ce.luth.se



Lennart Elfgren
Professor, Tech. Dr.
Department of Civil and Mining Engineering
Division of Structural Engineering
Luleå University of Technology
SE-971 87 Luleå, Sweden
E-mail: Lennart.Elfgren@ce.luth.se

ABSTRACT

The aim of this work is to calculate partial coefficients for thermal cracking problems of young concrete and to compare the results with the values stated in the Swedish building code for bridges, [1]. The code values are only based on experiences and logical reasoning, whereas the calculated values form a more theoretical base for their determination. The coefficients are calculated with a probabilistic method. Various possible variations of the used variables have been studied showing the wide range of possible results depending on the input. However, with use of material properties and reasonable assumptions related to thermal cracking problems, fairly good agreement has been found between the stated values in the Swedish code [1] and the values obtained through the probabilistic method.

The calculated values are based on many assumptions and assumed values and should therefore not be seen as what is correct but rather more as an indication on the reasonableness of the values stated in the Swedish code. Further investigations, calculations and judgements must be performed before wider conclusions can be drawn.

Keywords: Partial coefficients, Safety factors, Young concrete, Probabilistic method, Cracking

1 INTRODUCTION

A structure or a structural member should be designed in such a way that safety and serviceability are always maintained. This means that no relevant limit state conditions should be exceeded with an in beforehand determined probability. For young concrete structures it is important to prevent surface and through cracks due to e.g. temperature and/or temperature gradients during the hydration phase. Such cracks do not affect the total bearing capacity of a structure, the safety, but can influence the aesthetics and cause leakage and durability problems, the serviceability, that must be taken care of by e.g. injection.

The risk of thermal cracking in young concrete structures is commonly estimated as the ratio between the calculated maximum tensile stress and the actual tensile strength. Alternatively, the ratio between the calculated maximum tensile strain and the actual ultimate tensile strain is used, which will be the case here. If a determined ratio is smaller than a so-called crack safety value, a structure is assumed to fulfil the requirements for avoiding thermal cracking. Depending on the effects of cracking and the accuracy in determining material properties, the Swedish building codes for bridges, [1], states different crack safety values as measures of the risk of cracking.

The risk of cracking due to temperature and temperature gradients can be estimated, according to [1], by three different methods. In Method 1 certain demands are specified on i.e. the casting and the air temperatures, the maximum cement content and the minimum value of the water cement ratio. Demands are also stated on the thickness and height of the structural members, the casting length, and when form stripping is allowed. In Method 2 and Method 3, which are more elaborate, certain values of the crack safety are prescribed depending on the accuracy in the determination of material data. Method 2 implies that requirements in a certain handbook, [2], should be applied. The requirements have been established by numerous thermal stress analyses. Further, material data that should be used are given in the code. In Method 3, the risk of cracking is estimated very accurately with tried and documented computer software and material properties.

The risk of cracking should not be larger than the partial coefficients given in Table 1, the crack safety values according to [1]. The environmental classes in the legend of the first column are according to the Swedish building code for concrete, [3]. Environmental class A2 stands for “Moderately reinforcement aggressive”, class A3 stands for “Very reinforcement aggressive” and class A4 stands for “Extremely reinforcement aggressive”, further see Section 4.2.

Table 1 - Partial coefficients derived as the inverse of the crack safety values for Method 2 and Method 3 given in [1]. For Method 2 values from the two right columns are used where C is the cement content [kg/m^3].

Environm. class	Method 3	Method 2	
	Complete material data	Material data given in the code $360 \leq C \leq 430 \text{ kg}/\text{m}^3$	$430 \leq C \leq 460 \text{ kg}/\text{m}^3$
A2	1.11	1.25	1.42
A3	1.18	1.33	1.54
A4	1.25	1.42	1.67

The crack safety values can be referred to what usually are called partial coefficients based on probabilistic methods, see e.g. [4], [5], [6], [7] and [8]. A method for determination of partial coefficients will be presented here. Further, a determination of partial coefficients for thermal cracking problems, that is the crack safety values in [1], will follow as an attempt to indicate the reasonableness in the stated values. The method and the results are more thoroughly presented and described in [8]. The determination is based on material properties, assumptions on load situations and other conditions typical for thermal cracking problems.

2 PARTIAL COEFFICIENTS

2.1 Limit state function and safety index

The safety against failure can be estimated by a limit state condition in terms of a resistance parameter r and a stress parameter s . The limit state condition, $\Theta(\cdot)$, can be expressed as the resistance parameter r reduced by the stress parameter s as

$$\Theta(\cdot) = r - s \geq 0 \quad (1)$$

Usually, the resistance parameter r is the material strength and the load parameter s is the stresses caused by acting loads. Depending on their relative size, the limit state condition is not exceeded if the resistance is larger than or equal to the stress, $r \geq s$, and it is exceeded if the resistance is smaller than the stress, $r < s$.

The two parameters are regarded as two normally distributed stochastic variables with given probability density functions, $f_r(r)$ and $f_s(s)$, see Figure 1a). From the presumption that the resistance parameter r and the stress parameter s are stochastic variables, the limit state condition is also a stochastic variable. Assuming the resistance parameter r and the stress parameter s being normally distributed also the limit state condition Θ is normally distributed with the probability density function $f_\Theta(\Theta)$, Figure 1b).

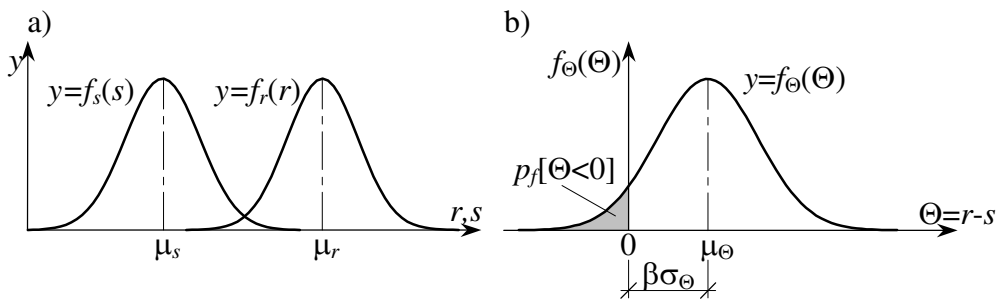


Figure 1 - a) Probability density functions for the stress parameter, $f_s(s)$, and the resistance parameter, $f_r(r)$, b) Probability density function for the limit state condition Θ , $f_\Theta(\Theta)$.

The probability of exceeding a limit state condition, $p_f[\Theta = r - s < 0]$, is equal to the area of the shaded surface in Figure 1b). In the figure, the distance, with the standard deviation σ_Θ as unit, from the mean value μ_Θ to the failure limit, $\Theta = 0$, is written as $\beta\sigma_\Theta$. The coefficient β is the so-called safety index, introduced by Cornell in [9], and is, according to the figure, determined as

$$\beta = \frac{\mu_{\Theta}}{\sigma_{\Theta}} \quad (2)$$

How much larger the resistance r should be than the stress s is often specified in building codes in different safety classes and through specified values of the safety index β . The safety index β is defined by a formal probability of failure, that is, of exceeding the limit state condition. The safety index β is often coupled to safety classes in building codes, see e.g. [6], [7], [10]. If the risk of human injuries is low, often referred to safety class 1, the probability of failure is $p_f = 10^{-4}$ and the safety index $\beta = 3.72$. The same principle applies to safety classes 2 and 3, see Table 2.

Table 2 - Correspondence between safety class, safety index and probability of failure, [1], [10].

Safety class	1	2	3
Safety index β	3.72	4.26	4.75
Probability of failure, p_f	10^{-4}	10^{-5}	10^{-6}

2.2 Partial coefficients

The partial coefficient method is based on characteristic values and partial coefficients for verification that prescribed safety requirements are fulfilled. Generally, for the limit state condition in Eq. (1), partial coefficients are used as follows

$$\Theta = r_d - s_d = \frac{r_c}{\gamma_r} - \gamma_s s_c \geq 0 \quad (3)$$

where d indicates design values, c indicates characteristic values and γ_r and γ_s are the partial coefficients for the resistance parameter r and the stress parameter s , respectively.

For the risk of thermal cracking of young concrete, the partial coefficients in Table 1 are the product of the partial coefficients for the resistance parameter r and the stress parameter s , $\gamma_r \gamma_s$, compare with Eq. (3),

$$\frac{r_c}{s_c} \geq \gamma_r \gamma_s \quad (4)$$

In this case, all partial coefficients have been collected in one coefficient limiting the ratio between the resistance parameter and the load parameter.

3 THE PROBABILISTIC METHOD

3.1 Equations for determination of partial coefficients

A method, further referred to as the probabilistic method, will be used to determine alternative values of the partial coefficients, safety values, for thermal cracking problems, given in Table 1.

The method has the advantage of being consequent but it also includes many approximations. The results can therefore not be used directly without additional judgements. The following determination of the partial coefficients will be formulated in terms of strains. The procedure in general is based on a method presented by Lars Östlund in [11], reprinted in [12], and adopted on thermal cracking problems in [8]. As design condition with partial coefficients for thermal cracking problems, Eq. (4) will be used as the limit state condition.

The resistance parameter r is defined as the product of a factor C_r describing uncertainties in the calculation method, of a factor a for the geometric quantity, a factor ρ transferring concrete strain in a test specimen at failure to concrete strain in real structures, and a factor ε that is the ultimate strain, see APPENDIX A.

$$r = C_r a \rho \varepsilon \quad (5)$$

The load parameter is defined as the product of a factor C_s describing uncertainties in the calculation method, a factor γ_R describing the restraint, see [8], and the sum of the thermal strain and the shrinkage induced strain, see APPENDIX A.

$$s = C_s \gamma_R (b \varepsilon_T + c \varepsilon_{sh}) \quad (6)$$

where b and c are deterministic coefficients that are used when either the temperature induced strain is of greater importance than the shrinkage strain, or the opposite.

By introducing

$$\frac{C_r}{C_s} = C \text{ with coefficient of variation } V_C = \sqrt{V_{C_r}^2 + V_{C_s}^2} \quad (7)$$

Eq. (5) and (6) in Eq. (1) give the limit state equation

$$\Theta(\cdot) = C a \rho \varepsilon - \gamma_R (b \varepsilon_T + c \varepsilon_{sh}) \quad (8)$$

When calculating partial coefficients by the probabilistic method, the following design values are used for the stochastic variables r , ε_T and ε_{sh} .

$$r_d = \mu_r \exp(-\alpha_r \beta V_r) \quad (9)$$

$$\varepsilon_{T,d} = \mu_T (1 - \alpha_T \beta V_T) \quad (10)$$

$$\varepsilon_{sh,d} = \mu_{sh} (1 - \alpha_{sh} \beta V_{sh}) \quad (11)$$

where α_r , α_T and α_{sh} are so-called sensitivity coefficients determined as

$$\alpha_i = \frac{\kappa_i}{\sqrt{\sum \kappa_i^2}} = \frac{\kappa_i}{\sqrt{\kappa_r^2 + \kappa_T^2 + \kappa_{sh}^2}}; \text{ with } i = r, T \text{ and } sh \quad (12)$$

which must fulfil the condition

$$\alpha_r^2 + \alpha_T^2 + \alpha_{sh}^2 = 1 \quad (13)$$

The sensitivity coefficients take values between -1 and 1 and are positive for favourable factors, the resistance parameters, and negative for unfavourable, the load/stress parameters. The larger the coefficient is, the larger the importance of the uncertainty is in the corresponding variable.

In the calculation of the partial coefficients for thermal cracking problems of concrete, it is very difficult to give any absolute values of the mean values of the strains of shrinkage and temperature changes. However, the relation between them is simpler to estimate. Therefore, a coefficient v_{sh} is introduced stating the ratio between the mean values of the strains of shrinkage and of the temperature change

$$v_{sh} = \frac{c\mu_{sh}}{b\mu_T} \quad (14)$$

Eqs. (9) to (11) and Eq. (14) in Eq. (8) give the design condition with design values of the variables

$$\frac{\mu_r}{b\gamma_R\mu_T} \exp(-\alpha_r\beta V_r) - (1 - \alpha_T\beta V_T) - v_{sh}(1 - \alpha_{sh}\beta V_{sh}) = 0 \quad (15)$$

By introducing the help variables

$$Z = \frac{\mu_r}{b\gamma_R\mu_T}$$

and

$$\psi_1 = (1 - \alpha_T\beta V_T) + v_{sh}(1 - \alpha_{sh}\beta V_{sh})$$

Eq. (15) can be re-written as

$$Z = \psi_1 \exp(\alpha_r\beta V_r) \quad (16)$$

By introducing partial coefficients for the design values in Eqs. (9) through (11) one obtain

$$r_d = \frac{r_c}{\gamma_r} = \frac{\mu_r}{\gamma_r} \exp(-k_r V_r) \quad (17)$$

$$s_d = \gamma_s \gamma_R (b\varepsilon_{T,c} + c\varepsilon_{sh,c}) = \gamma_s \gamma_R (b\mu_T(1 + k_T V_T) + c\mu_{sh}(1 + k_{sh} V_{sh})) \quad (18)$$

where r_c , $\varepsilon_{T,c}$ and $\varepsilon_{sh,c}$ are the characteristic values of the resistance parameter, the temperature and the shrinkage induced strains, respectively. The limit state condition is then written as

$$\frac{\mu_r}{\gamma_r} \exp(-k_r V_r) - \gamma_s \gamma_R (b\mu_T(1 + k_T V_T) + c\mu_{sh}(1 + k_{sh} V_{sh})) \geq 0 \quad (19)$$

The coefficient k depends of actual fractile value for normal distribution variables, see Table 10

in APPENDIX A. In the same way as above, with $Z = \mu_r/b\gamma_R\mu_T$, $v_{sh} = c\mu_{sh}/b\mu_T$ and $\psi_2 = (1+k_T V_T)+v_{sh}(1+k_{sh} V_{sh})$, Eq. (19) can be re-written as

$$\gamma_s \gamma_r \leq \frac{Z}{\Psi_2} \exp(-k_r V_r) = \frac{Z}{\Psi_2} \frac{r_c}{\mu_r} \quad (20)$$

By calculating Z , see APPENDIX A, and r_c/μ_r by Eq. (A.4) with $x_{i,c}/\mu_i = \exp(-\alpha_i \beta V_i) = \exp(-k_i V_i)$, the partial coefficient $\gamma_r \gamma_s$ can be determined.

More thorough descriptions of the determination of the partial coefficients can be seen in APPENDIX A and references [8], [11] and [12].

3.2 Numerical values

Varying the variables shown in Table 3 and keeping all others constant in the equations above, calculations of partial coefficients for thermal cracking problems of young concrete have been performed.

v_{sh} is defined in Eq. (14) and states the ratio between the mean values of the strains of shrinkage and of the strains of temperature change. b and c are varied to simulate situations where one of the two strain components has smaller or larger influence. Especially in high strength concrete the shrinkage is considerable implying larger values of c . V_ε is the coefficient of variation of the actual concrete (actual ultimate strain ε_{cu}). V_C is the coefficient of variation of the methods used for estimating the risk of thermal cracking. Compare V_C with Methods 1 to 3 in Section 1 where e.g. $V_C = 0.15$ for Method 1, $V_C = 0.10$ for Method 2 and $V_C = 0.05$ for Method 3. These values are just an attempt to estimate the accuracy in the methods and should not be seen as what is correct. The safety index β is varied to coincide with safety classes 1 and 3 with probabilities of failure of 10^{-4} and 10^{-6} respectively, see Table 2.

Table 3 - Variables varied in the determination of partial coefficients for thermal cracking problems.

Variable	Values
v_{sh}	$0.01 \frac{c}{b}$, $0.20 \frac{c}{b}$, $0.50 \frac{c}{b}$, $1.00 \frac{c}{b}$, $2.00 \frac{c}{b}$
b	1/3, 1, 3
c	1/3, 1, 3
V_ε	0.05, 0.10, 0.15, 0.20, 0.25
V_C	0.05, 0.10, 0.15, 0.20, 0.25
β	3.72, 4.75

The coefficient of variation of the temperature induced strains is given the value $V_T = 0.08$ according to [16]. The coefficient of variation of the shrinkage is given the value $V_{sh} = 0.20$. This value is a bit smaller than what can be determined from [17]. The values of k_T and k_{sh} are both 1.65 coinciding with 95 % fractile values of the temperature and shrinkage induced strains, re-

spectively, see Table 4.

The coefficients of variations of the geometry parameter V_a and of the factor transferring strength in test specimens to real structures V_ρ are both given the value 0, that is $V_a = 0$ and $V_\rho = 0$. The coefficient of variation of the geometry is assumed to be very low since in civil engineering structures, any divergences from the right measures do not significantly affect the risk of thermal cracking. For the concrete ultimate strain, 45% fractile value is assumed giving $k_\varepsilon = 0.13$. The coefficient k is for normal distribution variables and can be found in general statistic textbooks, see Table 10 in APPENDIX A. The value of the ultimate strain for the concrete is chosen slightly below the mean value bearing in mind that thermal cracking only causes flaws and costs for repair and reduction of the life of the structure but not total failure. For the accuracy in the design method C , for the geometry parameter a and for the factor transferring the ultimate strain in test specimens to real structures ρ , the coefficient k is chosen $k_C = k_a = k_\rho = 1.65$ assuming 5% fractile values, see Table 4 below and Table 10 in APPENDIX A.

Table 4 - Constant values for the resistance parameters C , a , ρ and ε and the load parameters ε_T and ε_{sh} used in the determination of the partial coefficients.

k_C	V_a	k_a	V_ρ	k_ρ	k_ε	V_T	k_T	V_{sh}	k_{sh}
1.65	0	1.65	0	1.65	0.13	0.08	1.65	0.20	1.65

3.3 Calculation of partial coefficients

Example of calculation of partial coefficients

The following presumptions and values are used to illustrate the calculation of partial coefficients. Let the influence of the imposed volume changes be equal, $b = c = 1$. The mean value of the volume change due to shrinkage is one hundredth of the mean value of the imposed volume change due to the temperature change, $v_{sh} = 0.01 \cdot 1/1 = 0.01$. Further, the variation coefficients of the strength of the concrete and the calculation method are assumed to be five percent, $V_\varepsilon = V_C = 0.05$. The safety index $\beta = 3.72$ refers to safety class 1. The following values for the resistance parameter, the sensitivity values α and the help values ψ , N and Z are obtained, Table 5 and Table 6.

Table 5 - Calculated values for the resistance parameter.

V_r	C_c/μ_C	a_c/μ_a	ρ_c/μ_ρ	$\varepsilon_c/\mu_\varepsilon$	r_c/μ_r
0.071	0.921	1.000	1.000	0.994	0.915

Table 6 - Calculated sensitivity values α and help-values ψ_1 , N and Z .

α'_{sh}	α_T	ψ_1	N	α_φ	α_T	α_r	Z
-0.017	-0.682	1.213	0.117	-0.017	-0.682	0.731	1.470

The partial coefficient for this case is then calculated as, Eq. (20)

$$\gamma_r \gamma_s = \frac{Z}{\psi_2} \frac{r_c}{\mu_r} = \frac{1.470}{(1 + 1.65 \cdot 0.08) + 0.01(1 + 1.65 \cdot 0.20)} 0.915 = 1.174$$

implying that the resistance parameter must be about 1.17 times larger than the load parameter for not exceeding the limit state condition.

Final calculation of partial coefficients

All the partial coefficients calculated with values according to the description and Table 3 above are presented in Figure 2 to Figure 6 below. In all the diagrams, the curves from the lowest to the upper most one represent $V_C = 0.05, 0.10, 0.15, 0.20$ and 0.25 , respectively. See [8] for more descriptions of the calculations and the results.

In Figure 2 to Figure 6 it can be seen that with increased safety index β , the partial coefficient $\gamma_r \gamma_s$ increases and is varying over a larger range depending on the values of V_C . When the coefficient b increases also the partial coefficient increases, and when b decreases the partial coefficient decreases, compare Figure 3 and Figure 4 with Figure 2. For the coefficient c , the opposite is valid. When c increases, the partial coefficient decreases and when c decreases, the partial coefficient increases, compare Figure 5 and Figure 6 with Figure 2.

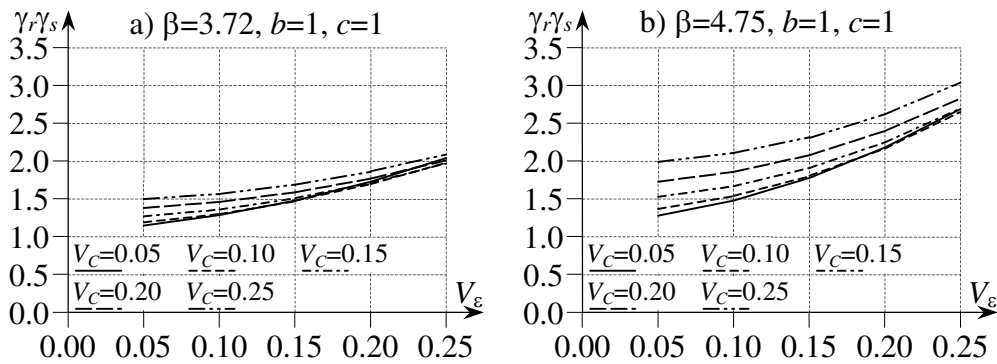


Figure 2 - Partial coefficient $\gamma_r \gamma_s$ for a) $\beta=3.72$, $b=1$ and $c=1$, b) $\beta=4.75$, $b=1$ and $c=1$.

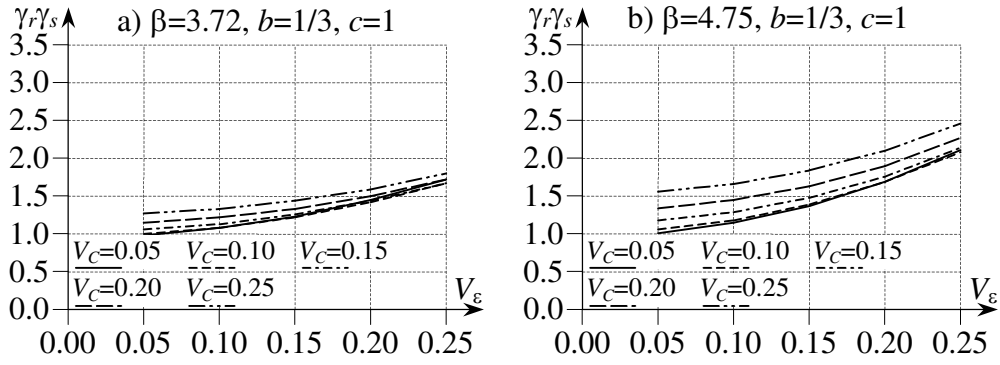


Figure 3 - Partial coefficient $\gamma_r \gamma_s$ for a) $\beta=3.72$, $b=1/3$ and $c=1$, b) $\beta=4.75$, $b=1/3$ and $c=1$.

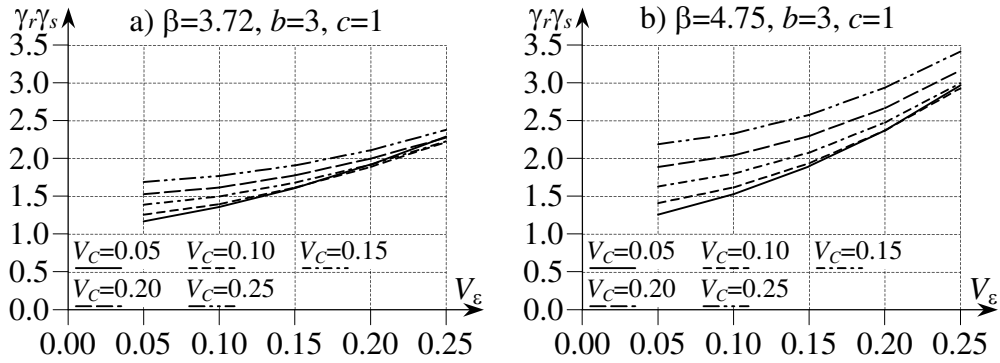


Figure 4 - Partial coefficient $\gamma_r \gamma_s$ for a) $\beta=3.72$, $b=3$ and $c=1$, b) $\beta=4.75$, $b=3$ and $c=1$.

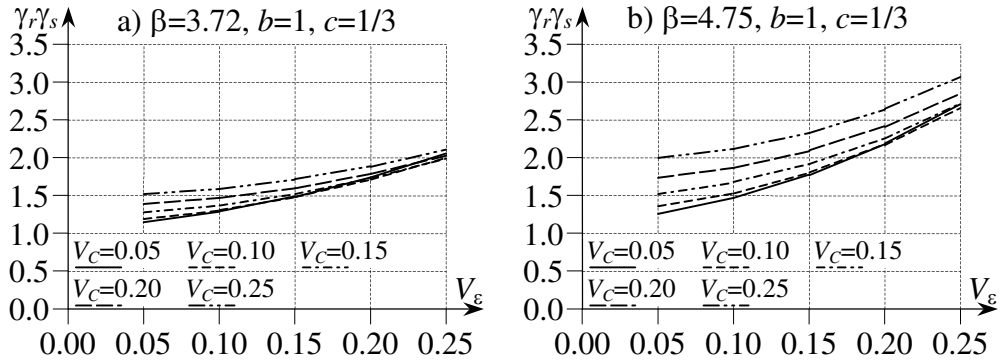


Figure 5 - Partial coefficient $\gamma_r \gamma_s$ for a) $\beta=3.72$, $b=1$ and $c=1/3$, b) $\beta=4.75$, $b=1$ and $c=1/3$.

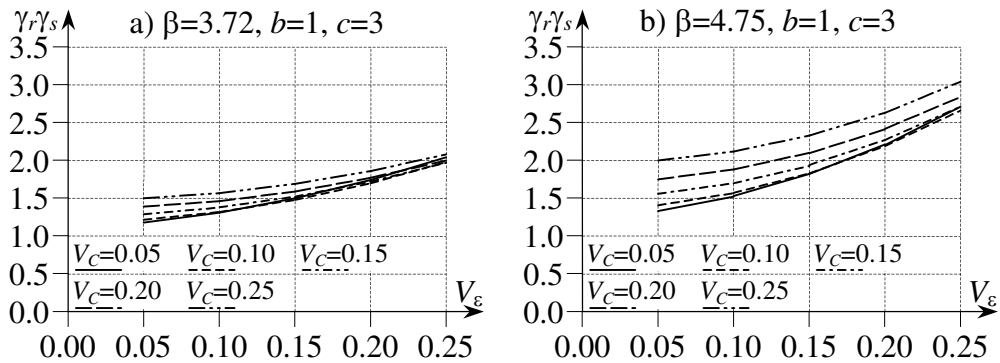


Figure 6 - Partial coefficient $\gamma_r \gamma_s$ for a) $\beta=3.72$, $b=1$ and $c=3$, b) $\beta=4.75$, $b=1$ and $c=3$.

4 RESULTS

4.1 Final values of partial coefficients

Final values of the partial coefficient $\gamma_r\gamma_s$ are determined from the previous calculations with $b = c = 1$, $\beta = 3.72$ and with coefficients of variation, $V_C = 0.05$ and $V_\varepsilon = 0.05, 0.10$ and 0.15 . The values are chosen to coincide with the first row in Table 1. For Method 3 (the column of complete material data) the models of analysis (computer software) are very well documented and tried and should give results not varying much from reality. Therefore, the coefficient of variation for the method of calculation is chosen to be small, $V_C = 0.05$. For Method 2, (columns for material data given in [1]) lots of calculations and judgements are behind, [2], implying good accuracy of the analyses, again $V_C = 0.05$. The differences in accuracy of material data are taken into account by varying the coefficient of variation of the material V_ε as stated, $V_\varepsilon = 0.05, 0.10$ and 0.15 . Again, $k_T = k_{sh} = 1.65$ for 95 % fractile values. Further, as an extension of the final determination of the partial coefficients, 55 % fractile values are assumed for the temperature and the shrinkage induced strains to coincide with the assumed fractile value of the ultimate strain (45 % fractile), see Section 3.2. For environmental class A2 and $V_\varepsilon = 0.05, 0.10$ and 0.15 , the partial coefficient $\gamma_r\gamma_s$ is taken as the values of the lowest curve in Figure 2a) presented in Table 7.

Table 7 - Partial coefficient $\gamma_r\gamma_s$ from calculation with the probabilistic method for environmental class A2 and $V_\varepsilon = 0.05, 0.10$ and 0.15 .

Environm. class	k_T, k_{sh}	Complete	Material data given in the code	
		material data $V_\varepsilon=0.05$	$360 \leq C \leq 430 \text{kg/m}^3$ $V_\varepsilon=0.10$	$430 \leq C \leq 460 \text{kg/m}^3$ $V_\varepsilon=0.15$
A2	0.13 (55% fractile)	1.36	1.52	1.75
	1.65 (95% fractile)	1.15	1.29	1.48

4.2 Effects of exceeding the limit state condition

The calculation of partial coefficients above is chosen to be valid for environmental class A2. The effects of exceeding the limit state condition (cracking) in a structural member are smaller in environmental class A2 than in classes A3 and A4. Therefore an extra partial coefficient γ_n is introduced. The values of the extra partial coefficient γ_n are chosen as the mean ratio between the values in the rows in Table 1, see Table 8.

Table 8 - Partial coefficient γ_n depending on environmental classes.

	Environmental class		
	A2	A3	A4
γ_n	1.00	1.07	1.14

Final values of the partial coefficient $\gamma_r\gamma_s$ are obtained from Table 7 with partial coefficient γ_n in Table 8, see Table 9.

Table 9 - Final values of partial coefficient $\gamma_r\gamma_s$ as determined by probabilistic method.

Environm. class	k_T, k_{sh}	Complete material data	Material data given in the code	
			$360 \leq C \leq 430 \text{kg/m}^3$	$430 \leq C \leq 460 \text{kg/m}^3$
A2	0.13 (55% fractile)	1.36	1.52	1.75
	1.65 (95% fractile)	1.15	1.29	1.48
A3	0.13 (55% fractile)	1.45	1.62	1.87
	1.65 (95% fractile)	1.23	1.38	1.58
A4	0.13 (55% fractile)	1.56	1.74	2.00
	1.65 (95% fractile)	1.32	1.48	1.70

A comparison with the values that are stated in [1] and the values of the partial coefficients obtained by the probabilistic method are depicted in Figure 7. As can be seen, the values for $k_T = k_{sh} = 1.65$ (95 % fractile values) are little higher than the values given in [1]. The values show good agreement even though the uncertainties in the chosen values of the variables used in the probabilistic method are large and that the partial coefficients stated in [1] only are based on experiences. For $k_T = k_{sh} = 0.13$ (55 % fractile values), the partial coefficients are much higher than the values in [1]. The reason for this is that with only 55 % fractile values of the temperature and the shrinkage induced strains, the risk of exceeding these values is increased. This implies an increased risk of exceeding the limit state condition, whereupon higher partial coefficients are needed.

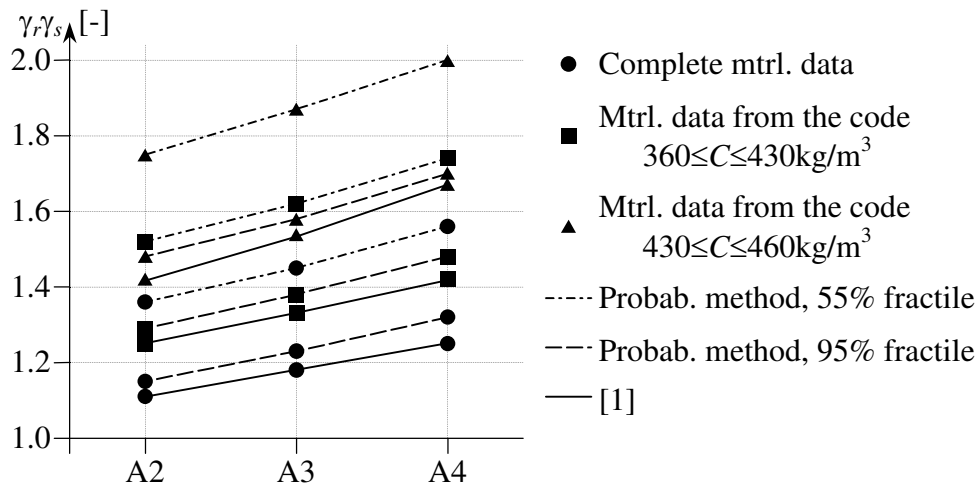


Figure 7 - Comparison between partial coefficients stated in [1] and partial coefficients obtained by the probabilistic method.

5 DISCUSSION

It is possible to calculate partial coefficients for thermal cracking problems of young concrete. The values presented above coincide well with the crack safety values stated in the Swedish building code for bridges, [1]. However, the calculated values of the partial coefficient are based on many assumptions and simplifications and they shall not be seen as what is absolutely true right, further judgements are always necessary.

The used coefficients of variation of the thermal changes and of the shrinkage need further investigation. The values are roughly taken from [16] and are only assumed values that have not been well verified.

The crack safety values in [1] are all based on experience, so also these values are a bit vague. The calculated partial coefficients presented here can be seen as an attempt to verify the values in [1]. However, all estimations of the risks of thermal cracking of young concrete have to be based on more judgements and analyses of the problems as a whole rather than on the crack safety values given in [1].

The differences in the partial coefficient between the environmental classes need further investigations. The values that are stated in [1] are only based on logical arguments by the persons who have written the code, meaning that higher environmental class needs higher partial coefficients.

ACKNOWLEDGEMENT

The authors thank Professor Emeritus Lars Östlund for his way of describing the methodology behind the determination of the partial coefficients. Thanks are also sent to Professor Emeritus Krister Cedervall, Chalmers University of Technology, for his thorough and dedicated work as leader of the discussion at Martin Nilsson's licentiate seminar. Finally, Associate Professor Jan-Erik Jonasson is thanked for his contributions in the field of thermal cracking of young concrete and material properties of concrete.

REFERENCES

- [1] BRO 94 (1999). *BRO94 Allmän teknisk beskrivning för broar, 9. Förteckning*. (General Technical Description for Bridges, 9. Catalogue). Borlänge, Sweden: Swedish National Road Administration. Publ 1999:20. pp. 139. ISSN 1401-9612. (In Swedish).
Bro 2002 (2002). *Bro 2002. Allmän teknisk beskrivning för broar, 4 Betongkonstruktioner*. (General Technical Description for Bridges, 4. Concrete structures). Borlänge, Sweden: Swedish National Road Administration. (In Swedish).
- [2] Emborg, M, Bernander, S, Ekefors, K, Groth, P & Hedlund, H (1997). *Temperatursprickor i betongkonstruktioner - Beräkningsmetoder för hydratationsspänningar och diagram för några vanliga typfall* (Temperature Cracks in Concrete Structures - Calculation Methods for Hydration Stresses and Diagrams for some Common Typical Examples). Luleå, Sweden: Luleå University of Technology. Technical Report 1997:02. 100 pp. ISSN 1402-1536. (In Swedish).
- [3] BBK94 (1994). *Boverkets handbok om betongkonstruktioner*. (The Swedish Building Administrations Handbook on Concrete Structures). Part 2 - Material, Performance and Control. Stockholm, Sweden: The Swedish Building Administration, Division of Buildings. pp. 116. ISBN 91-7332-687-9. (In Swedish).

- [4] Schneider, J (1997). Introduction to Safety and Reliability of Structures. In: *Structural Engineering Documents, 5*. Zürich: IABSE, International Association for Bridges and Structural Engineering. 138 pp.
- [5] AK79/81 (1982). *Allmänna regler för bärande konstruktioner. Principer, rekommendationer och kommentarer samt exempel på tillämpning*. (General Regulations for Structures. Principles, Recommendations, Comments and Examples of Application). Stockholm, Sweden: Statens Planverk, Rapport nr 50, Liber 1982, pp. 159. ISBN 91-38-07090-1. (In Swedish).
- [6] NKB78 (1978). *Retningslinier för last- og sikkerhetsbestemmelser for baerende konstruktioner* (Guiding Rules for Loads and Safety Regulations for Structures). NKB-rapport nr. 35. 146 pp. ISBN 87-503-2951-0. (In Swedish).
- [7] NKB87 (1987). *Retningslinier för last- og sikkerhetsbestemmelser for baerende konstruktioner* (Guiding Rules for Loads and Safety Regulations for Structures). NKB-rapport nr. 55. 107+55 pp. ISBN 87-503-6991-1, ISSN 0359-9981. (In Swedish).
- [8] Nilsson, M (2001). *Thermal Cracking of Young Concrete - Partial Coefficients, Restraint Effects and Influence of Casting Joints*. Luleå, Sweden: Division of Structural Engineering, Luleå University of Technology. Licentiate Thesis 2000:27. pp. 267.
- [9] Cornell, C A (1969). A probability-based structural code. In: *ACI Journal, Vol. 66*, pp. 974-985.
- [10] BBK94 (1995). *Boverkets handbok om betongkonstruktioner*. (The Swedish Building Administrations Handbook on Concrete Structures). Part 1 - Design. Stockholm, Sweden: The Swedish Building Administration, Division of Buildings. pp. 185. ISBN 91-7147-235-5. (In Swedish).
- [11] Östlund, L (1997). *Studium av erforderligt värde på partialkoefficienten för tåglast vid dimensionering av järnvägsbroar* (Study of Necessary Value of the Partial Coefficient for Load of Trains at Design of Railway Bridges). Borlänge, Sweden: Swedish Railroad Administration. Investigation on behalf of the Swedish Railroad Administration. pp. 19. (In Swedish).
- [12] Nilsson, M, Ohlsson, U & Elfgren, L (2000). *Partialkoefficienter för betongbroar längs Malmbanan* (Partial Coefficients for Concrete Bridges along Malmbanan). Luleå, Sweden: Luleå University of Technology. Technical report 1999:03. 66 pp. ISSN 1402-1536. (In Swedish).
- [13] Larson, M (2000). *Estimation of Crack Risk in Early Age Concrete*. Luleå, Sweden: Division of Structural Engineering, Luleå University of Technology. Licentiate Thesis 2000:10. pp. 170.
- [14] Jonasson, J-E, Wallin, K, Emborg, M, Gram, A, Saleh, I, Nilsson, M, Larson, M and Hedlund, H (2001). *Tempertursprickor i betongkonstruktioner – Handbok med diagram för sprickriskbedömning inklusive åtgärder för några typfall; Del D och E* (Temperature cracks in concrete structures - Handbook with diagrams for crack risk estimation including measures for some typical cases). Luleå, Sweden: Division of Structural Engineering, Luleå University of Technology. Technical Report 2001:14. (In Swedish, in progress).
- [15] ConTeSt Pro (1999). *Användarhandbok - ConTeSt Pro* (Users manual - Program for Temperature and Stress Calculations in Concrete). Developed by JEJMS Concrete AB in cooperation with Luleå University of Technology, Cementa AB and Peab Öst AB. Danderyd, Sweden: Cementa AB. pp. 207. (In Swedish).
- [16] Jonasson, J-E, Emborg, M & Bernander, S (1994). Temperatur, mognadsutveckling och egenspanningar i ung betong (Temperature, Maturity Growth and Eigenstresses in Young Concrete). In: *Betonghandbok - Material*. (Concrete Handbook - Material). Edition 2. Stockholm, Sweden: AB Svensk Byggtjänst and Cementa AB. pp. 547-607. ISBN 91-7332-709-3. (In Swedish).

- [17] Jonasson, J-E (1994). Krympning hos hårdnad betong (Shrinkage in Hardened Concrete). In: *Betonghandbok - Material*. (Concrete Handbook - Material). Edition 2. Stockholm, Sweden: AB Svensk Byggtjänst and Cements AB. pp. 524-545. ISBN 91-7332-709-3. (In Swedish).

APPENDIX A

Below a derivation follows of equations used in the determination of partial coefficients for thermal cracking problems.

A.1 Resistance parameter

The resistance parameter r is expressed as, [11]

$$r = C_r a \rho \varepsilon \quad (\text{A.1})$$

where C_r is a factor describing uncertainties in the calculation method on the resistance parameter such as determination of material properties. C_r is a stochastic variable with mean μ_{C_r} and coefficient of variation V_{C_r} . a is a geometric quantity (e.g. cross-section area). a is a stochastic variable with mean μ_a and coefficient of variation V_a . ρ is a factor transferring concrete strain from test specimen at failure to concrete strain in real structures. ρ is a stochastic variable with mean μ_ρ and coefficient of variation V_ρ . ε is the actual concrete ultimate strain. ε is a stochastic variable with mean μ_ε and coefficient of variation V_ε . The stochastic variables r , C_r , a , ρ and ε are assumed to be logarithmic normally distributed.

The mean value of the resistance parameter is

$$\mu_r = \mu_{C_r} \mu_a \mu_\rho \mu_\varepsilon \quad (\text{A.2})$$

and the coefficient of variation, if terms of higher order are neglected,

$$V_r \approx \sqrt{V_{C_r}^2 + V_a^2 + V_\rho^2 + V_\varepsilon^2} \quad (\text{A.3})$$

Eq. (A.1) divided by Eq. (A.2) gives, if using characteristic values,

$$\frac{r_c}{\mu_r} = \frac{C_{rc}}{\mu_{C_r}} \frac{a_c}{\mu_a} \frac{\rho_c}{\mu_\rho} \frac{\varepsilon_c}{\mu_\varepsilon} \quad (\text{A.4})$$

which will be used further on in the final calculation of the partial coefficients, see Eq. (A.21) below.

A.2 Load parameter

The load parameter s for thermal cracking problems can be formulated, in terms of strains, as

$$s = C_s \gamma_R (b(\varepsilon_{T1} + \varepsilon_{T2}) + c\varepsilon_{sh})$$

where C_s is uncertainties in the calculation method on the load parameter and is assumed to have the same value for all the loads. C_s describes uncertainties in the determination of the strains by e.g. manual methods, see [13] and [14], or by finite element calculations, see [15]. C_s is a stochastic variable with mean μ_{C_s} and coefficient of variation V_{C_s} . γ_R is the coefficient of restraint and is a deterministic coefficient, $0 \leq \gamma_R \leq 1$. For further explanations and the determination of the coefficient of restraint, see [8]. ε_{T1} is the non-elastic strain of volume changes from differences between the casting temperature and the adjacent temperature. ε_{T2} is the non-elastic strain

of volume changes from differences between the maximum temperature and the casting temperature. Below, the temperature-induced strains are combined into one parameter, ε_T , which is a stochastic variable with mean μ_T and coefficient of variation V_T . ε_{sh} is the strain of volume changes from shrinkage and is a stochastic variable with mean μ_{sh} and coefficient of variation V_{sh} . b and c are both deterministic coefficients, $0 \leq b$ and $0 \leq c$. The stochastic variables ε_T and ε_{sh} are assumed to be normally distributed. The deterministic coefficients b and c are used when either the temperature-induced strain is of greater importance than the shrinkage strain, or the opposite. Now, the load parameter is

$$s = C_s \gamma_R (b\varepsilon_T + c\varepsilon_{sh}) \quad (\text{A.5})$$

The variables are put together so that the mean value of the stress parameter is

$$\mu_s = \gamma_R (b\mu_T + c\mu_{sh}) \quad (\text{A.6})$$

By introducing the following relation

$$\frac{C_r}{C_s} = C; \quad V_C = \sqrt{V_{C_r}^2 + V_{C_s}^2} \quad (\text{A.7})$$

the limit state condition, Eq. (1), is simplified to

$$\Theta(\cdot) = Cap\varepsilon - \gamma_R (b\varepsilon_T + c\varepsilon_{sh}) \quad (\text{A.8})$$

A coefficient v_{sh} is introduced stating the ratio between the mean values of the strains of shrinkage and of the temperature change

$$v_{sh} = \frac{c\mu_{sh}}{b\mu_T} \quad (\text{A.9})$$

A.3 Design condition

When calculating partial coefficients by the probabilistic method, the following design values and help values κ are used for the stochastic variables r , ε_T and ε_{sh} .

$$r_d = \mu_r \exp(-\alpha_r \beta V_r) \quad \kappa_r = r_d V_r \quad (\text{A.10})$$

$$\varepsilon_{T,d} = \mu_T (1 - \alpha_T \beta V_T) \quad \kappa_T = -b\gamma_R \mu_T V_T \quad (\text{A.11})$$

$$\varepsilon_{sh,d} = \mu_{sh} (1 - \alpha_{sh} \beta V_{sh}) \quad \kappa_{sh} = -c\gamma_R \mu_{sh} V_{sh} \quad (\text{A.12})$$

When using design values in Eq. (3), the equal sign is valid, which together with Eq. (A.5) gives

$$r_d - b\gamma_R \varepsilon_{T,d} - c\gamma_R \varepsilon_{sh,d} = 0 \quad (\text{A.13})$$

In the expressions above, α are so-called sensitivity coefficients determined as

$$\alpha_i = \frac{\kappa_i}{\sqrt{\sum \kappa_i^2}} = \frac{\kappa_i}{\sqrt{\kappa_r^2 + \kappa_T^2 + \kappa_{sh}^2}}; \quad \text{with } i = r, T \text{ and } sh \quad (\text{A.14})$$

which must fulfil the condition

$$\alpha_r^2 + \alpha_T^2 + \alpha_{sh}^2 = 1 \quad (\text{A.15})$$

$c\mu_{sh} = v_{sh}b\mu_T$ according to Eq. (A.9) and design values according to Eqs. (A.10) to (A.12) inserted in Eq. (A.13) give

$$\frac{\mu_r}{b\gamma_R\mu_T} \exp(-\alpha_r\beta V_r) - (1 - \alpha_T\beta V_T) - v_{sh}(1 - \alpha_{sh}\beta V_{sh}) = 0 \quad (\text{A.16})$$

By introducing the help variables

$$Z = \frac{\mu_r}{b\gamma_R\mu_T}$$

and

$$\psi_1 = (1 - \alpha_T\beta V_T) + v_{sh}(1 - \alpha_{sh}\beta V_{sh}) \quad (\text{A.17})$$

Eq. (A.16) is simplified to

$$Z \exp(-\alpha_r\beta V_r) - \psi_1 = 0$$

where from

$$Z = \psi_1 \exp(\alpha_r\beta V_r) \quad (\text{A.18})$$

Z can be determined if the values of α_i (with $i = r, T$ and sh), β , v_{sh} , b , c and V_i are known. The steps for calculating Z can be as follows:

- (1) A value of α'_{sh} is assumed
- (2) $\alpha'_T = \frac{\kappa_T}{\sqrt{\sum \kappa_i^2}} = \frac{-b\gamma_R\mu_T V_T}{-c\gamma_R\mu_{sh} V_{sh}} \alpha'_{sh} = \frac{V_T \alpha'_{sh}}{v_{sh} V_{sh}}$ is calculated
- (3) ψ is calculated with Eq. (A.17), α'_{sh} and α'_T
- (4) $r_d = \mu_r \exp(-\alpha_r\beta V_r) = \mu_r \frac{\psi_1}{Z} = b\gamma_R\mu_T \psi_1$ and $\kappa_r = r_d V_r$ are calculated
- (5) $N = \frac{\sqrt{\sum \kappa_i^2}}{b\gamma_R\mu_T} = \sqrt{(V_T)^2 + (v_{sh} V_{sh})^2 + (\psi_1 V_r)^2}$
- (6) $\alpha_{sh} = \frac{\kappa_{sh}}{\sqrt{\sum \kappa_i^2}} = \frac{-\gamma_R b \mu_T v_{sh} V_{sh}}{\sqrt{\sum \kappa_i^2}} = \frac{-v_{sh} V_{sh}}{N}$ is calculated and compared to α'_{sh}
- (7) When $\alpha'_{sh} \approx \alpha_{sh}$, $\alpha_T = \frac{-V_T}{N}$ and $\alpha_r = \frac{\psi_1 V_r}{N}$ are calculated

- (8) Check of $\Sigma \alpha_i^2 = 1$
 (9) Z is calculated by Eq. (A.18).

The value of Z is used below in the calculation of the partial coefficients.

A.4 Partial coefficients

The design values in Eqs. (A.10) through (A.12) can alternatively be expressed with partial coefficients as

$$r_d = \frac{r_c}{\gamma_r} = \frac{\mu_r}{\gamma_r} \exp(-k_r V_r) \quad (\text{A.19})$$

$$s_d = \gamma_s \gamma_R (b \varepsilon_{T,c} + c \varepsilon_{sh,c}) = \gamma_s \gamma_R (b \mu_T (1 + k_T V_T) + c \mu_{sh} (1 + k_{sh} V_{sh})) \quad (\text{A.20})$$

which in the limit state condition, Eq. (3), give

$$\frac{\mu_r}{\gamma_r} \exp(-k_r V_r) - \gamma_s \gamma_R (b \mu_T (1 + k_T V_T) + c \mu_{sh} (1 + k_{sh} V_{sh})) \geq 0$$

With $Z = \mu_r / b \gamma_R \mu_T$, $\psi_{sh} = c \mu_{sh} / b \mu_T$ and $\psi_2 = (1 + k_T V_T) + \psi_{sh} (1 + k_{sh} V_{sh})$ it can be re-written as

$$\gamma_s \gamma_r \leq \frac{Z}{\psi_2} \exp(-k_r V_r) = \frac{Z}{\psi_2} \frac{r_c}{\mu_r} \quad (\text{A.21})$$

giving the partial coefficients $\gamma_r \gamma_s$. Z is calculated according to Section A.3 and r_c / μ_r is calculated from Eq. (A.4) with $x_{i,c} / \mu_i = \exp(-\alpha_i \beta V_i) = \exp(-k_i V_i)$. k_i depends on actual fractile value, which for normally distributed functions can be found in any table for the normal distribution, see Table 10 below.

Table 10 - Coefficient k as function of fractile for normal distribution.

Fractile	0.05	0.10	0.15	0.20	0.25	0.30	0.35	0.40	0.45
k	1.65	1.28	1.04	0.84	0.67	0.52	0.39	0.25	0.13

Steel Fibre Reinforced Concrete toppings exposed to temperature deformations – Part I: Experimental study



Jonas Carlswärd, Tech. Lic.
Betongindustri AB, Luleå Technical University
100 74, Stockholm, Sweden
E-mail: jonas.carlsward@betongindustri.se

ABSTRACT

The paper deals with a test method for studying the formation of cracks in restrained concrete overlays. It constitutes the first paper in a series of two, where the second paper deals with a two-dimensional Finite Element Model, developed to simulate the response of the toppings, *Carlswärd* [1]. The experimental set-up consisted of 15 cm thick toppings placed on the surface of a bottom slab constituting a stiff foundation. By exposing the overlays to temperature gradients, tensile stresses, gradually leading to the formation of cracks, developed in the concrete. A total of eight plain and eight fibre reinforced concrete toppings, divided into two series, have been tested. Within the frames of the test programme, it was shown that steel fibres contributed to the limitation of crack widths. Based on the results it was concluded that the test method as such is functional for the purpose, i.e. to study cracking in restrained toppings. Nevertheless, some modifications are suggested in order to further improve the accuracy of the method.

Keywords: Temperature load, Restraint, Cracks, Steel fibres, Bond, Test method.

1. INTRODUCTION

An area of application where steel fibres are frequently used today is as crack distribution reinforcement in thin ground supported concrete structures such as slabs cast on grade, repairs and overlays on parking decks and bridges. A major concern for such structures is related to stresses arising due to restrained deformation that typically develop in a concrete section as a result of drying shrinkage or temperature changes.

Nevertheless, there is, to the author's knowledge, no generally accepted methodology available that allows for predictions of crack spacing and widths based on the type and amount of steel fibres employed. In order to find such methods of design it is necessary to learn more about the behaviour of concrete structures subjected to restrained deformation. A number of test methods have been proposed in literature for this purpose. For instance, the ring test, where concrete is allowed to shrink around an inner stiff steel ring, have been employed in e.g. *Malmberg and*

Skarendahl [2], *Grzybowski and Shah* [3,4], *Shah et al* [5] and *Groth* [6] while specimens with uni-axial configuration have been studied by e.g. *Banthia et al* [7], *Weiss et al* [8], *Kovler* [9] and *Westin et al* [10]. By using such methods it has been shown that steel fibres effectively contribute to the control of cracking caused by restrained deformation. However, as most of the proposed test methods are somewhat idealised as referred to the restraint conditions it is not certain that the results obtained in the various studies are realistic. Accordingly, as was also stated in *Banthia et al* [11], there is a need for developing methods where the restraint is similar to the one in reality. Thus, to develop such a method has been the main objective of this study.

Most often, imposed deformations in concrete overlays are connected to the process of drying shrinkage. However, in the method proposed here it was decided to apply a temperature difference as a load rather than a humidity gradient. The main reason for this choice was that the use of temperature loads enables a test to be carried out within a much shorter period of time.

2. TEST PROGRAM

The principle aim of the present study was to develop a test method that would enable realistic simulations of concrete toppings exposed to restraint stresses. Also, to use the method for evaluating the effect of steel fibres on the fracture response of the specimens was another important ambition. In order to fulfil these objectives a test methodology, as described in the following sections, was developed at Testlab, the testing laboratory of the Technical University of Luleå. A total of eight tests, divided into two series, series I and II, were then conducted to verify the influence of steel fibres on the crack formation.

2.1 Specimen Details

The test program was conducted during a relatively long period of time in which the methodology was successively developed. Thus, the adopted technique was not identical from test to test. A major change that was made in order to enable a more controlled procedure was to decrease the size of the bottom slabs from 4200x1200x200 mm to 2400x1400x200 mm, see *Feil! Ukjent bryterargument..*. Apart from making it easier to handle this also resulted in a symmetric set-up, which is preferable from a consistency point of view. A total of four tests were performed on each type of slab. In order to separate them, the first mentioned tests are referred to as series I while the last four tests are called series II.

Another important difference between the slabs of the two series was that the surface texture of the upper faces was varied. For the slabs of series I a rather rough texture was achieved by brushing the wet concrete while the slabs of series II were either board levelled or grinded, which in both cases resulted in considerably smoother texture. The smoothest surface was obtained for the grinded slabs. The reason for changing the surface texture of the slabs was to be able to study the effect of different bond situations on the crack development in the toppings.

Details on the experimental configuration of the set-ups developed in each of the series are shown in *Feil! Ukjent bryterargument..*. At every test occasion a bottom slab (1 in the figure), that had been manufactured in advance, was positioned on the laboratory floor. To ensure that the slab would have full contact with the substrate the floor had previously been covered by a

thin layer of cement based levelling compound. Furthermore, two layers of plastic sheet had been placed on top of the levelling compound in order to make sure that the slab would be able to move freely.

In both test series the bottom slabs (1) had been prepared with heating cables close to the upper and lower surfaces. Heating cables were also embedded in the toppings for most of the tests (except for the first two tests, I:1 and I:2). Furthermore, the slabs were prepared with $\varnothing 80$ mm holes with an individual distance of 1 m along each side where $\varnothing 50$ mm restraining ties were fitted (3). This made it possible to fasten the slab rigidly to the thick laboratory floor, to simulate an inflexible sub-grade.

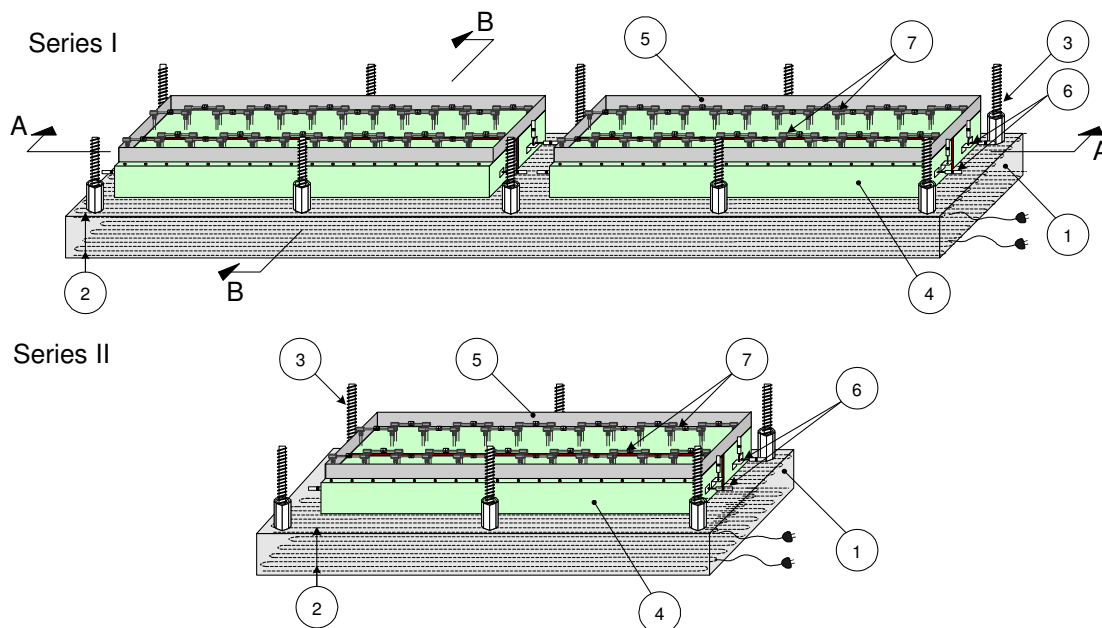


Figure Feil! Ukjent bryterargument. – Principle illustrations of the set-ups developed in the present study. The smaller bottom slabs employed in series II allowed for a somewhat more controlled test procedure.

Concrete toppings (4 in the figure) with depths of 150 mm, widths of 300 mm and lengths of 1800 mm were then placed on top of the substrate slab, which had been previously cleaned and wetted 24 hours in advance in order to enhance the bond properties. At each production occasion two such specimens were cast aside each other, one with plain and one with steel fibre reinforced concrete. In this way a direct comparison was obtained between SFRC and PC for specimens exposed to exactly the same load situation.

After an initial curing period of at least one week the preparation of the specimens was initiated by mounting borders of sheet metal (5) at the upper faces. The reason for this was to prevent the cold water, which was used to create the temperature gradient, from running off the upper surface of the overlays in an uncontrolled fashion. The specimens were also prepared with different gauges for measuring deformations (6 and 7). These are described in more detail in section 2.3. At the time of testing the concrete was in all cases at least a month old.

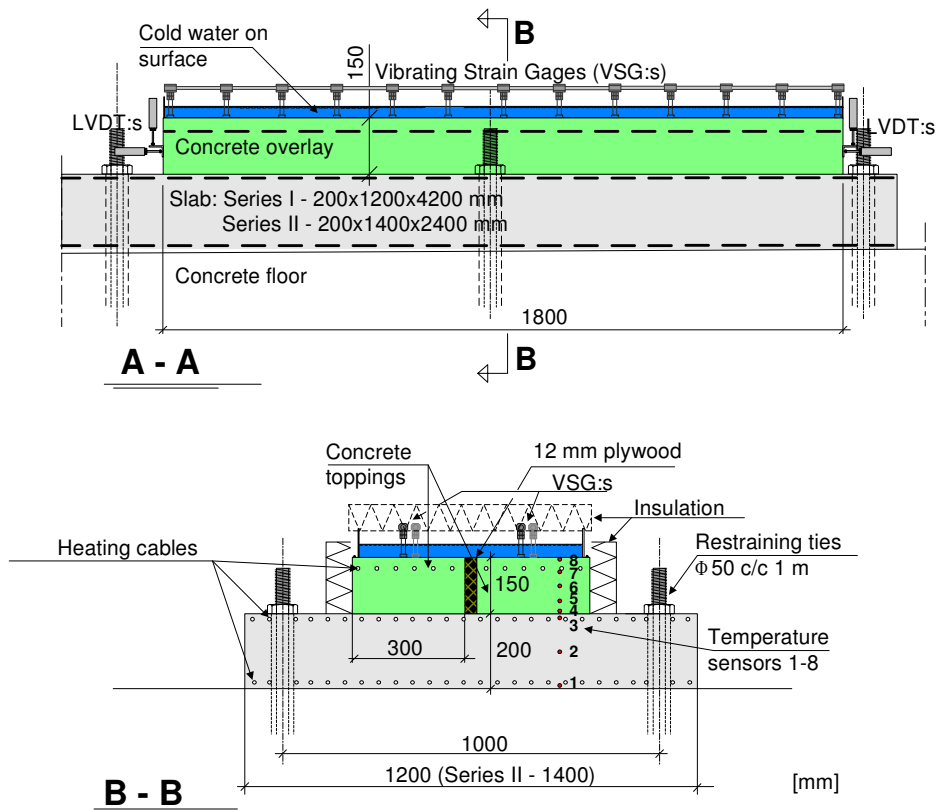


Figure Feil! Ukjent bryterargument. – Sections through the test set-up showing some measures and instrumentation.

2.2 Test Procedure

In order to reach a state of stress in the concrete overlays that would result in cracking, one of the main issues was to generate a substantial temperature difference between the top and bottom faces of the test specimens. At the same time it was necessary to restrain the specimens to avoid free deformation. The testing technique adopted to fulfil these requirements is schematically presented in *Feil! Ukjent bryterargument*.

Each test was initiated by heating up the specimens to a predefined temperature using the embedded heating cables, phase 1. During the heating process the slab was free to move in order to avoid pre-stressing the toppings. Also, in order to ensure a uniform temperature distribution over the entire test set-up, the overlays were covered with a layer of insulation, see section B-B in *Feil! Ukjent bryterargument*. After reaching the temperature level aimed at, T_1 , the bottom slab was fastened to the thick and inflexible floor by applying loads to the restraining ties. In theory this would prevent further displacements of the test set-up, implying that the bottom slab from this point on could be seen as a rigid base.

Phase 2 was then initiated by switching off the power to the cables in the overlays before the top insulation was removed. Cold water was then distributed on the upper surface of the toppings a

few hours later, which resulted in a rather steep temperature decrease, particularly near the upper faces.

The temperature of the slab was maintained at a rather high level throughout the cooling phase by leaving the heating cables on. In this way, temperature gradients of considerable magnitude rapidly developed over the depth of the overlays. As a consequence tensile stresses, which gradually lead to the formation of cracks, were created in the concrete.

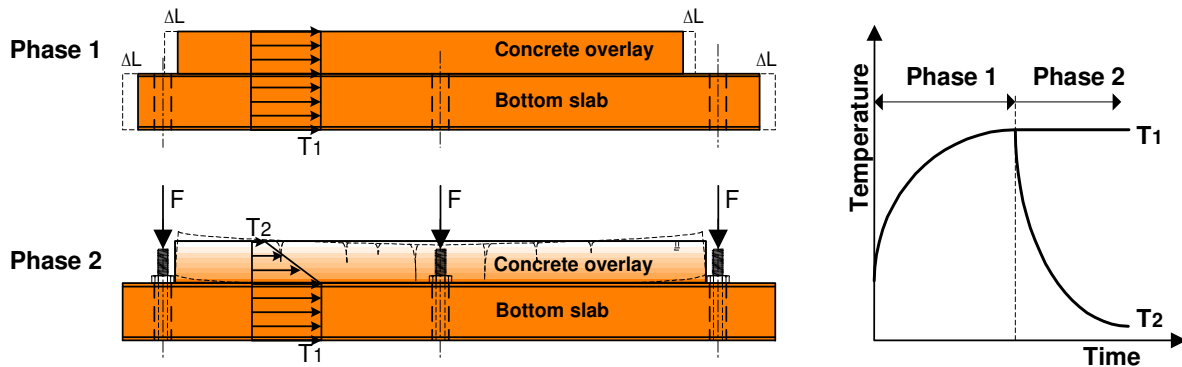


Figure *Feil! Ukjent bryterargument*. – Schematic illustration showing the different phases of the test procedure. (Phase 1 – Heating of overlay and bottom slab, Phase 2 – Cooling of overlay).

2.3 Instrumentation

The instrumentation employed in the tests to provide information about temperature distribution and deformations is shown in *Feil! Ukjent bryterargument*. and *Feil! Ukjent bryterargument*.. Thermocouples were embedded at different levels both in the bottom slab as well as in the overlays, sensors 1 to 3 in the slab and 4 to 8 in the concrete overlays. This made it possible to follow the temperature development throughout the different phases of the testing procedure. Longitudinal deformations were continuously recorded at the upper faces of the toppings in order to study the crack formation. The strain reading device used for this purpose was Vibrating wire Strain Gauges (VSG:s), as shown in *Feil! Ukjent bryterargument*. (a). As is evident from the name the VSG:s use the vibrating wire principle when measuring strains. The implication of this is further developed in *Geokon* [12].

From the photo in (a) it can be seen that the VSG:s, with a measuring length of 150 mm, were placed between two bolts that had been previously glued to the concrete surface. The reason for not embedding part of the bolts in the concrete was that it would result in crack directors that could disturb the strain readings.

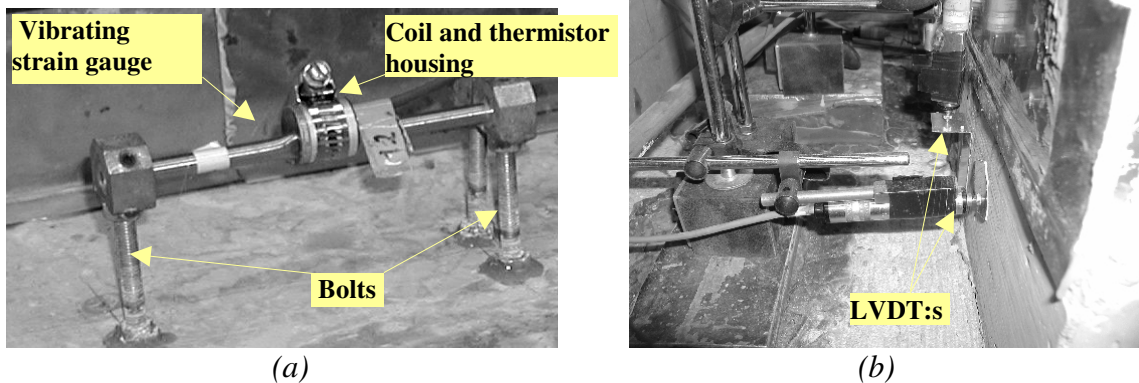


Figure *Feil! Ukjent bryterargument*. – (a) Strain measurement device (VSG:s) used to record longitudinal deformations at the upper face of the toppings. (b) LVDT:s placed at the ends of the toppings to record horizontal and vertical displacements.

Horizontal and vertical displacements of the ends of the overlays were measured by means of Linear Voltage Differential Transducers (LVDT:s) as shown in *Feil! Ukjent bryterargument*. (b). For the specimens of series I the displacements were measured relative to the floor at the left end while the displacements at the right end were measured relative to the bottom slab. This way of measuring made it possible to control that the bottom slab would not move during the cooling process. On the other hand, for the tests of series II the edge displacements of the toppings were recorded with the floor as a reference at both ends. This implies that no information as regards the difference in deformation between toppings and slabs was obtained in this case. Nevertheless, it is evident from the results presented in section 3.3 that some interesting information on this matter could be distinguished. The reason why more LVDT:s were not used to control the displacements of the slab relative the floor was mainly due to the lack of space in the end zones.

2.4 Material Details

As the primary objective was to develop a test procedure that would give consistent results no predefined test program was initially followed in which a certain mix design was used. For this reason the concrete composition changed a few times, at least for the tests of series I, see *Feil! Ukjent bryterargument*. For series II, on the other hand, the mix design was kept the same for all tests. As can be seen in the table a total of eight tests were carried out, four in each series. At every production occasion one mix was produced with steel fibres and one without. The type of fibres was in all cases the Dramix[®] RC-65/35-BN, which is an end-hooked, round fibre with a length of 35 mm and a diameter of approximately 0,54 mm. The amount of steel fibres was either 20 or 30 kg/m³ for the specimens of the first series and 30 or 60 kg/m³ for series II.

Table Feil! Ukjent bryterargument. – Mix proportions of the concrete used in series I and II.

Test Nr	Cement (kg/m ³)	Filler (kg/m ³)	Sand 0-8 (kg/m ³)	Gravel 8-16 (kg/m ³)	Sp (kg/m ³)	Water (kg/m ³)	Steel Fibres (kg/m ³)	w/c - ratio
Series I								
PC I:1	350	150	1010	673	3,5	178	0	0,51
FRC I:1	350	150	1010	673	3,5	178	30	0,51
PC I:2	350	150	1172	631	2,8	192	0	0,55
FRC I:2	350	150	1172	631	2,8	192	20	0,55
PC I:3	350	150	1143	515	3,5	190	0	0,54
FRC I:3	350	150	1143	515	3,5	190	30	0,54
PC I:4	350	0	1007	824	3,7	180	0	0,55
FRC I:4	350	0	1007	824	3,7	180	30	0,55
Series II								
PC II:1	350	0	1007	824	3,7	180	0	0,55
FRC II:1	350	0	1007	824	3,7	180	30	0,55
PCII :2	350	0	1007	824	3,7	180	0	0,55
FRC II:2	350	0	1007	824	3,7	180	30	0,55
PC II:3	350	0	1007	824	3,7	180	0	0,55
FRC II:3	350	0	1007	824	3,7	180	60	0,55
PC II:4	350	0	1007	824	3,7	180	0	0,55
FRC II:4	350	0	1007	824	3,7	180	60	0,55

The type of concrete composed for the first three tests of series I, tests I:1-3, was a Self Compacting one (SCC) while the remaining mixes were of a conventional type. As is evident from *Feil! Ukjent bryterargument.* limestone filler, of the type Köping 500, was used in the SCC mixes in order to enhance the stability. Furthermore, to achieve good fluidity an effective superplasticiser, a so called co-polymeric admixture of the type Glenium 51, was used for these mixes while a melamine-based one, type M 92, was used for the remaining tests. The cement was of the type Std PK Slite, which is classified as a CEM I 42,5 R type of cement.

3. TEST RESULTS

3.1 Material properties

Material properties obtained from compressive, tensile and four point flexural tests are summarised in *Feil! Ukjent bryterargument.* Values in brackets are the standard deviations from two specimens for the compression test, four (in some cases three) specimens for the uniaxial tensile test and two specimens for the flexural beam test. The compressive strength was evaluated on 150 mm cubes while the tensile strength was obtained from uniaxial tests on Ø94 mm cylinders. In order to enable measurements of the crack width during the process of a tension test the specimens were prepared with a notch giving a waist diameter of about 74 mm. This also made it possible to conduct the tests under displacement control, which gave information regarding the post cracking performance of the concrete. The measuring length was about 30 mm. Information on the softening response was also provided by the flexural beam tests conducted in accordance with the ASTM C1018 procedure, as described in detail in e.g. *Concrete Report No 4* [13].

Table Feil! Ukjent bryterargument. – Material properties for the concrete produced for the toppings and information regarding the interface texture.

Test Nr	Comp. strength		Tensile strength			Flexural strength			Interface condition	
	f_{cc} MPa	Age d	f_{ct} MPa	G_f Nm/m ²	Age d	f_{flu} MPa	$R_{10,30}$ %	$R_{10,50}$ %		Age d
Series I										
PC I:1	43,7 (2,4)	47	3,34 (0,14)	133 (7)	53	5,63 (0,43)	0	0	80	Brushed
FRC I:1	53,0 (3,8)	47	3,35 (0,06)	6265 (1891)	53	6,32 (0,32)	47 (6)	46 (6)	80	Brushed
PC I:2	42,9 (1,1)	98	3,39 (0,50)	124 (14)	301	4,81 (0,11)	0	0	272	Brushed
FRC I:2	36,4 (5,8)	98	3,20 (0,34)	916 (242)	301	4,83 (0,04)	21 (4)	18 (4)	272	Brushed
PC I:3	44,5 (0,4)	28	3,44 (0,07)	142 (82)	228	5,08 (0,31)	0	0	200	Brushed
FRC I:3	38,4 (2,2)	28	3,07 (0,27)	1260 (580)	228	5,66 (0,08)	40 (11)	37 (10)	200	Brushed
PC I:4	54,9 (2,3)	41	3,69 (0,27)	143 (15)	196	5,22 (0,03)	0	0	166	Brushed
FRC I:4	52,2 (1,8)	41	3,26 (0,44)	1289 (708)	196	5,33 (0,52)	39 (13)	38 (12)	166	Brushed
Series II										
PC II:1	54,1 (2,1)	46	3,33 (0,15)	163 (31)	148	5,24 (0,26)	0	0	116	Grinded
FRC II:1	53,0 (2,9)	46	3,39 (0,08)	2757 (1080)	179	5,52 (0,50)	32 (12)	31 (13)	116	Grinded
PCII :2	55,5 (0,9)	33	3,40 (0,40)	169 (29)	134	5,31 (0,46)	0	0	103	Boarded
FRC II:2	54,2 (0,9)	33	3,43 (0,19)	2109 (1150)	165	4,85 (0,01)	45 (16)	43 (13)	103	Boarded
PC II:3	50,6 (2,2)	29	2,84 (0,43)	146 (34)	93	4,47 (0,16)	0	0	62	Boarded
FRC II:3	50,6 (5,3)	29	3,10 (0,25)	2739 (455)	126	5,12 (0,47)	61 (2)	60 (4)	62	Boarded
PC II:4	55,9 (0,5)	35	3,52 (0,15)	200 (21)	81	4,53 (0,11)	0	0	48	Grinded
FRC II:4	58,3 (2,7)	35	2,93 (0,19)	1367 (85)	117	5,50 (0,05)	58 (17)	57 (16)	48	Grinded

In the table information is also provided on the interface conditions between slabs and toppings. The roughest texture was achieved for the brushed slabs, series I, while the grinding resulted in the smoothest texture, tests II:1 and II:4. Thus, even if the roughness is certainly not the only parameter with influence on the interface properties, it is reasonable to suspect that the best bond conditions were achieved for the tests of series I while the worst conditions were reached for tests II:1 and II:4. Tests will be conducted to verify the correlation between roughness and bond strength for the toppings of series II.

Results and information regarding the geometry and loading configuration for the four point flexural beam tests are presented in *Feil! Ukjent bryterargument.* (a) and (b) for series I and II respectively. In general it can be seen that while the resistance of the plain concrete specimens dropped rather steeply after reaching the maximum load the fibre reinforced ones proved to have considerable residual strength.

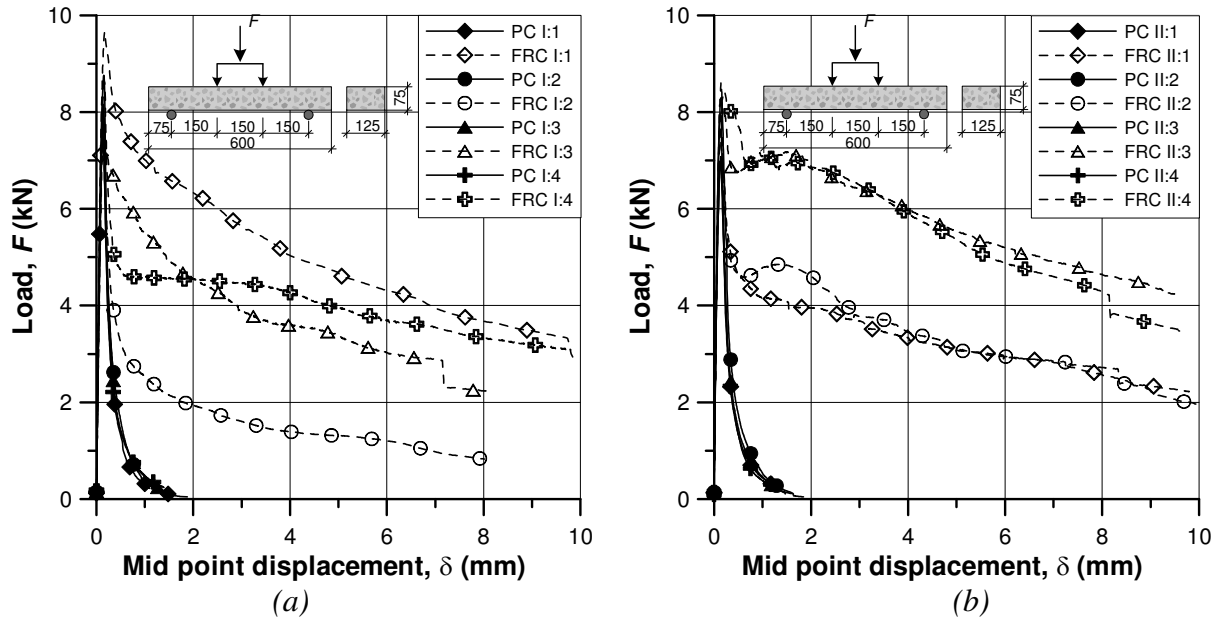


Figure Feil! Ukjent bryterargument. – The diagrams show results from four point flexural tests that were conducted in accordance with the ASTM C1018 standard. Series I in (a) and series II in (b).

When studying the results of series I in *Feil! Ukjent bryterargument*. (a) it can be seen that the poorest response of the fibre reinforced beams was obtained for test FRC I:2. This was expected since the amount of fibres used in this case was only 20 kg/m^3 . Moreover, it is evident that the best residual performance was recorded for FRC I:1. As the fibre amount in this case was the same as for the last two tests of series I, 30 kg/m^3 , this implies that the combination of fibres and concrete composition was possibly more suitable in this case.

For the specimens of series II the concrete mix was kept the same. This is most certainly also the reason as to why the general responses obtained from the flexural tests are quite consistent. When comparing the FRC composed for the first two tests (II:1 and 2) with the last ones in series II (II:3 and 4) it can further be concluded that the residual response was substantially improved as the fibre content increased from 30 to 60 kg/m^3 .

Results from the uniaxial tensile tests are presented in *Feil! Ukjent bryterargument*. (a) and (b). Evident from these graphs showing the strength as a function of the crack opening displacement, is that the effect of steel fibres was not as obvious as for the flexural tests discussed previously. In fact, the only mix where the fibre addition showed to have a considerable contribution was for test I:1. In all other cases only small differences in post-cracking response were registered between plain and fibre reinforced concrete. Considering that the uniaxial tensile response is intimately connected to the flexural strength the effect should have been more distinct.

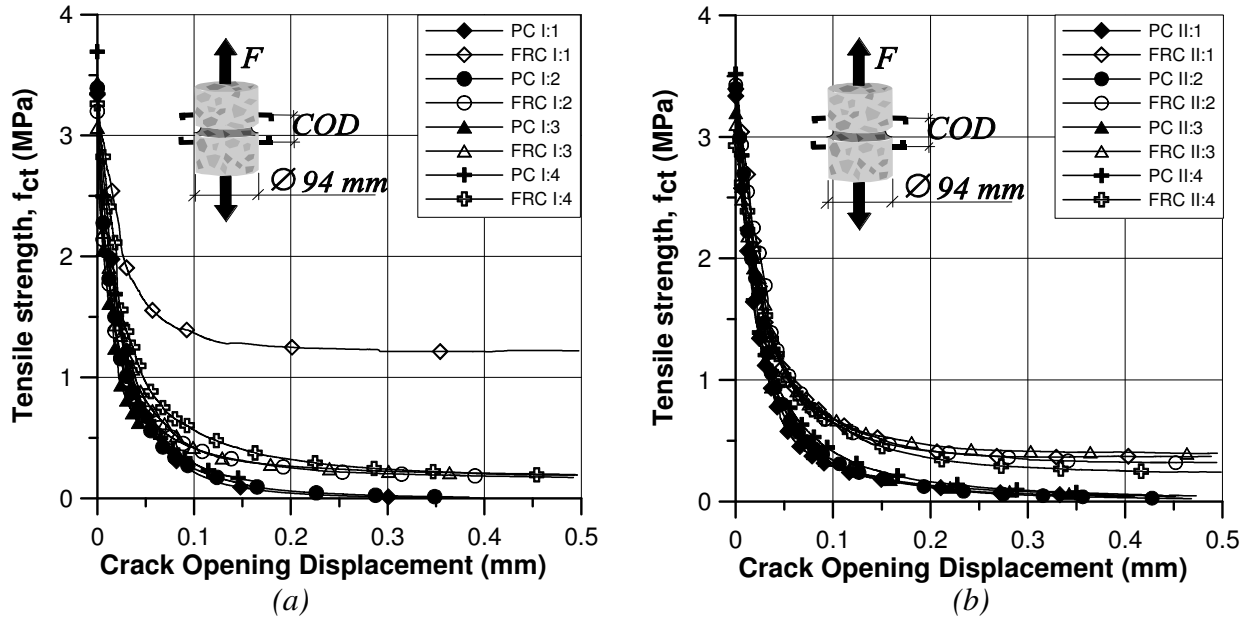


Figure Feil! Ukjent bryterargument. – Post cracking response of the concrete obtained from uniaxial tensile tests. The results from the concrete produced in series I are shown in (a) and series II in (b).

The reason why this was not the case here is most certainly related to the way that the specimens were manufactured. Cores were taken out from 150 mm cubes using the same procedure in each case, i.e. drilled from the face that had been facing upwards during casting. The reason why the performance of FRC I:1 was not visibly effected by this procedure while it had such a great influence on all the other FRC specimens was that the cubes produced in this case were not vibrated. For the other specimens vibration was carried out, which possibly aligned the fibres in a predominantly horizontal direction. This would clearly have a negative effect on the post-cracking response of the fibre reinforced concrete, thus mitigating the fibre effect. The assumption could have been verified by checking the fibre orientation for each individual specimen. Unfortunately, this was not done here but the general experience from ocular inspections was that the number of bridging fibres in the fracture zones was rather low.

3.2 Temperature development

An example of the temperature development during the different phases of the testing procedure is shown in *Feil! Ukjent bryterargument.* for the last test of series II, test II:4. The complete test cycle is presented in (a) while the development of temperatures during the cooling phase alone is shown in (b). In order to make the latter graph more legible it was decided to zero the temperatures at the initiation of phase 2. Thus, time zero in graph (b) corresponds to the initiation of cooling.

When studying the temperatures during the heating phase, *Feil! Ukjent bryterargument.* (a), it can be seen that there was a rather extensive temperature scatter, about 15 °C at the end of this phase. This was primarily due to a cooling effect from the concrete floor, which held back the temperature development in the slab. A difference in temperature between the various parts of the set-up is clearly not desirable at this stage as it means that the toppings seek to expand different than the slab. This may result in an undesired stress build-up. In this case it is likely

that compressive stresses developed in the toppings due to higher temperature in the toppings as compared to the slab. However, the fact that the slab was free to move during the heating phase implies that this temperature difference may also have caused the set-up to bend. This means that a tensile stress field may have developed in the toppings when the slab was fastened to the floor. In either case it is clear that the temperature scatter influences the possibilities of theoretically evaluating the stress levels in the toppings caused by the following temperature decrease.

Furthermore, it is likely that the rather high temperature produced during the heating phase, about 80 °C in the test shown in *Feil! Ukjent bryterargument.*, influences the response of the concrete. In previous studies it has been shown that an increased temperature decrease the strength and the elastic modulus of the concrete and increase the creep deformations [14]. Other results reported in the same reference indicate that the coefficient of thermal expansion increases with increasing temperatures. However, no tests have been conducted in this study to examine the properties of the concrete at different temperatures. This is yet another factor that restricts a potential theoretical evaluation of the tests.

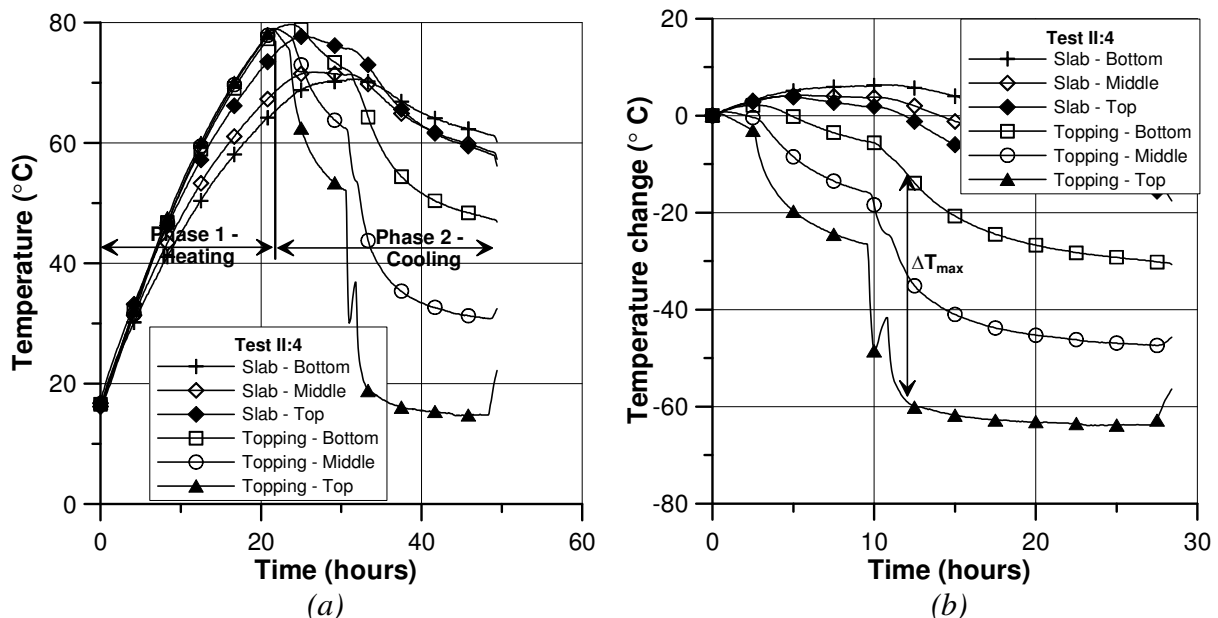


Figure *Feil! Ukjent bryterargument.* – (a) Temperature development during the complete testing process, heating and cooling, for test II:4. (b) Temperature development during the cooling phase alone for test II:4. The positions of the thermocouples for which results are shown can be found in section B-B in *Feil! Ukjent bryterargument.*.

The temperature distribution over the set-up during the second phase, cooling, can be seen in *Feil! Ukjent bryterargument.* (b). At time zero in the graph the power to the heating cables of the toppings was turned off while the heating of the slab was continued. This resulted in a slight decrease of the temperature near the upper face of the toppings. After approximately two hours the top insulation was removed, which is represented by the increased cooling rate at this point. Cold water was then distributed on the toppings after another eight hours. This led to a very steep temperature fall near the top. Following this procedure a temperature gradient between top and bottom of the overlays, ΔT , of up to a maximum of 48 °C was reached for test II:4. Similar values were also reached for tests II:1 and II:2 while a slightly greater maximum gradient, 56 °C,

was recorded for test II:3. The corresponding values for the tests of series I were 35, 38, 43 and 45 °C for tests I:1, I:2, I:3 and I:4 respectively.

3.3 Edge displacements

A typical feature of continuously bonded toppings is the displacements appearing near free ends, generally referred to as edge lifting or curling. This phenomenon occurs for the reason that bond forces acting along the interface equilibrate the resultant force of the imposed strain field. As a consequence, a tensile stress field is established that tends to lift the topping vertically at free ends. This typically results in the development of joint cracks that extend progressively along the interface surface between topping and substrate material as soon as the bond strength is exceeded. Thus, measuring the development of end displacements of the toppings should give an indication of the bond quality. Here, information on this subject was provided by means of deformation gauges mounted on the end faces of the toppings, see *Feil! Ukjent bryterargument.*, *Feil! Ukjent bryterargument.* and *Feil! Ukjent bryterargument.* (b).

Recorded end displacements for test II:4 are presented in *Feil! Ukjent bryterargument.* (a) and (b). The reason for the choice of test is simply to enable comparisons with the temperature development shown in *Feil! Ukjent bryterargument.* (a) and (b). Similar to the presentations of temperatures, the first graph shows the development of displacements throughout the complete duration of a test while the deformations developed during the cooling phase alone are shown in the other graph.

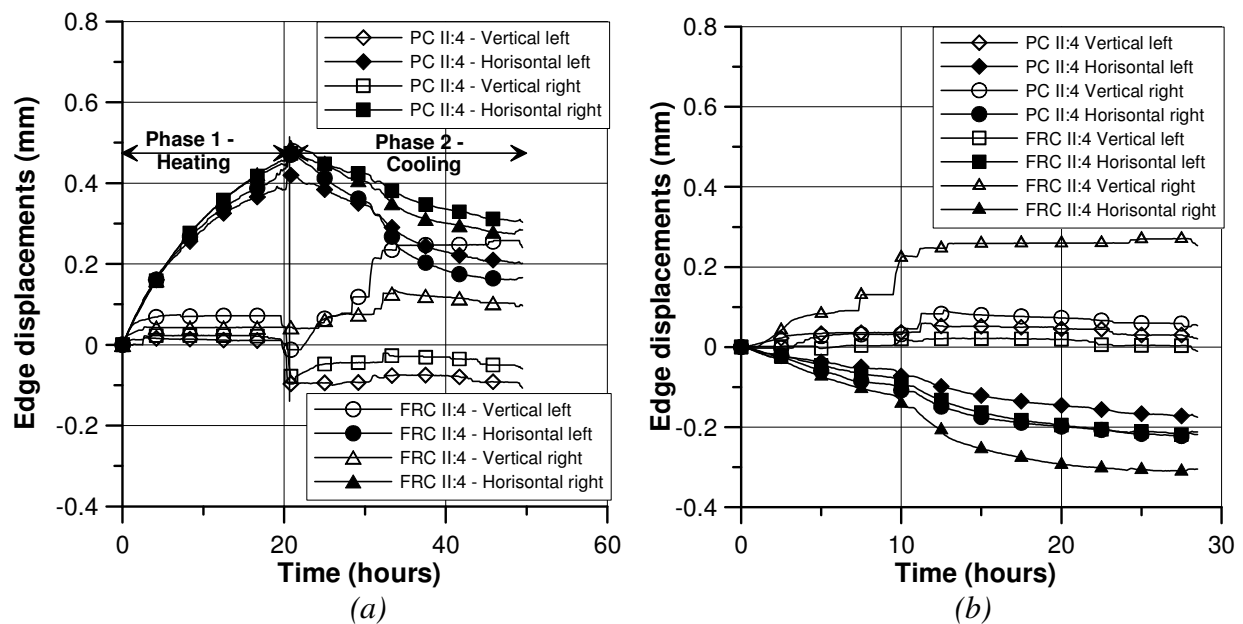


Figure *Feil! Ukjent bryterargument.* – Vertical and horizontal displacements recorded at the ends of the toppings by means of LVDT:s for test II:4. The complete test cycle, i.e. heating and cooling, in (a) and the cooling phase alone in (b).

From the first graph, *Feil! Ukjent bryterargument.* (a), it can be seen that major horizontal displacements were recorded during the heating phase while the vertical movements were rather insignificant. This implies that the set-up mainly translated on the laboratory floor. The small vertical displacements possibly occurred due to thermal expansion of the concrete.

Based on the temperatures shown in *Feil! Ukjent bryterargument.* (a) a maximum horizontal displacement of about $50 \cdot 1 \cdot 10^{-5} \cdot 1200 = 0,6$ mm can be estimated at each end, for $\Delta T = 50$ °C, $\alpha = 1 \cdot 10^{-5}$ and $L/2 = 1200$ mm. However, the measured displacements at this stage were only between 0,4 and 0,5 mm. Considering that the slab was not fastened to the floor at this stage and that plastic sheet was covering the laboratory floor underneath the slab to reduce the friction, this implies that the recorded temperatures may not have been relevant for the complete set-up.

After fastening the slabs to the floor the measured deformations should represent the actual lifting and slipping of the toppings in relation to the slab. However, as the displacements in most cases, except for the right ends of the specimens of series I, were measured with the floor as reference this was not entirely true. Nevertheless, some conclusions may be drawn regarding the development of end displacements of the toppings. For instance, substantial vertical deformations were registered at the right end of the fibre reinforced specimen of test II:4, see *Feil! Ukjent bryterargument.* (b). Unquestionably, this implies that a major joint crack has developed along the interface at this position. Also interesting to notice is that the corresponding horizontal displacement, i.e. at the right end of the FRC topping, was slightly greater than the other recorded translations. This implies that end lifting is followed by horizontal translation.

Information regarding the maximum displacements recorded during the cooling phase of each test can be found in *Feil! Ukjent bryterargument.*, where it is observed that the greatest displacements were recorded for the specimens of test I:3, PC I:3 and FRC I:3. The reason for this was that complete de-bonding occurred already during (or even before) the heating phase, thus implying that the displacements measured in this case constitute free deformation. Evidently, this resulted in maximum displacements of about 0,7 and 0,3 mm in vertical and horizontal direction respectively. The reason for the de-bonding is unclear. A laboratorial mistake is though suspected.

Table Feil! Ukjent bryterargument. – Max displacements at the ends recorded with the LVDT:s during the cooling phase.

Series I	Vertical mm		Horizontal mm		Series II	Vertical mm		Horizontal mm	
	Left	Right	Left	Right		Left	Right	Left	Right
PC I:1	0,10	0,03	0,03	0,08	PC II:1	0,30	0,05	0,32	0,36
FRC I:1	0,14	0,12	0,03	0,08	FRC II:1	0,36	0,14	0,33	0,39
PC I:2	0,06	0,02	0,19	0,09	PC II:2	0,02	0,02	0,26	0,27
FRC I:2	0,08	0,01	0,09	0,09	FRC II:2	0,10	0,08	0,29	0,30
PC I:3	0,65	0,68	0,27	0,24	PC II:3	0,14	0,12	0,14	0,15
FRC I:3	0,64	0,73	0,26	0,22	FRC II:3	0,13	0,14	0,19	0,18
PC I:4	0,60	0,06	0,36	0,10	PC II:4	0,06	0,02	0,18	0,22
FRC I:4	0,59	0,10	0,33	0,10	FRC II:4	0,09	0,27	0,22	0,31

Almost as great displacements, as for test I:3, were also recorded at the left end of PC I:4 and FRC I:4. This implies that quite extensive de-bonding occurred in these cases as well. For the tests of series II the greatest joint cracks seem to have developed at the left end of the specimens of the first test, PC II:1 and FRC II:1, and at the right end of the fibre reinforced specimen of the last test, FRC II:4.

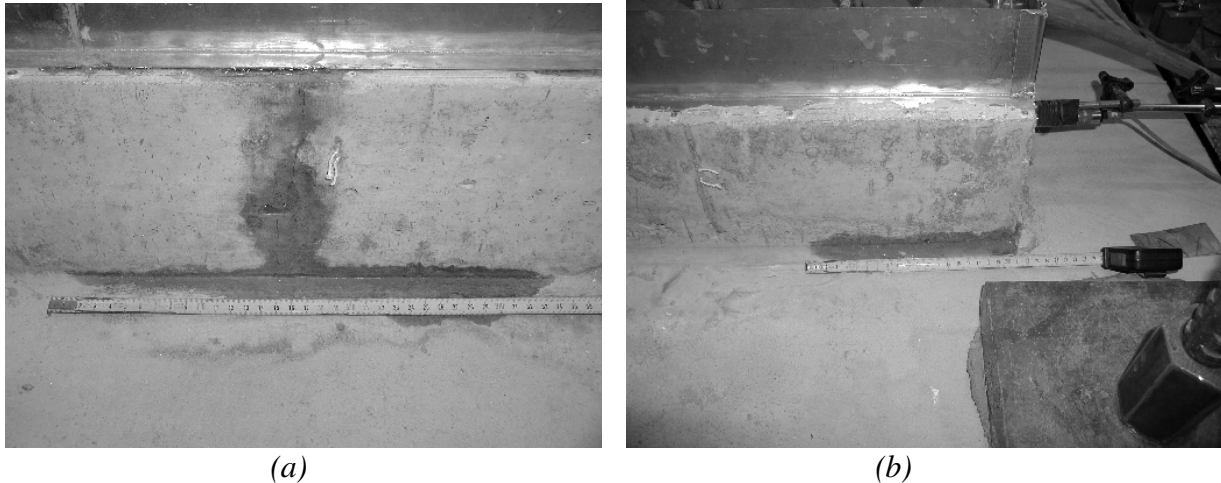


Figure 3.4. – Photos illustrating displacements of topping PC II:4 that resulted in de-bonding along the interface in the vicinity of a crack in (a) and at the end zone in (b).

The displacements near free ends were also visually observed for some of the specimens within the present test program, see *Feil! Ukjent bryterargument.*. In the photos, the lifting is represented by the moist areas, which appeared for the reason that water found its way from the upper face and through the topping. It is further clear that this phenomenon was not exclusively restricted to the ends of the specimens but was also found in the vicinity of through cracks. This is not surprising considering that two new free ends are generated for each extensive crack that is established in the topping.

3.4 Longitudinal strains and crack development

Longitudinal strains recorded with VSG:s at the upper faces of PC II:4 and FRC II:4 are shown in *Feil! Ukjent bryterargument.* (a) and (b) respectively during the cooling phase alone. Thus, time zero in the graphs corresponds to the initiation of cooling. At this point the strains have also been zeroed in order to make the graphs more legible. The presented strain development gives information both concerning the time at which cracks start to propagate as well as about the crack widths.

When comparing the response of PC II:4 and FRC II:4 it can be concluded that there was a substantial effect of fibres. This is most certainly due to the rather high fibre volume fraction used in this case, 60 kg/m^3 . It can further be established that the fibres bridging the cracks of FRC II:4 were able to withstand the rather abrupt load following from the distribution of cold water on the upper face at a time of approximately 10 hours. While the widths of the two cracks in the plain concrete specimen, at locations 450-600 and 1200-1350 mm, increased steeply at this point the cracks in the fibre reinforced one only grew marginally. At this stage, however, it is evident that a new crack was initiated between 450 and 600 mm from the left end of the fibre reinforced topping. Possibly, this indicates a redistribution of stresses due to the contributing effect of fibres bridging and transferring forces over cracks.

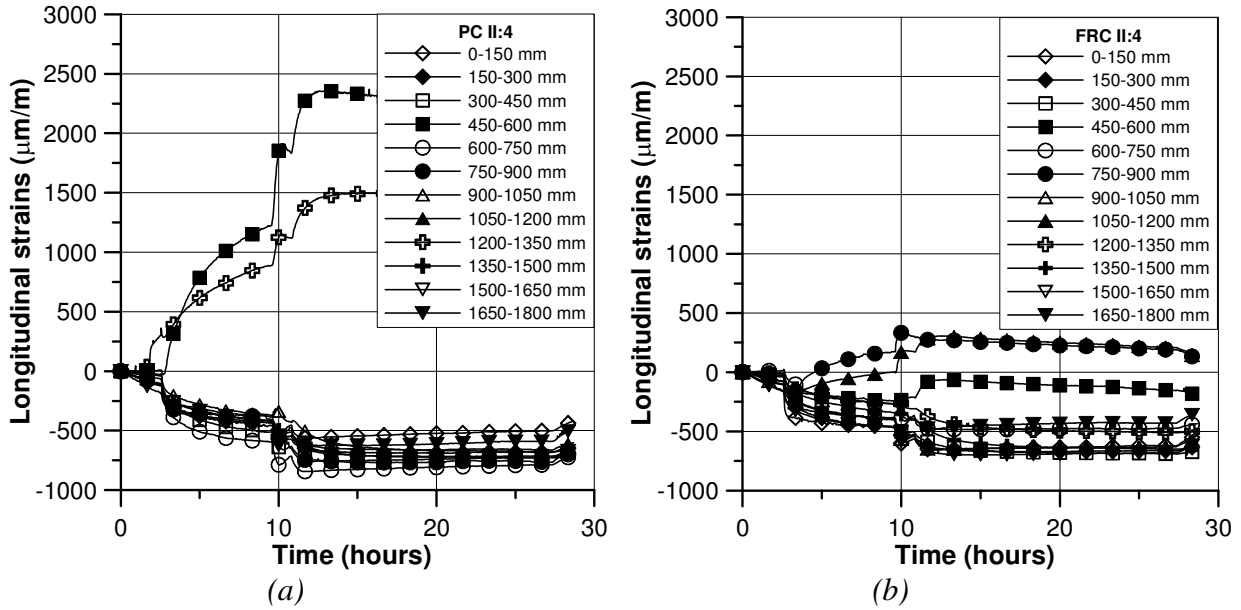


Figure 15. – Examples of longitudinal strain developments measured with the VSG:s on the upper face of the overlays during the cooling phase for PC II:4 and FRC II:4 in (a) and (b).

Summaries of the strain distributions recorded for the toppings in both series of tests are presented in *Feil! Ukjent bryterargument.*, series I in (a) and (b) and series II in (c) and (d). The distributions correspond to the time during the cooling phases when maximum crack widths were registered. Clearly, the general tendency is that the extreme values of the strains obtained for the PC specimens were greater as compared to the corresponding values of the FRC specimens. This indicates that the cracks appearing in the plain concrete toppings were wider than for the corresponding fibre reinforced ones.

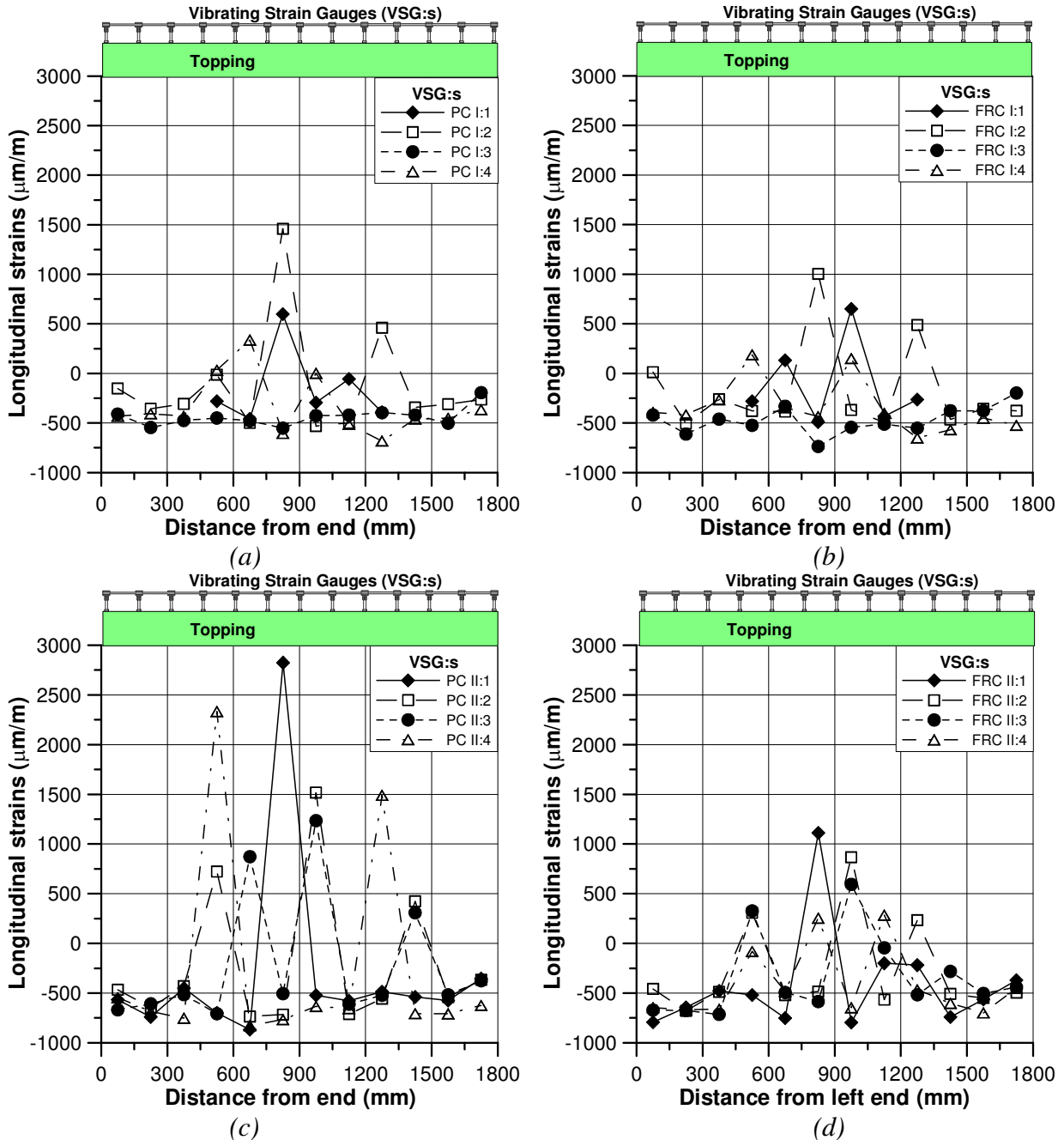


Figure Feil! Ukjent bryterargument. – Maximum longitudinal strain distributions registered during the cooling phase. Summaries of results obtained for the Plain and Fibre Reinforced Concrete specimens of series I are shown in (a) and (b) while the corresponding results for the PC and FRC specimens of series II are shown in (c) and (d).

Moreover, it is clear that the effect of steel fibres on the crack distribution was more apparent for the tests of series II as compared to the ones of series I. A possible reason for this is that the bond quality of the interface layer between toppings and slabs may have been somewhat better for the tests of series I, except for test I:3. Especially considering that the upper faces of the bottom slabs used in series I had a brushed texture while the corresponding surfaces of the slabs in series II had either grinded or board levelled textures, see *Feil! Ukjent bryterargument.*. A consequence of better bond characteristics would be that crack distribution is accomplished even without reinforcement which seems to have been the case for the tests of series I where only

minor differences were observed between PC and FRC. This reasoning implies that the effect of steel fibres would increase as the quality of the bond diminishes.

The above conclusion is further verified by the results presented in *Feil! Ukjent bryterargument. (a)*. Here, the maximum crack width, or rather the maximum deformation measured over a gauge length of 150 mm, for each of the toppings in the two series of tests is plotted as a function of the steel fibre amount. It is evident that the crack width reduction was considerably greater for some of the tests of series II as compared to series I. Particularly interesting is that the widest cracks, and also the most substantial fibre effects, were recorded for the tests where the slabs with the smoothest surface texture had been used, tests II:1 and II:4.

It is also important to mention that the measuring length of the VSG:s may have had an influence on the registered deformations. Considering that the length was 150 mm it is clear that not only the deformations over the actual crack zone were registered but also the strains in the surrounding un-cracked concrete. This may have influenced the results as the cracks forming in PC, differently from the ones forming in FRC, rapidly extended to the bottom of the section in most cases. Successively this resulted in a de-bonded zone in the vicinity of each crack, as was also indicated in *Feil! Ukjent bryterargument. (a)*. This implies that, for the PC specimens, the imposed strains resulting from the temperature reduction were released in the concrete near the cracks. Thus, the recorded strains should represent the real crack widths relatively well. For most of the FRC toppings, on the other hand, the measured “crack widths” may have been smaller than the real widths. The reason for this is that bridging fibres restricted the crack extension. This implies that the negative strain in the un-cracked concrete was not released, as was the case for the plain concrete toppings.

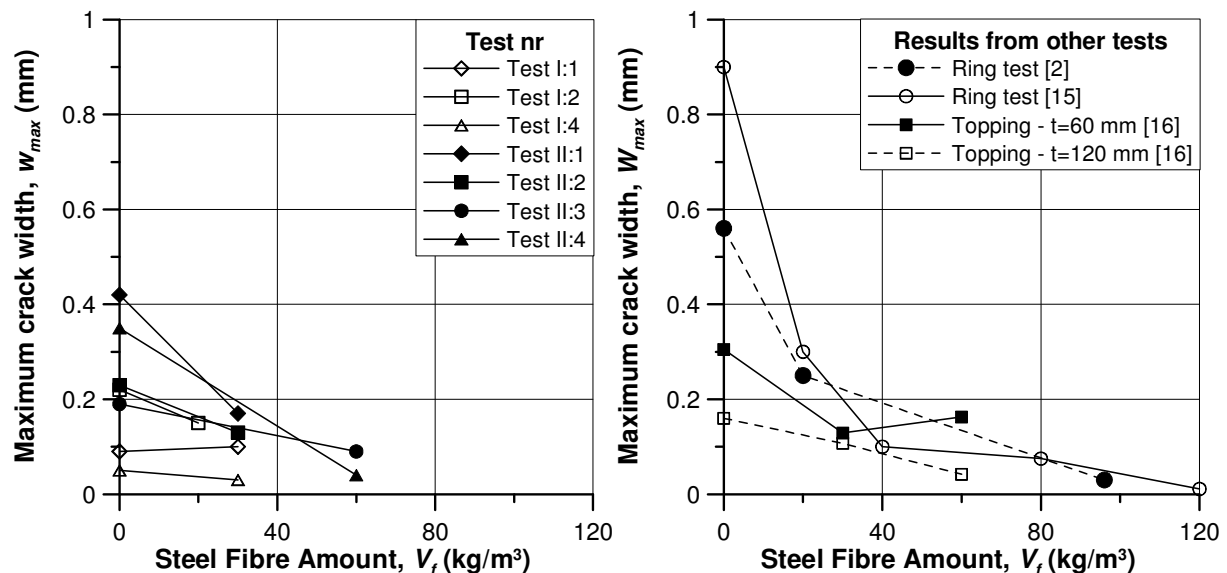


Figure *Feil! Ukjent bryterargument. (a)* Maximum crack widths as a function of the steel fibre amount for the tests in the present study. (b) Maximum crack widths reported from tests on ring shaped specimens [2,14] and toppings [15].

A few examples of results from studies on restrained drying shrinkage are shown in *Feil! Ukjent bryterargument. (b)* for comparison reasons. In the ring test the restraint is provided by an inner stiff steel ring, on which a thin concrete layer is cast. The outer diameter of the steel ring and the thickness of the concrete layer were 170 and 40 mm in the tests of *Malmberg and Skarendahl*

[2] and 305 and 35 mm in the tests of *Grzybowski* [15]. In both cases the concrete was cured for 4 days before the tests were initiated by exposing the outer surface of the specimens to a drying environment of 20 °C and 50 % RH in [2] and 20 °C and 40 % RH in [15]. The type of fibres used was in both cases a straight one with a length of 25 mm and a diameter of 0,3 mm in [2] and 0,4 mm in [15].

The results from both studies on the ring shaped specimens show that the maximum observed crack widths were considerably reduced already at rather low dosages of steel fibres, 20 kg/m³. However, as was pointed out in [2], the limited thickness of the concrete layer enforces a more or less two-dimensional fibre orientation. This implies that the specified fibre volumes in the ring test correspond to higher volumes in a real, thicker, structure.

The other results shown in *Feil! Ukjent bryterargument. (b), Carlswärd* [16], were obtained in a study where 0,9x2,7 m² toppings with thickness of either 60 or 120 mm were exposed to a drying environment, about 16 °C and 60 % RH, after three days of curing. The type of fibres used in this case was Dramix RC-65/35-BN with a length of 35 mm and a diameter of about 0,5 mm, i.e. the same as in the temperature tests. It is clear that the fibre effect was not as significant for the toppings as was the case for the ring tests, although the maximum crack widths were somewhat reduced due to the fibre additions. An explanation to this could be that the cracks in the plain concrete toppings were considerably finer than the ones observed in the plain concrete specimens of the ring test. This means that the potential for a similar crack width reduction, as for the ring test, was rather limited.

A possible reason as to why considerably wider cracks develops in a ring test, i.e. for PC, may be that the restraint conditions are tougher. For toppings a more or less even restraint is provided along the interface zone to the substructure. This means that bond stresses acting along the interface will contribute to the distribution and limitation of cracks. For the ring test on the other hand, the development of bond stresses to the inner steel ring is rather insignificant, thus implying that the restraint condition is similar to a uni-axial tension test. In other words, when a crack arises in a plain concrete ring the material outside the fracture zone will be unloaded and the total elastic strain built up in the concrete will be released in the crack.

4. SUMMARY AND CONCLUSIONS

The principle aim of the presented study was to develop a test method for studying the crack distributing ability of steel fibres in restrained concrete overlays. Accordingly, a test methodology, where temperature gradients were used as loads, was developed and evaluated through two series of tests.

Based on results from these tests some conclusions can be drawn. As regards the effect of steel fibres it was shown that the maximum crack widths were reduced more or less due to a fibre addition. For instance, results indicated that the addition of 30 kg/m³ of steel fibres reduced the maximum crack widths with up to 60 % while the corresponding reduction for a case when 60 kg/m³ were added was approximately 85 %. It was further concluded, or rather assumed based on the difference in surface texture, that the effect of fibres to some extent is influenced by the bond properties of the interface between topping and substrate surface in the sense that the influence seems to be greater as the bond quality diminishes.

Vertical and horizontal movements at free ends were also observed both visually and by means of displacement gauges mounted on the end faces of the toppings. This indicates that de-bonding occurred at the ends between toppings and substrate, at least in some cases. However, there is no general conclusion that may be drawn based on the recordings of end displacement.

On the subject of de-bonding it was also observed that this phenomenon was not exclusively restricted to the ends but was also found in the vicinity of through cracks, in particular for the PC specimens. Naturally, this is due to the fact that two new free ends are established for each crack that extends through the concrete layer.

Although results indicated that the method is suitable for the purpose it can be concluded that a few modifications of the testing procedure are required in order to improve the consistency of the results. In particular, measures need to be taken to ensure that the temperatures are uniformly distributed throughout the various parts of the set-up during the heating phase. From this perspective the main concern seems to be the cooling effects of the surrounding environment, in particular from the supporting floor. Thus, simply by placing an insulating layer underneath the bottom slab it would most certainly be possible to enhance the uniformity of the temperatures. It is further necessary to introduce a system for automatic control of the temperature development in the set-up to allow for a more controlled and repeatable heating procedure.

Furthermore, it is suggested that more LVDT:s are used in future tests to follow the end displacements of the slabs. Within the present test program such deformations were recorded only for the toppings in reference to the floor, as it was assumed that the bottom slabs were rigidly fastened to the substructure. However, results indicate that, although it was possible to distinguish edge lifting of the toppings, the bottom slabs did move throughout the cooling phase. It may further be useful to place some LVDT:s in mid section to verify that the set-up is not bending.

Regarding the preparation of the specimens it is clear that a somewhat more standardised approach is required. In particular, considering that the time between casting and testing varied somewhat for the tests conducted within the present study. As moisture exchange was not restricted throughout the complete period this would imply that the shrinkage strain development was not identical. It may further be suspected that stresses were introduced in the toppings due to differential shrinkage between toppings and slabs. From this reasoning it can be concluded that all tests should be performed at the same time or measures should be taken to restrict the moisture exchange.

ACKNOWLEDGEMENTS

The research project is included as a part of the Doctors of Engineering Programme initiated and partly financed by the Scancem Group (now Heidelberger Zement, Northern Europe). Financial support has also been provided by the Swedish Research Council for Engineering Sciences, TFR, and Betongindustri AB.

REFERENCES

1. Carlswärd, J., "Steel fibre reinforced concrete toppings exposed to temperature deformations – Part II: Finite Element Modelling," to be published.
2. Malmberg, B., and Skarendahl, Å., "Method of studying the cracking of fibre concrete under restrained shrinkage," *Testing and test methods of fibre cement composites*, RILEM, Paris, 1978, pp. 173-179.
3. Grzybowski, M., and Shah, S.P., "Model to predict cracking in fibre reinforced concrete due to restrained shrinkage," *Magazine of Concrete Research*, V. 41, No. 148, 1989, pp. 125-135.
4. Grzybowski, M., and Shah, S.P., "Shrinkage Cracking of Fiber Reinforced Concrete," *ACI Materials Journal*, V. 87, No. 2, 1990, pp. 138-148.
5. Shah, S.P., Ouyang, C., Marikunte, S., Yang, W., and Becq-Giraudon, E., "A method to predict shrinkage cracking of concrete," *ACI Materials Journal*, V. 95, No.4, pp. 339-346, 1998.
6. Groth, P., "Fibre Reinforced Concrete – Fracture mechanics methods applied on self-compacting concrete and energetically modified binders," Doctoral Thesis 2000:04, Luleå University of Technology, Division of Structural Engineering. ISSN: 1402-1544. 2000.
7. Banthia, N., Azzabi, M., and Pigeon, M., "Restrained shrinkage cracking in fibre-reinforced cementitious composites," *Materials and Structures*, Vol. 26, 1993, pp. 405-413.
8. Weiss, W.J., Yang, W., and Shah, S.P., "Shrinkage Cracking of Restrained Concrete Slabs," *Journal of Engineering Mechanics*, V. 124, No. 7, 1998, pp.765-774.
9. Kovler, K., "Testing system for determining the mechanical behaviour of early age concrete under restrained and free uniaxial shrinkage," *Materials and Structures*, Vol. 27, 1994, pp. 324-330.
10. Westin, I., Petersson, Ö., and Nordin, A., "Stålfiberarmerade industrigolv," *CBI Report no 6:92*, (In Swedish), 1992.
11. Banthia, N., Yan, C., and Mindess, S., "Restrained shrinkage cracking in fiber reinforced concrete: A novel test technique," *Cement and Concrete Research*, Vol. 26, No. 1, pp. 9-14, 1996.
12. Geokon, "Instruction Manual Model VSM-4000 Vibrating Wire Strain Gage" Lebanon, USA: Geokon Inc., Geotechnical Instrumentation, 1996.
13. Concrete Report No 4, "Stålfiberbetong – Rekommendationer för konstruktion, utförande och provning," *Svenska Betongföreningen*, Betongrapport nr 4, (In Swedish), 1995, 132 pp.
14. Concrete Handbook - Material, "Betonghandbok – Material," 2nd edition, AB Svensk Byggtjänst, Stockholm, 1994.
15. Grzybowski, M., "Determination of Crack Arresting Properties of Fiber Reinforced Cementitious Composites," Publication TRITA-BRO-8908, Royal Institute of Technology, Department of Structural Engineering, ISSN 1100-648X, 1989.
16. Carlswärd, J., "Steel fibre reinforced concrete toppings exposed to shrinkage and temperature deformations," Licentiate Thesis 2002:33, Luleå University of Technology, Division of Structural Engineering. ISSN: 1402-1757, 2002.

Lattice Girder Elements - Investigation of Structural Behaviour and Performance Enhancements



Ingemar Löfgren
M.Sc. in Civil Engineering
Department of Structural Engineering / Concrete Structures
Chalmers University of Technology
SE-412 96 Göteborg, Sweden
E-mail: ingemar.lofgren@ste.chalmers.se.

ABSTRACT

In an ongoing research programme at Chalmers University of Technology, a study was made of the structural behaviour of lattice girder elements. The project was initiated by AB Färdig Betong and Thomas Concrete together with Chalmers as a response to the growing demand for improved construction methods for in-situ cast concrete structures. The study was based on experiments as well as numerical analyses. Its purpose was to gain knowledge of the structural behaviour and identify performance enhancements enabled by new materials. Through a deep understanding of the structural behaviour coupled with the possibilities to virtually investigate the effects of different material properties, new opportunities are available for an economical and safe way of introducing and using new materials. In the numerical analyses, four different types of concrete were investigated: a normal-strength concrete (C30), a fibre-reinforced normal-strength concrete (FRC30), a high-strength concrete (C80), and a fibre-reinforced high-strength concrete (FRC80). The results show that the structural behaviour of the lattice girder elements can be simulated and that, by changing the behaviour and properties of the concrete, both the peak load and the stiffness of the elements can be increased. For high-strength concrete an increased toughness seems to be important.

Key words: In-situ cast concrete, lattice girder elements, structural behaviour, experiments, numerical analysis, fracture mechanics, fibre-reinforced concrete.

1. INTRODUCTION

In this paper, the structural behaviour of the lattice girder system is studied and, with this as a basis, performance enhancements of the system are discussed and analysed. The ideas and methods presented are based on experimental and numerical studies together with current knowledge and developments in materials science and structural engineering. An experimental program was set up to investigate the behaviour in question. The lattice girder system has been used as a case study in order to explore the potential value of new materials in structural

concrete systems. This approach could lead to a safe and economical way of introducing new materials like fibre-reinforced concrete. The reason for choosing the lattice girder system is that it is thought that new materials might enhance the performance of the elements. Moreover, in design practice in Sweden, there is a lack of a consistent mechanical model able to describe the structural behaviour of the elements and the phenomena of failure. This study has been limited to reinforced elements, not considering prestressed elements, and it focuses chiefly on the construction stage and the structural behaviour. The experimental results, in combination with non-linear finite element analysis based on fracture mechanics, will be used in the future for verification of a proposed analytical model, but now mainly for investigating performance enhancements of the system. The test results and the proposed analytical model can be found in Harnisch [1] and Verdugo [2].

The methods of construction vary depending on the cost of labour, the availability of workers, and the price and availability of construction materials and equipment. In Sweden, where the cost of labour is fairly high, the semi-precast element floor, or lattice girder system, is a popular system for construction of concrete floors. The lattice girder element (see Figure 1) is a permanent participating formwork system, which combines precast concrete panels and poured in-situ concrete topping.



Figure 1. Mounting of lattice girder elements on the construction site (photo, Hans Olsson SKANSKA, Mellerud).

The construction methods for in-situ cast concrete structures must become more efficient and industrialised; this is necessary for the competitiveness of in-situ concrete, and essential if the construction industry is to move forward. At present, the expenditure on labour (preparation and dismantling of formwork, reinforcing, and casting and finishing of concrete) almost equals the cost of material, being roughly 40 percent of all costs; see [3]. To improve the construction and utilise the concrete more efficiently, all parties must be involved (clients, designers, contractors, material suppliers, and researchers). From the viewpoint of structural engineering, there is an urgent need to address these problems, look for innovative design solutions and devote efforts and knowledge to, for example, the development of new structural building/formwork systems. Innovations and improved performance can often be attributed to the use of new or improved

materials. Engineered materials, with enhanced characteristics for a particular application, are increasingly viewed as a source of innovations and development.

2. THE LATTICE GIRDER SYSTEM

The lattice girder element consists of a precast panel with a minimum thickness of 40 mm, a lattice girder (see Figure 2), and bottom reinforcement. The elements are cast in a factory, transported to the site, and lifted into place before in-situ casting. The lattice girder element was introduced in Germany some 40 years ago and has spread to numerous countries. In the early years there was considerable development of the system; beginning with simple beam elements, it evolved into slab and wall (shell) elements. Its most noticeable development concerns the manufacturing process. Today some manufacturers have automatic production plants with CAD/CAM operated equipment (see for example Müller [4]).

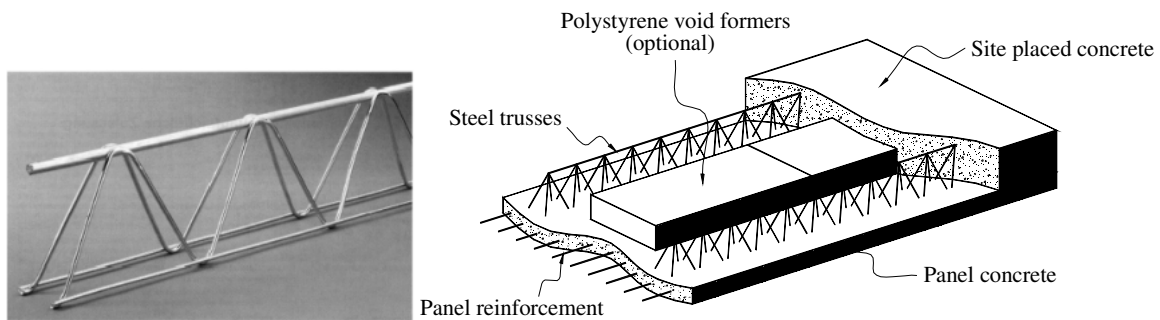


Figure 2. A lattice girder truss and a lattice girder element.

The system has several advantages: stripping and cleaning are unnecessary, the main slab reinforcement is cast into the slab in the factory, the elements require less propping (temporary support also called shoring) than ordinary formwork, installations can be cast into the slab in the factory, surface finish is better, and working conditions are improved. This usually results in reduced site manpower and floor-cycle time. The disadvantages are an increase in material cost, in co-ordination of the design, in requirements of dimensional tolerance, in the difficulties of connection details, and possibly in the size of the crane. Furthermore, propping is still needed.

From the contractor's point of view, there is a desire to increase the spacing of props. This would lead to less congestion and disturbance on site, and minimise the need for temporary works and the associated costs; some reasons can be seen in Figure 3. From the manufacturers' point of view, there is a desire to minimise transportation costs, by reducing the weight and the thickness of the elements.



Figure 3. Simple arguments for why improvements are needed: photos recently taken at a construction site. (Source author)

When designing the elements, the design parameters are the number of trusses, the truss height, the diameter of the top chord, the slab thickness, and prestressing forces. But how the concrete contributes to the structural behaviour is less well known, and this limits progress. For example, can the concrete be allowed to crack and, if so, how does this affect the structural behaviour? How should it be considered in the analysis and, in this context, how should other types of concrete be treated, such as fibre-reinforced concrete? In sum, there is a desire to optimise and refine the system, e.g. reduce the weight and manage longer spans during construction. To achieve this, a better understanding of the structural behaviour is needed.

Materials have developed since the introduction of the system. However, they have not made any significant impact so far. Increased concrete compressive strength and curing condition at moderate temperatures can allow a shorter production cycle. The reason for the lack of materials development could be inadequate understanding of how the material properties of the concrete contribute to the structural behaviour of the system, in particular the behaviour in tension which affects the performance. Besides, it is not until recent times that the building and construction industry has progressed sufficiently in developing and applying new materials (that is, to be able to design or engineer materials) as well as to design structures and components which better utilise these improved properties. This ongoing development was primarily initiated by an increase in the scientific understanding of the origin of material properties at micro-level and the mechanical properties at macro-level, coupled with the advent of numerical tools (like finite element analysis) able to predict the behaviour of structures. For a long time the compressive strength of concrete was considered to be *'the'* property and all other properties used in design were, and still are, assumed to be related to it by empirical relationships – increased compressive strength meant a stronger, better, and more durable material. Nowadays, with our greater understanding of this complex composite material, it is clear that there exist better methods to optimise concrete (e.g. Brandt and Marks [5]; Karihaloo and Lange-Kornbak [6]). These advances will provide the manufacturer with a more reliable material and more tools such as admixtures (shrinkage reducing), additions (silica, fly ash, grinded limestone), inclusions (fibres), advanced curing (e.g. steam curing), etc. Further, the type and volume fraction of aggregates may be used to affect the mechanical properties.

It is important to recognise the possibilities and opportunities that materials offer, as suggested in Figure 4, but also their limitations. To introduce and use these techniques in an economical and safe way, it is necessary to have a deep understanding of the structural behaviour of the

system and how this is linked to the mechanical properties and behaviour of the materials. Nor should one forget that the material properties must be reliable and possible to evaluate with material testing. Today there is a lack of guidelines, in standards and codes, for the use of new materials as well as standardised test methods for evaluating their performance, e.g. for fibre-reinforced concrete and FRP reinforcement.

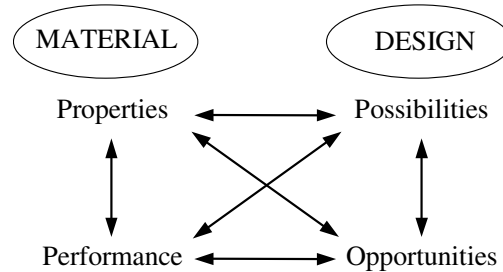


Figure 4. Inter-relationship between materials and design, adopted from James [7].

3. DESIGN AND ANALYSIS

Design and analysis models should, as far as possible, be able to describe the structural behaviour and the phenomena of failure. They should be adequate but not over sophisticated. However, when carefully examining a product like the lattice girder element – which may seem a rather simple product – and considering the entire life cycle from a structural viewpoint, it becomes obvious that design and analysis of it are not a straightforward matter. One has to consider both time-dependent effects (such as creep and shrinkage) and time-dependent material properties (gain in strength and modulus of elasticity), which are affected by environmental conditions throughout the lifetime. This refers to an element with time-dependent boundary conditions (i.e. temporary supports during construction) and time-dependent sectional geometry (i.e. changing from a lattice girder element to a monolithic cross-section with composite action). Moreover, when or even before they are loaded, the elements may exhibit, due to shrinkage and/or transportation, cracking which significantly changes the stiffness. As will be shown later, the tension-softening response of the material has a significant influence on the behaviour.

The structural design of the elements must therefore be performed with regard to the whole life cycle. The different stages to be considered are:

Stage I (Non-composite Action) – prior to placement of concrete, which includes the time:

- (a) during transportation, handling and erection – e.g. cracking during lifting;
- (b) once the formwork is erected but prior to placement of the concrete – e.g. deflections, excessive cracking and damage from construction loads, temporary stabilisation.

Stage II (Non-composite Action) – during placement of concrete until the concrete hardens – e.g. deflections and excessive cracking during casting.

Stage III (Composite Action) – during usage of the structure, which includes:

- (a) normal usage (serviceability limit stage) – e.g. deflections, cracks, vibrations, acoustics, thermal comfort;
- (b) at overloads (ultimate limit state) – e.g. strength, ductility, fire resistance.

The focus of this study is the construction process (Stage I and Stage II). The design objectives for the construction stages can be divided into the serviceability and the ultimate limit states. In

the ultimate limit state (ULS) the main requirement is that the overall system and each of its members should have the capacity to sustain all design loads without collapsing. Adequate strength and safety are achieved if the following failures are avoided: failure of critical sections; loss of equilibrium of the overall system or any part of it; loss of stability due to buckling of the lattice girder or any of its members (the top chord or the diagonals). In the serviceability limit state (SLS) the following requirements should be fulfilled: deflections and local deformations must not be unacceptably large; tensile cracks widths must be limited (or cracking may not be allowed); and local damage must be prevented. Moreover, if cracking is allowed, the crack width in the finished slab (Stage III) must be calculated considering that the element is cracked, and stresses present in the reinforcement before the additional load is applied must be added when calculating the final crack widths and deflections.

The current design practice in Sweden is based on empirical expressions (evaluated from full-scale testing performed 25 years ago) instead of a mechanical model; the only design parameters are the number of trusses, the truss geometry (top chord diameter and truss height), and the slab thickness. Hence, limitations to standard solutions are introduced, because non-standard solutions cannot be treated. Another disadvantage is that the flexural stiffness of the elements is not defined, and as a consequence stresses, strains, deflections, and crack widths cannot be calculated. Furthermore, an accurate stiffness is needed in order to calculate the shoring/propping loads in multi-storey buildings. Additionally, as mentioned, materials like fibre reinforcement are not treated in the existing design method – this is a major impediment to improving the system.

4. TEST PROGRAM

A test series was carried out with twelve lattice girder elements, manufactured by AB Färdig Betong, in the laboratory at the Department of Structural Engineering, Chalmers University of Technology. The main parameters varied were the height of the truss and the diameter of the top bar. The choices of truss geometry were to be representative of standard trusses used in practice. All of the tested slabs had the same outer dimensions (length \times width \times thickness, 2600 \times 1180 \times 50 mm) but had different truss geometries where the height, H , and the diameter of the top chord, ϕ_{top} , were varied; see Figure 5 for description of parameters and Table 1 for test specimens referred to in this paper. In Table 2 the concrete mixture proportions are presented.

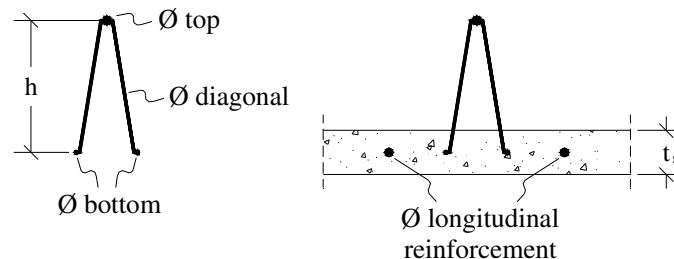


Figure 5. Description of the parameters varied in the test series.

Table 1. Table of test specimens.

Slab No.	ϕ Top chord [mm]	ϕ Diagonal [mm]	ϕ Bottom chords [mm]	Truss height, h [mm]	ϕ Longitudinal reinforcement [mm]	Slab thickness, t_s [mm]
T10-6-5 H=120	10	6	5	120	9 ϕ 10 – s 100	50
T10-6-5 H=150	10	6	5	150	9 ϕ 10 – s 100	50
T10-6-5 H=200	10	6	5	200	9 ϕ 10 – s 100	50
T8-6-5 H=150	8	6	5	150	9 ϕ 10 – s 100	50
T12-6-5 H=150	12	6	5	150	9 ϕ 10 – s 100	50
T10-6-5 H=150/8	10	6	5	150	9 ϕ 8 – s 100	50

Table 2. The concrete mixture proportions for 1 m³ concrete.

Concrete mixture: C 25/35, w/c 0.59, semi-fluid consistence, D_{\max} 18 mm.						
Cement (II/A-LL 42,5) (Bygg.cem. Skövde)	Stone 8 - 18 mm (crushed)	Sand 0 – 8 mm	Water	Plasticizer	Air- entraining admixture	Total weight
[kg]	[kg]	[kg]	[litre]	[litre]	[litre]	[kg]
340	842	949	200	5	0	2330

A test set-up according to Figure 6 was used. Deflections at specific points, and strains in the top as well as the bottom chord, were measured.

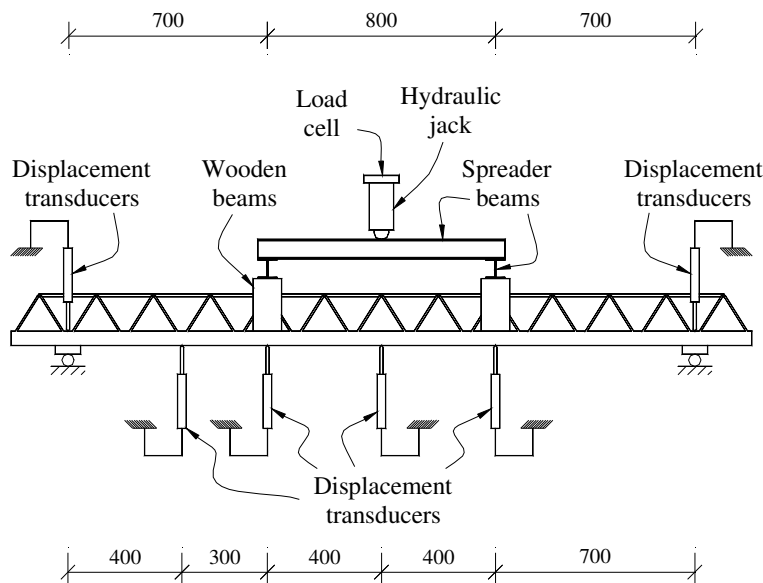


Figure 6. Test set-up used in the experiments.

5. TEST RESULTS

We will now focus on the structural behaviour and discuss the mechanisms underlying it; only some of the results are presented here. For further information on the test series and the results, see Harnisch [1] and Verdugo [2].

5.1 Material Properties

Material properties were obtained from standard material tests: compressive strength on cubes, $f_{c,cube}$, and cylinders, $f_{c,cyl}$; splitting tensile strength on cubes, $f_{ct,sp}$; and modulus of elasticity on

cylinders, E_{c0} (see Table 3). The fracture energy, G_F , was tested in an earlier experiment (see Löfgren [8]) and, since the same concrete mix was used, it was assumed that the result from this test could be used in the numerical analysis ($G_F = 133 \text{ Nm/m}^2$).

Table 3. Measured material properties of the concrete, at 28 and 42 days.

Material property	Age [days]	Age [days]
	28	42
$f_{c,cube}$ [MPa]	46.5	-
$f_{ct,sp}$ [MPa]	3.6	-
$f_{c,cyl}$ [MPa]	33.5	35.3
E_{c0} [GPa]	25.1	25.6

The lattice girder truss is produced by welding cold-worked reinforcement (see Figure 2). The reinforcement in the truss was of the type Ps700, with a measured tensile strength, $f_{0.2}$, of 720 MPa and measured modulus of elasticity, E_s , of 210 GPa. The reinforcements used in the concrete slab were ribbed hot-rolled bars of Swedish type K500, with a measured yield strength, f_y , of 586 MPa and measured modulus of elasticity, E_s , of 211 GPa.

5.2 Structural Behaviour

The main drawback with concrete is the brittleness problem; cracking of concrete usually takes place at low stresses and is thus, in almost every case, inevitable in reinforced concrete elements. Large crack widths are not aesthetically appealing and may also cause initiating of reinforcement corrosion in severe environments. Furthermore, the structural behaviour is highly influenced by cracking and the cracking process, it results in a gradual reduction of the stiffness, as can be seen in Figure 7.

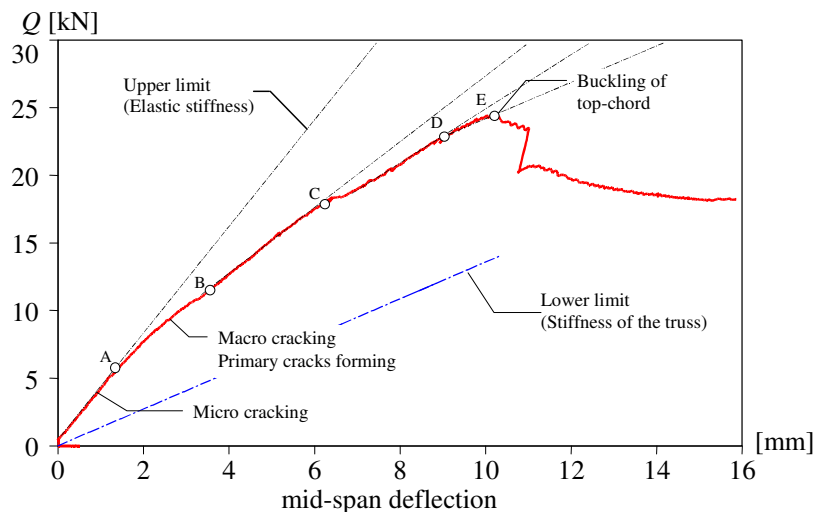


Figure 7. Typical load–deflection curve, for slab T10-6-5 H=150.

Generally, the load-deflection behaviour is characterised by the following. The initial, almost linear relationship between load, Q , and deflection applies until the onset of macro-cracking (A). The cracks continue to grow and form as the load, Q , increases; in the load–displacement curve this is indicated in a region of decreasing stiffness (A-B). Primary cracks are primarily initiated where the diagonals intersect each other. A second near-linear range of behaviour occurs until the next set of primary cracks is formed (B-C). A third near-linear range of behaviour occurs when the crack pattern is well developed (C-D). The last stage (D-E) is reached when the top

chord of the lattice girder is affected by second-order effects, which reduce the stiffness of the system; this takes place until buckling occurs and the peak load is reached (E).

What is interesting with the lattice girder system is that relatively small reinforcement strains and small crack widths are introduced due to the geometrical configuration: the reinforcement is placed in the middle of the concrete slab. The crack widths are relatively small, typically < 0.1 mm at peak load and < 0.2 mm at a deflection of $L_0/100$, and are not visible until about 60 percent of the peak load. The measured strains are typically on the order of $500-1000 \times 10^{-6}$ at peak load, and less than 300×10^{-6} at 60 percent of the peak load; see Figure 10. However, the geometry of the truss (height and diameter of the top chord) influences the strain distribution in the section. For the same top chord diameter, a higher truss results in smaller strains in the bottom chord. For the same truss height, a larger top chord diameter results in larger strains in the bottom chord. As a result of the relatively small reinforcement strains and crack widths, the ability of concrete to carry tensile stresses after cracking plays a significant role for the tension-stiffening effect in the service stage. This is important for limitation of deflections, which is one of the main design parameters. The load–deflection curves are presented in Figures 8 and 9. Figure 10 shows a typical load–strain curve for the embedded truss reinforcement. Figure 11(a) shows the obtained crack pattern and 11(b) shows a deformed truss..

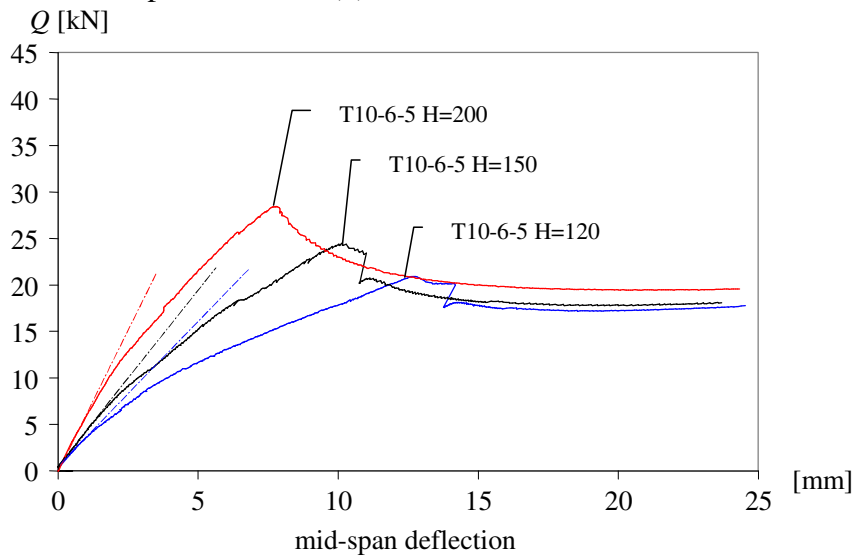


Figure 8. Load versus mid-span deflection, influence of the truss height.

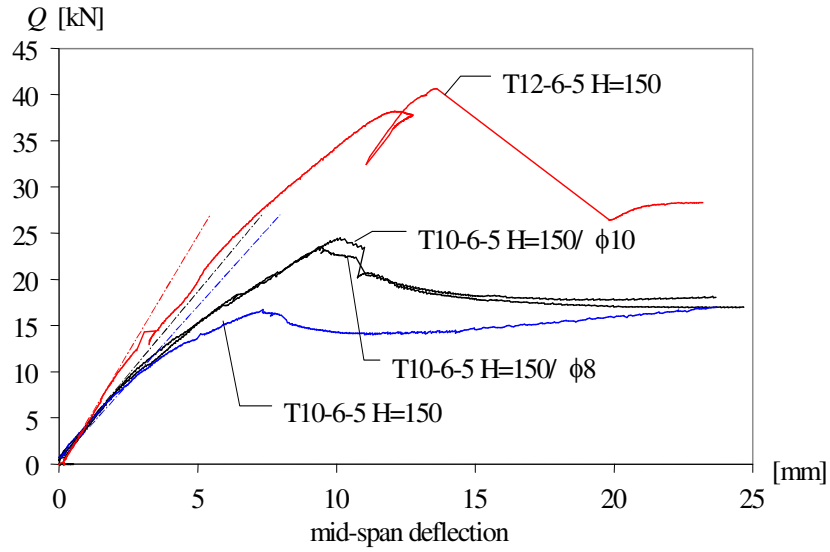


Figure 9. Load versus mid-span deflection, influence of the top chord diameter.

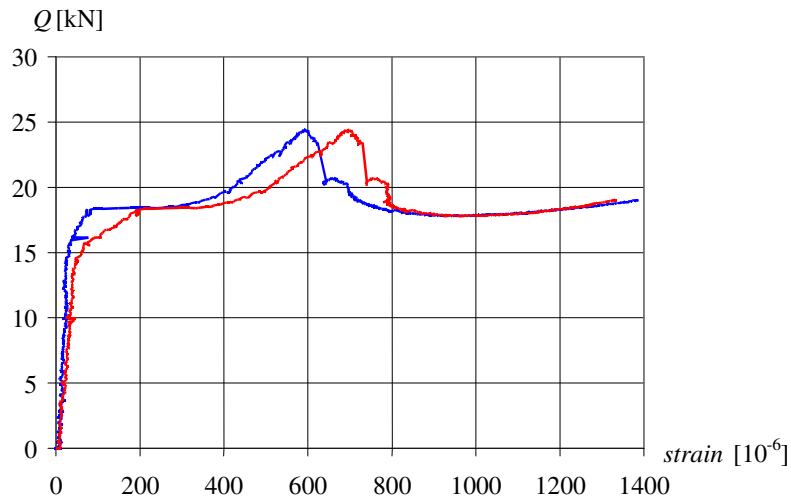


Figure 10. Typical load-strain curve for the embedded truss reinforcement, measured at mid-span, for slab T10-6-5 H=150.

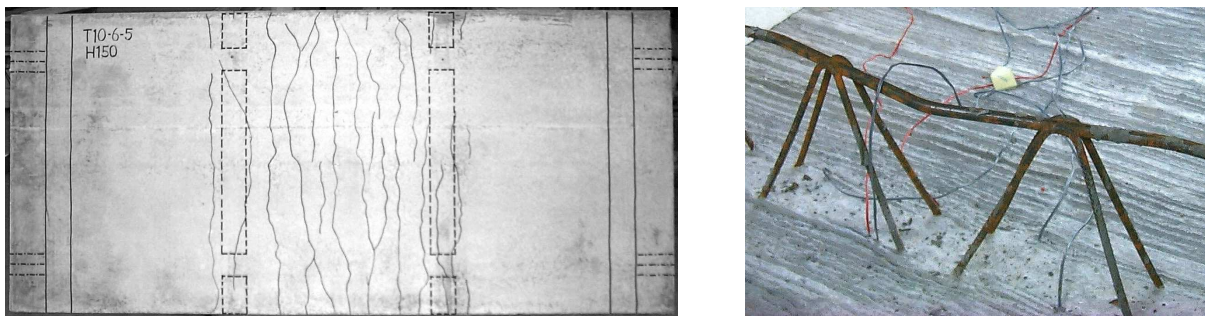


Figure 11. (a) Crack pattern after a deflection of 30 mm, for slab T10-6-5 H=150. Dotted lines towards the centre of the slab indicate where the load was applied and the continuous lines at the ends indicate the supports. (b) Photo showing the deformed truss.

6. NUMERICAL ANALYSIS

Numerical analysis (e.g. finite element analysis) provides possibilities to analyse complex problems, but also to virtually study the effect of different material properties and geometrical configurations. A finite element model was set up in the program DIANA [9]. From the tests it was realised that the structural behaviour is governed by three main mechanisms: buckling of the lattice girder at peak load (see Figure 11 b), cracking (see Figure 11 a), and tension stiffening (see Figure 7 and 10). Hence, the elements and material models to be used in the analysis should be able to represent the non-linear phenomena of buckling (geometric non-linearity), cracking (material non-linearity), and slip of the reinforcement. When modelling, there is always a careful balance needed between the level of detailing and the complexity of the problem, the desired output and the ‘accuracy’ of the results and the pros and cons always have to be considered carefully when choosing models and elements for the FE model. For example, during the modelling and analysis process it was experienced that the inclusion of a bond-slip improved the localisation of primary cracks and the convergence.

6.1 Finite Element Model

In the numerical analysis, the concrete slab was modelled with curved shell elements, which are good at describing bending, with eleven integration points in the thickness direction. Curved higher-order beam elements represented the lattice girder, while truss elements represented the other reinforcement. In order to capture the buckling load, the top chord was given an initial sinusoidal imperfection, with a maximum value of 0.1% of the top bar diameter. Both the reinforcement and the lattice girder were modelled with the von Mises plasticity condition. The model is shown in Figure 12.

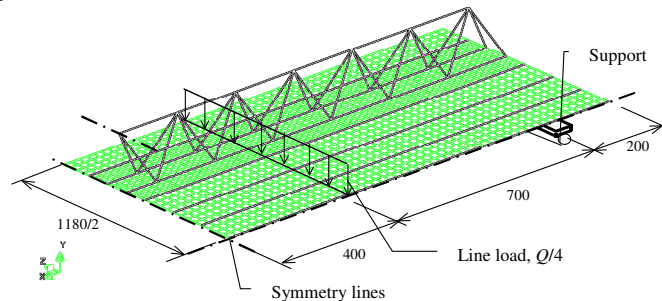


Figure 12. Finite element model representing a lattice girder element (due to symmetry, only a quarter of the slab needs to be modelled).

The connection between concrete and the reinforcement (both the lattice girder and the ordinary reinforcement) was modelled with interface elements, which were given a bond-slip relationship according to the CEB-FIP MC90 [15]; see Figure 13(a). For the bottom chord of the truss (lattice girder), confined concrete with good bond conditions was chosen, the reasons being that the bar diameter is only $\phi 5$ and no splitting cracks were observed during the tests (i.e. failure by shearing of the concrete between the ribs). For the $\phi 10$ reinforcement, unconfined concrete with good bond conditions was chosen. To capture cracking of concrete, the concept of a smeared, rotating crack model, based on total strain (i.e. with strain decomposition), was chosen. A tension-softening relationship according to Figure 13(b) was used. It is suggested by Cornelissen *et al.* [13] and describes the relation between the crack stress, σ_{cr} , and the crack strain, ϵ_{cr} , or crack opening displacement. Since the structure is modelled with interface elements representing a bond-slip relationship, the transverse cracks were assumed to, and did, localize within a band width equal to the element size.

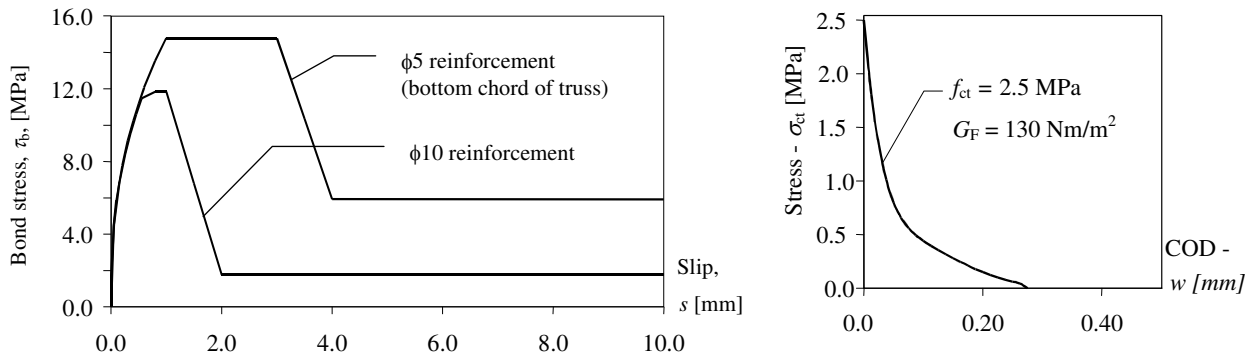


Figure 13. (a) Bond-slip relationship used in the analysis, according to the CEB-FIP MC90. (b) Tension softening used in the analysis, according to Cornelissen *et. al.* [10] (COD = Crack Opening Displacement.)

In compression, a non-linear stress–strain relationship according to Thorenfeldt [11] was used. Biaxial stress states were taken into account by two models available in DIANA: the influence of lateral cracking on the compressive strength by means of a reduction function based on the model proposed by Vecchio and Collins *et al.* [12], and increase in compressive strength due to lateral confinement by means of a model proposed by Selby and Vecchio [13]. An overview of the material properties used in the analysis is presented in Table 4.

Table 4. Material properties used in the analysis.

Material property	Concrete	Reinforcement Ps700	Reinforcement K500
$f_{c,cyl}$ [MPa]	35.0	-	-
f_{ct} [MPa]	2.5	-	-
f_y [MPa]	-	720	586
E_{c0} [GPa]	25.6	-	-
E_s [GPa]	-	210	211
G_F [Nm/m ²]	130	-	-
ν	0.15	0.3	0.3

6.2 Shrinkage Analysis

Since no direct measurement was made of the tensile strength of the concrete, a reasonable value had to be assumed. Based on empirical correlations between tensile strength and the compressive strength and splitting tensile strength, the concrete was assumed to have a tensile strength, f_{ct} , of 2.6-3.0 MPa. However, concrete shrinkage, which took place from the time of manufacturing to the time of testing, introduces tensile stresses in the concrete, resulting in a lower cracking load. To evaluate the shrinkage-induced stresses, an analysis based on the same FE-model was made, considering the time-dependent effects of shrinkage, creep, and material properties (modulus of elasticity). In DIANA, models are available for both creep and shrinkage; the models used in this analysis were based on the CEB-FIP MC90, *creep* being modelled by rheologic Maxwell/Kelvin chains, and *shrinkage* being modelled as age-dependent initial strain. The shrinkage strain was considered as uniform over the thickness of the slab; in reality the surfaces will dry out faster than the core, resulting in additional shrinkage effects. To consider the curing conditions, *curage* is the concrete age in days at the end of the curing period. The elastic and creep deformation for a young concrete will be much larger than for a concrete loaded at later stage; the model codes therefore give different superposable creep curves for

loading at different young concrete ages. The creep and shrinkage models require additional data, and the following inputs were given; see Table 5.

Table 5. Model parameters used in the analysis.

Model parameter	Creep / Shrinkage
$E_{c,28}$ [GPa]	25.1
modulus of elasticity at 28 days	
$f_{c,cyl,28}$ [MPa]	33.5
compressive strength at 28 days	
H [mm]	48
notational size of the member	
RH [%]	60
ambient relative humidity	
$TEMPR$ [°C]	20
ambient temperature	
$CEMENT$	normal hardening
type of cement	
$Curage$ [days]	2
$Aging$ [days]	2

The result of the shrinkage analysis is shown in Figure 15. The shrinkage-induced stresses are on the order of 0.4 MPa in the bottom of the slab and 1.0 MPa at the top of the slab. Hence, to capture the cracking load, an effective tensile strength of 2.5 MPa was used in the analysis instead of the earlier estimated value of 2.6-3.0 MPa.

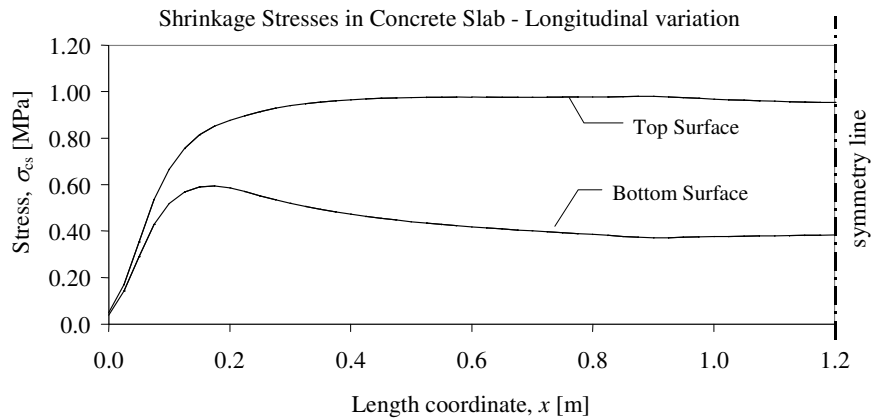


Figure 15. Shrinkage-induced tensile stresses, from numerical analysis.

6.3 Results From Numerical Analysis

The first step was to compare the numerical results with the test results in order to investigate whether the model was able to simulate the structural behaviour in a reasonable way.

The lattice girder element presents several difficulties for the numerical analysis. Since cracking plays such a significant role in the degradation of the stiffness, this must be captured correctly throughout the entire loading process. Hence, a correct crack pattern is needed (number of cracks and their spacing). The peak load was represented accurately. However, the numerical model showed too stiff behaviour, mainly due to insufficient crack localisation. The buckling phenomenon was predicted in a satisfactory manner. The analysis becomes numerically unstable as soon as cracking starts, and has convergence problems in some load steps. In Figure 16, a comparison is made between the numerical and experimental load–deflection curves for slab

Structural Modelling and Testing – Summary of a Concrete Café at the 18th Nordic Concrete Research Meeting, Elsinore, Denmark



Prof. J. Silfwerbrand, Ph.D.
johan.silfwerbrand@cbi.se

Swedish Cement and Concrete Research Institute
SE-100 44 Stockholm, Sweden

ABSTRACT

This short paper is a summary of a so called concrete café held at the Nordic Concrete Research Meeting in June 2002 in Elsinore, Denmark. Four papers were presented; two were devoted to dynamics and two to steel fibre reinforced concrete structures. This paper gives brief summaries of the four papers and tries to summarise the discussions.

Key words: Dynamics, SFRC, structural modelling, discussions.

1. INTRODUCTION

Following up the promising result of the concrete cafés in Reykjavik at the previous Nordic Concrete Research Meeting in 1999, four concrete cafés were held at the 18th Nordic Concrete Research Meeting in June 2002 in Elsinore, Denmark. The idea of a concrete café, as understood by the author, is to arrange a technical session in a friendly and informal atmosphere and provide more time for discussions. The author had the honour to chair one of the concrete cafés in Elsinore. The theme of this concrete café was “Structural Modelling and Testing”. Four papers were presented. They could easily be grouped in two parts; one devoted to structural dynamics and one to steel fibre reinforced concrete (SFRC) structures.

The concrete café was divided into two parts with an intermediate coffee break. Ansell ([1] and Svahn [2] presented papers on structural dynamics and Carlswärd [3] and Kanstad [4] presented papers on SFRC structures. Thorough discussions followed the two presentations in both parts. Since the papers easily could be found and read in the proceedings [1-4], this paper is focused on the discussions. Approximately 30 participants attended the concrete café.

2. PART ONE: STRUCTURAL DYNAMICS

Anders Ansell, Royal Institute of Technology, Stockholm, Sweden, opened the session by presenting his paper on modelling of shotcrete on rock subjected to blast induced vibrations [1]. The blasting process leads to that fresh concrete is subjected to vibrations that might be detrimental for the fresh concrete itself and for the bond between concrete and rock. To analyse this problem, Ansell uses an elastic finite element model. It consists of beam and spring

elements and considers the effect of fractured rock. By comparisons with tests, the model is shown to be able to accurately describe the response of shotcrete linings exposed to vibrations.

Per-Ola Svahn, Chalmers University of Technology, Gothenburg, Sweden, presented an experimental study on pile driving using the modified Hopkinson pressure bar [2]. This test method can be used to determine the dynamic tensile strength of concrete. The dynamic tensile strength is considerably higher than the static one and is highly affecting the structural behaviour of the concrete pile.

In the common discussion, Svahn explained the difference between the original Split Hopkinson Bar (SHB) and the modified one. In the original test, a projectile is hitting a system of three parts. The test specimen is the intermediate one. In the modified test, the system has only two parts. The test specimen is the second one that is not hit directly by the projectile. The modified Hopkinson pressure bar seems to give very promising results.

How to treat the boundary conditions (rock, rock bolts, bond, projectile, clay or gravel) is fundamental for interpreting the results from a FE analysis. Ansell uses beam and spring elements to model shotcrete and fractured rock. Svahn has not started his numerical analyses yet, but the modelling of the clay and the contact zone between clay and pile will be subjected to thorough investigations.

Svahn also explained that increased strain rate influences tensile strength much more than compressive strength. It depends on differences in the cracking and failure pattern.

The chairman asked if the beneficial strain-rate influence on tensile strength might cancel out the detrimental load magnification at dynamic loading. In practical pavement design, dynamic effects are considered neither on loads, nor on strength. Håkan Sundquist, Royal Institute of Technology, Stockholm, Sweden, regarded this as an interesting hypothesis that needs research.

3. PART TWO: STEEL FIBRE REINFORCED CONCRETE STRUCTURES

Jonas Carlswärd, Betongindustri, Stockholm, Sweden, presented his research project on SFRC overlays [3]. He has developed a new test set method to study the effects of imposed deformations on the behaviour of restrained concrete overlays. In stead of studying very slow shrinkage movements, Carlswärd has used heating cables to produce thermal differences between the overlay and the bottom slab (substrate). He has used his test set-up to investigate the effects of fibres on the cracking behaviour of the overlay. As might be assumed, cracks in SFRC overlays are finer than cracks in plain concrete overlays. Furthermore, the tests show that increased fibre content decreases the crack width.

Terje Kanstad, Norwegian University of Science and Technology, Trondheim, presented tests on SFRC beams [4]. Bending moment and shear capacities have been tested in beams with combined (minimum) flexural reinforcement bars and fibre reinforcement. The bending capacity increases with increased fibre content while the ductility decreases. An increased fibre content implies also an enhanced shear capacity.

The chairman reported that previous research shows that crack control in SFRC demands increased fibre content due to increased concrete strength [5]. Carlswärd's test results do not contradict this statement.

In the Swedish Concrete Association's SFRC guidelines [6], two different methods to compute shear strength of SFRC beams are described. Both are using the superposition concept, but they are treating the fibre effect differently. The fibres could either be assumed to enhance the concrete contribution V_c or constitute an additional contribution V_f . In a master thesis at the Royal Institute of Technology [7], it was concluded that the second method, that was adopted by the Swedish Concrete Association, showed the best agreement between test results reported in the literature and computational formula. Kanstad's test results were evaluated towards the latter approach using the general shear capacity formula from the Norwegian Standard, NS3473, and the additional fibre contribution adopted by the Swedish Concrete Association [6]. Mikael Bræstrup, Rambøll, Virum, Denmark, stated that computation formulae containing parts from different studies are doubtful to use. Kanstad responded that the Norwegian steel fibre project just has started and that more research within this field will be carried out soon.

The concrete café was ended with a discussion on the economical benefits of using SFRC. Håkan Sundquist said that fibres are uneconomical. If you develop a complete concept where SFRC is a part, this concept might have a potential. Terje Kanstad stated that there is a lack of skilled concrete workers with knowledge on reinforcing structures. SFRC that you just pour into the form is an interesting alternative, but still the main part of the structural elements like beams, slabs and walls will need a certain amount of ordinary flexural reinforcement to meet the ductility requirements.

REFERENCES

1. Ansell, A., "Modelling of Shotcrete on Rock Subjected to Blast Induced Vibrations". *Proceedings*, 18th Nordic Concrete Research Meeting, Elsinore, Denmark, June 2002, pp. 48-50.
2. Svahn, P.-O., & Gylltoft., K., "Impact loaded Concrete Structures – Experimental study with Modified Hopkinson Pressure Bar". *Proceedings*, 18th Nordic Concrete Research Meeting, Elsinore, Denmark, June 2002, pp. 84-87.
3. Carlswärd, J., "A Test Method for Studying Crack Development in Steel Fibre Reinforced Concrete Overlays due to Restrained Deformation". *Proceedings*, 18th Nordic Concrete Research Meeting, Elsinore, Denmark, June 2002, pp. 54-56.
4. Kanstad, T., & Stemland, H., "Steel Fibre Reinforced Concrete Beams". *Proceedings*, 18th Nordic Concrete Research Meeting, Elsinore, Denmark, June 2002, pp. 72-74.
5. Westin, I., Petersson, Ö., & Nordin, A., "Steel Fibre Reinforced Concrete Floors". Commission report No. 94015. Swedish Cement and Concrete Research Institute, Stockholm, Sweden, 1994. (In Swedish).
6. Swedish Concrete Association, "Steel Fibre Reinforced Concrete – Recommendations for Design, Construction, and Testing", *Concrete Report* No. 4, 2nd Edn, Stockholm, Sweden, 1997. (In Swedish).
7. Hällgren, A., "Shear Capacity of Concrete Beams with Co-operating Bar and Fibre Reinforcement". Master thesis, Royal Institute of Technology, Dept. of Structural Engineering, 1997. (In Swedish).

Steel Fibre Reinforced Concrete toppings exposed to temperature deformations – Part II: Finite Element Modelling



Jonas Carlswärd, Tech. Lic.
Betongindustri AB, Luleå Technical University
100 74, Stockholm, Sweden
E-mail: jonas.carlsward@betongindustri.se

ABSTRACT

The study deals with a two-dimensional Finite Element Model, developed with the FE code *DIANA* [1] for studying the formation of cracks in restrained concrete toppings subjected to temperature loads. It constitutes the second paper in a series of two. The first paper, *Carlswärd* [2], deals with a test method for the situation, including details on the experimental set-up and procedure adopted as well as results from an extensive test program involving both plain and steel fibre reinforced concrete specimens.

In the analysis the main variables focused on were the concrete properties in addition to the bond quality of the interface to the sub-structure. The simulations were further compared to experimental results in order to verify the accuracy of the numerical predictions. As expected the results indicated that both the interface properties topping-slab as well as the tensile response of the concrete play important roles as regards the fracture response. However, the correlation with experimental results was not satisfactory.

Keywords: FEM, Temperature, Restraint, Cracks, Steel fibres, Bond, Toppings.

1. INTRODUCTION

The fracture response of thin layers of concrete exposed to imposed strains is typically characterised by vertical cracks that extend through the depth in addition to shearing along the interface between overlay and substrate. Thus, not only the properties of the concrete but also the quality of the bond between topping and substrate have significant influence on the structural behaviour. This was also recognized in *Groth* [3] where it was stated that depending on the quality of the bond the mode of failure would range from complete de-bonding for a “poor bond situation” to well-distributed cracking for a situation with full restraint. This is applicable both for plain as well as for fibre reinforced concrete.

In order to learn more about the factors that influence the mode of failure for thin toppings subjected to restrained deformation a test method was developed in which concrete specimens were exposed to temperature differentials. Results from the study showed that the effect of a

fibre addition on the crack widths varied somewhat. A considerable contribution was observed in some cases, i.e. substantial crack width reductions, while the effect was less pronounced in other cases. Based on these observations, and the fact that the roughness of the interface between slab and topping varied, it was concluded that the crack propagation in a topping is influenced not only by the type and amount of fibres, but also by the quality of the bond. More specifically the results indicated that the poorer the bond the greater the effect of the fibre addition. Details on the adopted procedure as well as results from two series of tests are presented in the first paper in a series of two, *Carlswård* [2].

The present paper, which accordingly is the second in the series, describes a two dimensional Finite Element Model developed primarily to simulate the behaviour of the tested specimens. Following from the above reasoning, the study also aims at investigating the influence of the concrete softening and the interfacial bond on the fracture response. In that respect numerical modelling provides a powerful tool as it allows for rapid assessments of the effect of various parameters.

2. FINITE ELEMENT MODEL

2.1 Testing procedure

A short presentation of the set-up and test procedure adopted for the restrained temperature tests are briefly provided here in order to give a background to the Finite Element analysis. The main ambition of the tests was to use temperature loads to create a state of stress in a concrete topping that would resemble the one appearing due to one-directional drying shrinkage. Thus, an important feature was to generate a temperature difference between the top and bottom face of the overlay. At the same time it was necessary to restrain the specimens to avoid free deformation. The testing technique adopted to fulfil these requirements is schematically presented in *Figure 1*.

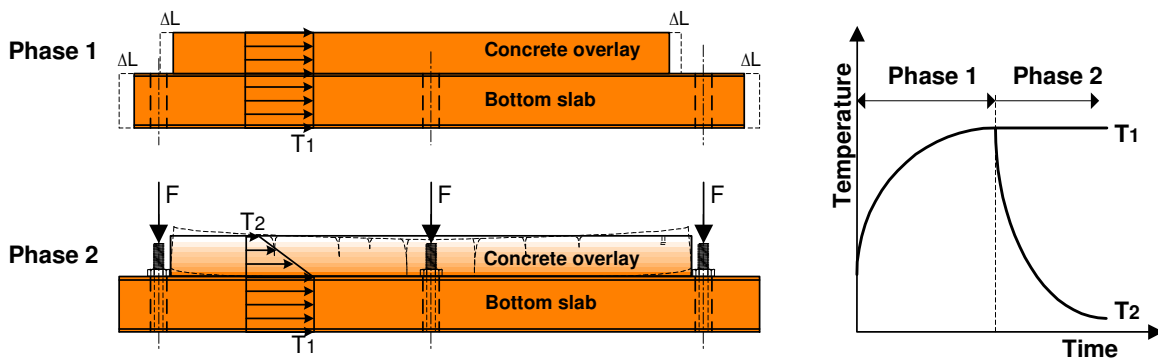


Figure 1 – Schematic illustration showing the different phases of the test procedure. (Phase 1 – heating of overlay and bottom slab. Phase 2 – Cooling of overlay).

The test procedure was divided into two phases, 1 and 2. In the first of these, during which the bottom slab was free to move, the temperatures were gradually increased in the various parts of the set-up using embedded heating cables. After reaching the temperature distribution aimed at the bottom slab was fastened to the floor by applying loads to restraining ties. In theory this would prevent further displacements of the test set-up, implying that the bottom slab from this point on could be seen as a rigid base. The second phase was then characterized

by a gradual decrease of the temperature starting from the upper surface of the topping. In this way a rather steep temperature gradient was produced which successively lead to the formation of cracks.

2.2 Model description

A two-dimensional finite element model was developed using the finite element code DIANA, see *Figure 2*. The model consisted of a 150 mm thick topping on a 200 mm bottom slab that was supported by an inflexible floor. Four-noded rectangular plain stress elements of the type Q8MEM, as shown in the figure, were used to simulate the topping and the substrate slab. The mesh generated for the topping consisted of 576 elements, each with a width of 25 mm and a height of 18,75 mm. The thickness was assumed to be 600 mm in accordance with the toppings of the tests. For the bottom slab a corresponding number of 768 quadratic elements with 25 mm sides in the plane and a thickness of 1400 mm were used.

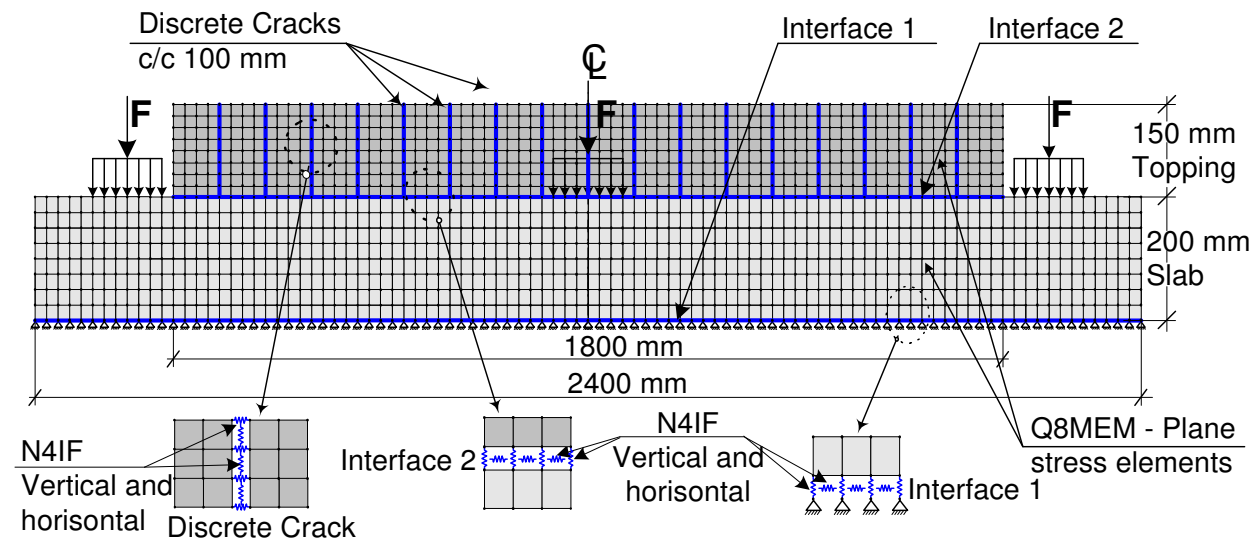


Figure 2 – Finite Element Model (FEM) developed to simulate the behaviour of restrained toppings exposed to temperature loads.

Furthermore, two-noded structural interface elements of the type N4IF were employed to simulate the material characteristics of both the layer between slab and floor, interface 1, and topping and slab, interface 2. Structural interface elements were also positioned between two successive columns of membrane elements at each 100 mm to model the development of cracks in the topping. Other distances between discrete cracks were also attempted before deciding on this space. A similar response was obtained for a shorter distance, 50 mm while a space of 200 mm resulted in stress levels exceeding the prescribed tensile strength in between some of the discrete cracks. The response of the model, i.e. the distribution of cracks, was also verified by means of a smeared crack model.

The two nodes between which each structural interface element was positioned had the same initial coordinates, i.e. the points overlapped. The reason for this was that the interfaces, in reality, have no physical distribution. For both the layer describing the bond between topping and slab, interface 2, as well as for the discrete cracks, double interface elements were put at each position. The reason for this was to be able to separate the response in vertical and horizontal direction. Differently, for the layer between slab and floor, interface 1, only one

nodal interface element was applied at each position. Here, half of the number of elements was active in vertical direction while the other half was active in horizontal direction.

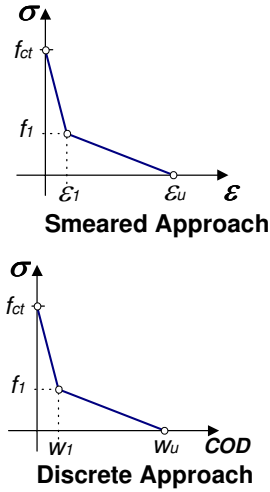
2.3 Material models

The main feature of a discrete approach is that both the positions as well as the direction of cracks are prescribed in the structure. Thus, in situations where a multi-directional state of stress may be expected such an approach is usually not preferable since the principal strength requirement may be violated in any direction, i.e. the stress in a principal direction may exceed the strength of the material. However, for the type of application studied here a tensile stress field that predominantly acts in a longitudinal direction may be expected. This implies that cracks mainly form in a vertical direction as is also assumed in the analysis.

In order to assure that the strength requirement was not violated in between the prescribed discrete cracks, a smeared crack model was assigned for the membrane elements. The implication of which is that a crack is assumed to form as soon as the maximum principal stress in an element reaches the tensile strength. However, different from a discrete approach, where softening is restricted to localised fracture zones, the smeared theory assumes that the displacement jump that follows from the initiation of a crack is averaged over the whole finite element, *Elfgren* [4]. Consequently, rather than specifying a relation between stresses and displacements, as is the case for a localized crack model, a relation is set between tensile tractions and strains. This means that the stress versus crack opening curves obtained from e.g. tensile tests cannot be directly introduced in the model. Firstly, the displacements need to be transformed into strains. This is done in a smeared approach by dividing the crack opening displacements, COD:s, by an assumed crack band width, h_{cr} , which is typically related to the element size.

As shown in *Figure 3* bi-linear relations were set between tensile stresses and strains or displacements for the smeared and discrete approach respectively. The various parameters assigned to describe the shapes of the softening curves for plain and fibre reinforced concrete respectively are inscribed in the table. To some extent these values were selected in order to reflect the experimentally obtained uni-axial tensile properties as presented in *Carlswärd* [2]. In the case shown here the tensile response used for the SFRC approximately corresponds to a concrete with 30 kg/m^3 of steel fibres, as obtained for test I:1 in the experimental program.

The reason why slightly lower tensile strength was assigned for the discrete cracks as compared to the smeared, 3,1 and 3,3 MPa, was to ensure that cracks would, at least initially, develop at the prescribed positions. Another important motive was that it improved the numerical stability of the model.



Material Property	Smearred approach		Discrete Approach	
	PC	FRC	PC	FRC
E_c , GPa	30	30	30	30
ν , -	0,2	0,2	0,2	0,2
α , $^{\circ}\text{C}^{-1}$	$1 \cdot 10^{-5}$	$1 \cdot 10^{-5}$	$1 \cdot 10^{-5}$	$1 \cdot 10^{-5}$
f_{ct} , MPa	3,3	3,3	3,1	3,1
f_1 , MPa	0,7	1,2	0,7	1,2
ϵ_B , -	0,0012	0,0012	-	-
ϵ_w , -	0,06	0,4	-	-
w_1 , mm	-	-	0,03	0,03
w_w , mm	-	-	0,15	10

Figure 3 – The graph illustrates the principle stress-strain relation used to describe the softening of the concrete and the values inscribed in the table represent the actual parameters used in the analysis to describe Plain Concrete and Fibre Reinforced Concrete respectively.

Shown in the table of Figure 3 are also the parameters used to describe concrete in the uncracked stage, an elastic modulus, E_c , of 30 GPa and a Poisson's ratio, ν of 0,2. Furthermore, to be able to model the effect of temperature changes the coefficient of thermal expansion, α , was set to $10 \cdot 10^{-6} \text{ }^{\circ}\text{C}^{-1}$. These parameters have not been obtained from tests on the specific concrete used in the experimental program. However, quite a few previous studies, as referred to in the *Concrete Handbook - Material* [5], have indicated that the values assumed here are reasonable. For instance, regarding the coefficient of thermal expansion, it was shown in a study conducted by *Detting* [6], that a value of approximately $10^{-5} \text{ }^{\circ}\text{C}^{-1}$ can be expected for concrete composed with a cement content of 350 kg/m^3 and granitic or gneissic aggregates that is stored in air. Due to the increased temperature during a test it is however likely that the value may increase slightly. Results from experiments by *Wiegler and Fischer* [7], show that the coefficient of thermal expansion increases from about 10 to $12 \cdot 10^{-6} \text{ }^{\circ}\text{C}^{-1}$ as the temperature increases from 20 to 80°C , which was the case here.

A drawback of the FE-model is that creep has not been accounted for. The reason for this was that visco-elastic behaviour was not an option for the discrete elements. However, considering the short-term nature of the temperature load it is likely that the favourable influence of creep on the stress development in the concrete was rather insignificant in this case.

The assumed material characteristics of the interfaces, 1 and 2 in Figure 2, are shown in Figure 4. For the tests the restraint was minimized along the interface between slab and floor by covering the floor with plastic sheet. This situation was modelled with Coulomb friction in horizontal direction for the corresponding interface (interface 1). The friction model made it possible to simulate a practically free sliding situation in the unloaded state, i.e. during the first phase of the analysis when the various parts of the model were heated up. After the restraining ties had been stressed, i.e. during the second phase of the analysis, the interface provided a resistance to sliding. In the model, two parameters were specified, a cohesion c and a friction angle ϕ . Different values as well as combinations of values were attempted before eventually deciding for a cohesion factor c of 10 Pa (negligible) and a friction angle ϕ , or rather $\tan\phi$ of 0,6. In addition, a non-linear elasticity model, with virtually no tensile

resistance but with substantial compressive resistance f_c was assigned for the vertical interface elements to model the rigidity of the floor.

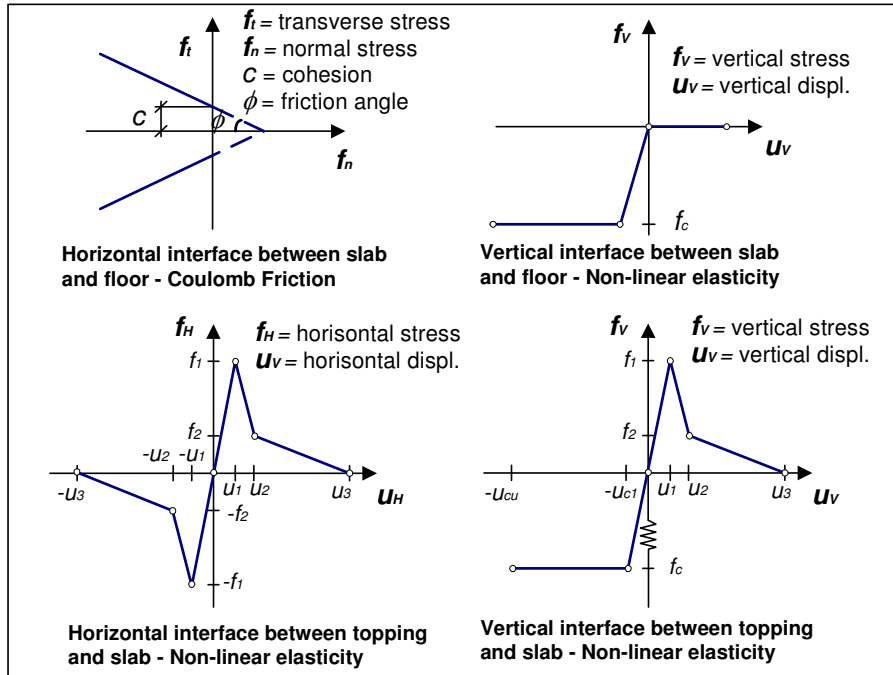


Figure 4 – Material models assigned for the horizontal and vertical structural interface elements between both the floor and the slab as well as between the slab and the topping.

For the interface between toppings and slab, a continuous restraint, mainly constituted by adhesive bond, was produced in the tests. This restraint situation was modelled by assigning non-linear elasticity in both horizontal and vertical direction for the interface elements connecting the topping with the slab. In these models the maximum value corresponds to the ultimate adhesive strength, f_1 in Figure 4. Similar to the post-cracking properties of the concrete bilinear softening relations were then specified to simulate the small residual strength that may be expected even after the adhesive bond has been exceeded, f_2 in Figure 4. Within the present analysis two different conditions were studied; poor and good bond quality. The values assumed in each case are inscribed in **Feil! Ukjent bryterargument..** The “poor” bond situation corresponds to results from a single vertical bond test performed for one of the tested toppings while the parameters adopted for the “good” bond situation were fabricated.

Table **Feil! Ukjent bryterargument.** – Parameters used for the non-linear elasticity models assigned for the structural interface elements between topping and slab.

Bond Quality	Interface – Vertical direction					Interface – Horizontal direction				
	u_1 (mm)	f_1 (MPa)	u_2 (mm)	f_2 (mm)	u_3 (mm)	u_1 (mm)	f_1 (MPa)	u_2 (mm)	f_2 (mm)	u_3 (mm)
Poor	0.00075	1.2	0.02	0.2	0.1	0.001	1.2	0.02	0.2	0.1
Good	0.00125	2.0	0.02	0.33	0.1	0.00167	2.0	0.02	0.33	0.1

As only one test has been conducted so far to evaluate the bond strength, by exposing a drilled cylinder to uni-axial tension, there is no way of knowing if the assigned values are in fact representative for the tests. However, previous tests, as presented in *Silfwerbrand* [8], have shown that the vertical bond strength typically assumes a value of about 1 MPa for

mechanically treated surfaces and in most cases exceed 2 MPa for water-jetted surfaces. This indicates that the assigned values are reasonable in magnitude even though slightly lower strength could perhaps be expected for the poor bond situation. It is though important to mention that the choice of interface properties has a great impact on the numerical stability of the analysis. This narrowed the span within which the bond strength could be varied.

In *Feil! Ukjent bryterargument*, it can further be seen that the same response was assumed in horizontal and vertical direction. To some degree this assumption is supported by results presented in section 12.7:1 of the *Concrete Handbook – Material* [5]. Based on a study conducted by *Silfwerbrand* [8], it is shown here that the shear strength of the interface, as calculated from tests with combined compressive and shear stresses, reaches approximately the same value as the vertical tensile bond strength.

2.4 Temperature distribution

The toppings were exposed to non-linear temperature gradients that were produced following the procedure briefly described in section 2.1. However, the temperature distributions obtained in the various tests of the experimental study were not identical. Reasons for this were both that the technique used for producing the temperatures as well as the method of generating the gradients over the toppings were successively developed from test to test. To simulate the response of each of the individual tests performed within the experimental program would therefore require the temperature load to be changed accordingly. Thus, for the sake of convenience it was decided to use only one temperature distribution here, the one obtained for the last test performed in the second series, test II:4.

A graph showing the corresponding development of temperatures at various positions in the bottom slab and topping as well as a drawing describing the position of the measuring gauges are shown in *Figure 5*. A more detailed discussion on the methods used to develop the temperatures as well as the way of recording temperatures can be found in *Carlswård* [2].

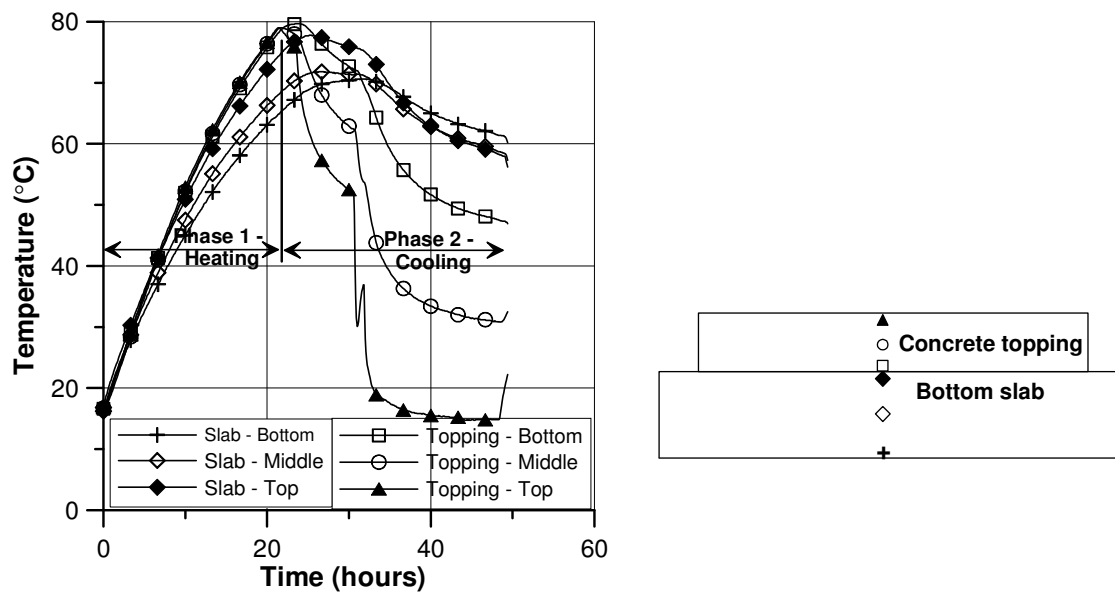


Figure 5 – Development of temperature in time at different positions in the bottom slab and topping of test PC and FRC II:4, i.e. the last test of series II. The temperature distribution was used as a load in the FE-simulations.

In the numerical modelling the temperatures were prescribed as functions of time for each nodal point of the continuum elements. In a stepwise execution DIANA then interpolated the corresponding temperature field for each time point. The so obtained distribution of temperatures was then translated into a thermal strain field using the specified linear coefficient of thermal expansion, α .

3. RESULTS

As was pointed out in the introduction there are some typical modes of failure for the type of structure studied here. In particular, the occurrence of vertical tensile cracks extending through the thickness of a topping as well as shearing along the interface between topping and substrate were identified as such. As a consequence, the most significant results are the relative displacements between toppings and bottom slab in addition to the development of deformations in the concrete along the toppings. Thus, the following presentation primarily focuses on information regarding these matters. Also, for the sake of verification the results obtained in the analysis are compared with results from the experimental study. As a temperature distribution corresponding to the test of series II was prescribed for the simulations, the comparisons were done with these tests, i.e. with results from tests PC II:4 and FRC II:4.

3.1 End displacements

The development of end displacements of the toppings is presented in *Figure 6 (a)* and *(b)* for a complete test cycle, i.e. during heating and cooling. Both the effect of interfacial properties, good and poor bond, as well as the influence of steel fibres on the development of end displacements is illustrated. For comparison reasons the corresponding measurements from the last test of series II, PC II:4 and FRC II:4, are also revealed in the graphs. As in reality, where the floor was used as reference for the readings rather than the slab, the displacements are presented as the movement of the topping relative the floor. Thus, not only the deformation of the topping but also the displacement of the bottom slab is included in the results.

From *Figure 6 (a)* and *(b)* it is clear that there is a rather good correlation between measured and simulated horizontal displacements during the initial phase, even though the simulated specimens translated slightly more than what was measured in reality. This indicates that the temperature load employed in the analysis agreed well with measured temperatures.

On the other hand, considering the vertical displacements during the heating phase there is a rather great discrepancy between predicted and experimental values. On this subject the FE analysis suggests a successive increase in vertical movement up to a value of about 0,15 mm. This is a result of the expansion of the concrete due to the increased temperature rather than displacements of the topping in relation to the slab. In this case the temperature was increased approximately 60 °C according to the temperature recordings, see *Figure 5*. This corresponds

to a vertical expansion of $60 \times 10^{-5} \times 275 = 0,165$ mm, as the gauges were positioned approximately in mid section of the topping ($200 + 75 = 275$ mm).

During the same period practically zero, or at least rather small vertical deformations were registered in the experimental study, which implies that the registered temperatures may not have been representative for the entire set-up.

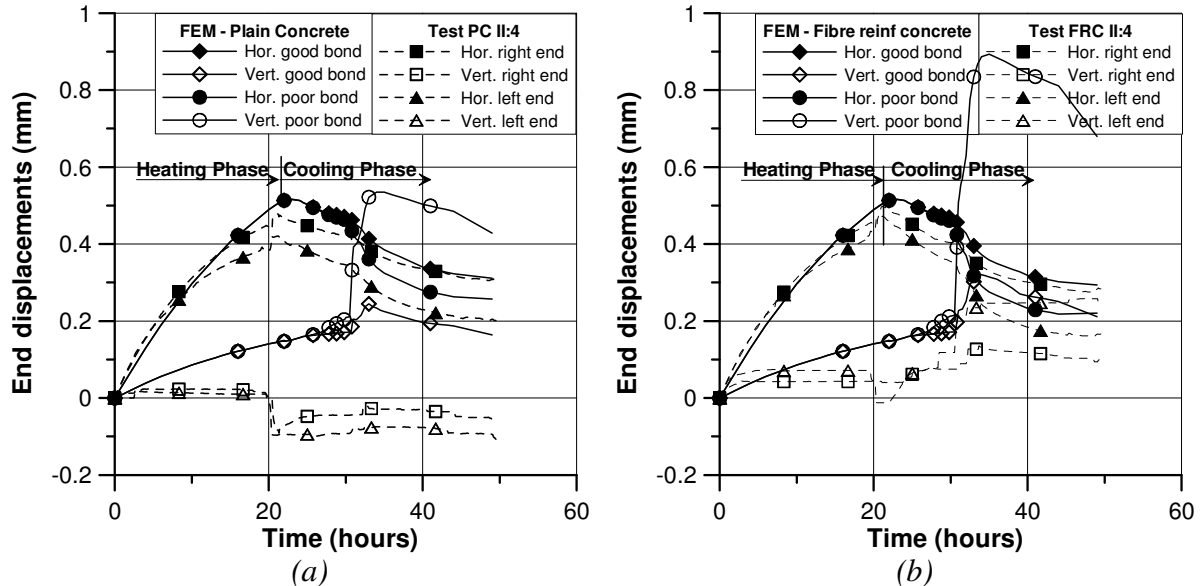


Figure 6 – Development of end displacements during a complete test cycle, i.e. phases 1 and 2 in Figure 1. Both a poor as well as a good bond situation (see *Feil! Ukjent bryterargument.*) have been studied in the FE analysis. Also shown are the corresponding displacements measured for tests PC II:4 and FRC II:4 respectively. Displacements obtained for Plain Concrete (PC) is shown in (a) and for Fibre Reinforced Concrete (FRC) in (b).

The horizontal and vertical end displacements during the cooling phase alone are shown in Figure 7 (a) and (b), i.e. time zero corresponds to the initiation of cooling. Assuming that the bottom slab was rigidly fastened to the floor during this phase, the presented graphs should represent the displacements of the ends of the toppings. However, results from the experimental study showed that the applied forces on the bottom slab, about 20 tons at six positions, were not sufficient to produce 100 % restraint. This is indicated by the horizontal deformations that were generally too great in magnitude to represent only the displacements of the toppings.

Similar results were obtained in the analysis, where the bottom slab continued to deform even during the cooling phase, despite the fact that loads had been applied. This may be seen when studying the displacement of the nodal point at the lower corner of the slab, which is plotted in the diagrams of Figure 7. During the first 10 hours after the load had been applied the slab did not translate horizontally, or at least not contract, even though the toppings contracted slightly. This is due to the fact that the temperature in the slab was kept at a rather high temperature during this period, as may be seen in Figure 5. After this point however, the slab started to contract, up to a maximum of about 0,15 mm, as a consequence of the temperature decrease. Thus, as was also the case in reality, it can be concluded that the loads applied to the slab in the analysis were not sufficient to restrict it from moving as the temperature decreased.

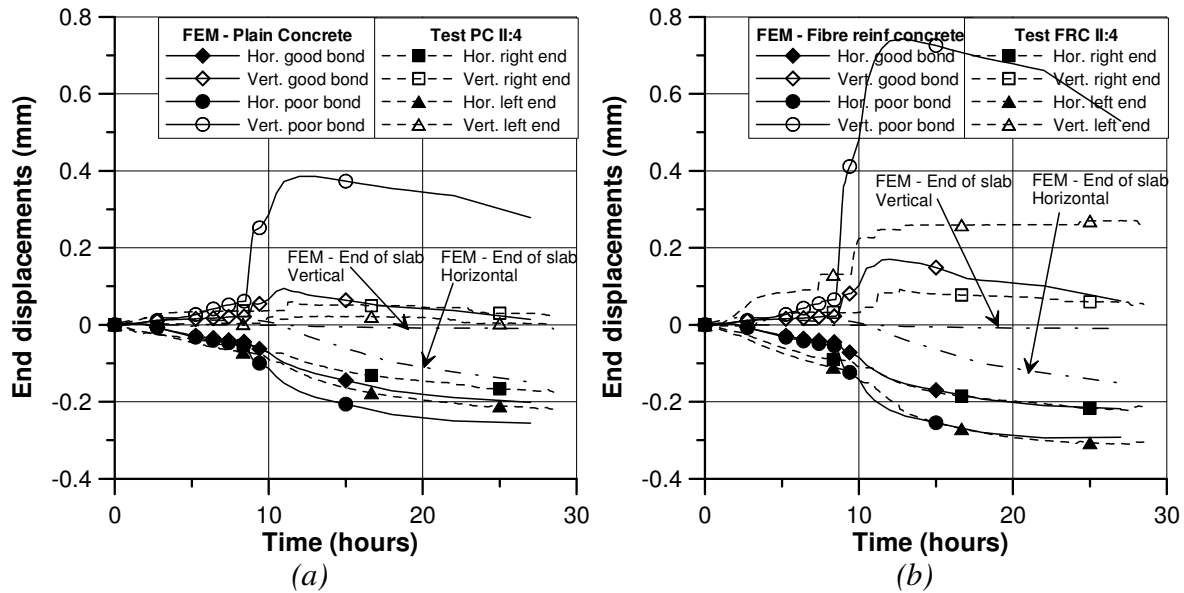


Figure 7 – Development of end displacements during the cooling phase alone for the poor and the good bond situation. Also presented are the corresponding displacements measured for tests PC II:4 and FRC II:4 respectively. Displacements obtained for Plain Concrete (PC) is shown in (a) and for Fibre Reinforced Concrete (FRC) in (b).

When comparing the actual results of the analysis with the experiments, *Figure 7*, it can be seen that there is a rather good agreement between measured and simulated horizontal displacements during the cooling phase, which was also the case during the heating phase. This was particularly true for the FRC topping where the displacement of the left end of FRC II:4 showed good agreement with the poor bond situation in the FE analysis while the translation of the right end coincided with the good bond situation. Even though the good correlation was just a coincidence here it indicates that a more severe de-bonding has occurred at the left end of FRC II:4.

If the magnitude of the vertical displacements, i.e. the edge lifting, is looked upon it can be concluded that the so called good bond situation in the FE analysis better described the actual quality of the interface for the tests. For both the PC as well as for the FRC it is clear that the poor bond situation was too weak.

Also interesting to notice is that not only the interface quality but also the concrete properties seems to have influence on the edge displacements. Regarding this effect the FE analysis suggests that the curling would be somewhat greater in magnitude for the case when FRC properties is assumed. This is possibly a consequence of the redistribution of stresses following from the formation of vertical cracks in the toppings. For plain concrete, a sudden drop in force transferring in the crack zone characterizes the development of a crack. This results in a relaxation of stresses in surrounding parts of the structure. Clearly, for cracks forming within a near distance from a free end this will most certainly have a positive effect on the magnitude of the curling moment in the sense that it will decrease.

On the other hand, when a crack develops in fibre reinforced concrete, forces may still be transferred in the actual fracture zone by fibres that bridge the crack. As a result, the redistribution of stresses following from the formation of fracture zones will be somewhat restricted and the corresponding reduction of the curling moment may be less for fibre reinforced concrete as compared to plain concrete. In other words, the analysis suggests that

the better the post-cracking properties of the concrete the higher demands are put on the bond quality of the interface in order to avoid lifting near free edges.

3.2 Longitudinal strain development

The development of longitudinal strains at the upper faces of the toppings obtained from the FE analysis for a poor bond situation (P.B.) and a good bond situation (G.B.) is presented in *Figure 8 (a)* for PC and in *Figure 8 (b)* for FRC. Also shown are the strains measured with Vibrating Strain Gauges (VSG:s) at the upper faces of tests PC II:4 and FRC II:4. The presented results represent the strain changes during the cooling phase alone, i.e. time zero in the graphs corresponds to the initiation of cooling. For comparison reasons the strains from the FE analysis have been levelled out over deformation intervals of 15 cm, which corresponded to the measuring lengths for the VSG:s.

Negative strains represent the contraction of the un-cracked concrete due to temperature decrease while the strains following from the establishment of crack zones and possible debonding along the interface near the crack are represented by positive values.

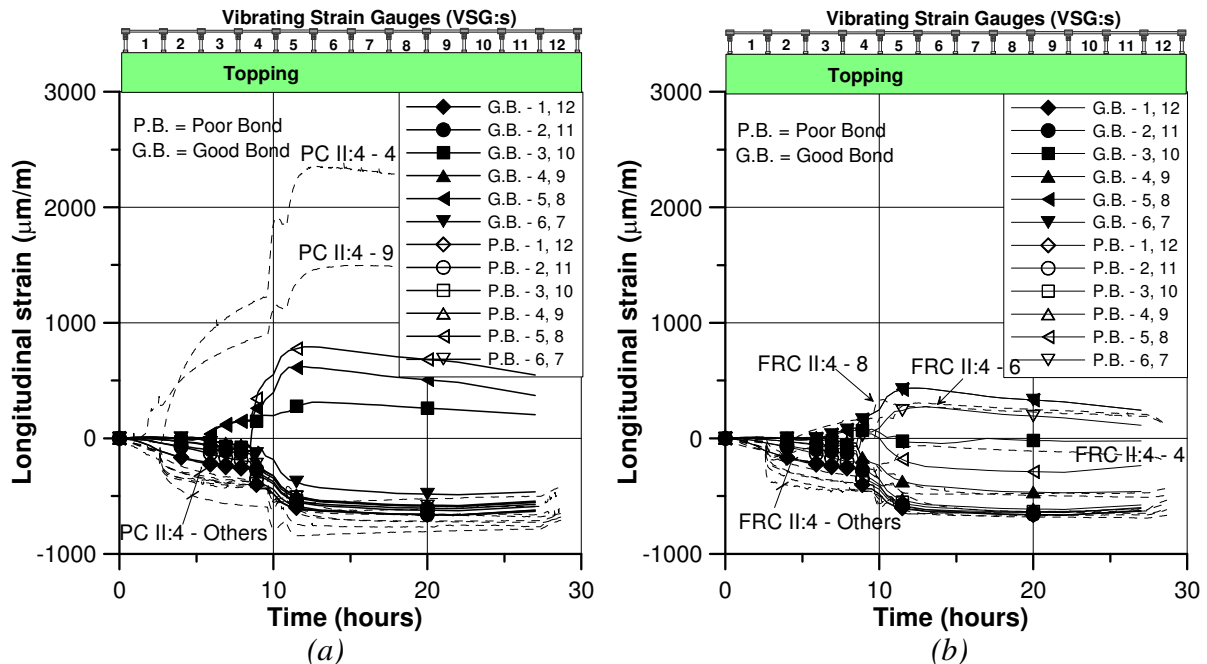


Figure 8 – Development of longitudinal strains during the cooling phase at the upper faces of the toppings obtained from the FE analysis for both a Poor Bond situation (P.B.) as well as a Good Bond situation (G.B.). Also shown are the corresponding strains measured with Vibrating Strain Gauges (VSG:s) at the upper faces of the specimens of test II:4 (dashed lines). PC in (a) and FRC in (b).

Considering the results of the PC, it is evident that cracks in reality, i.e. for PC II:4, appeared at an earlier stage as compared to what the FE analysis gives. Two major cracks, represented by a sudden increase in positive strains, occurred approximately after 2-3 hours at positions 4 and 9 in PC II:4 while cracks did not appear until after 5 hours in the analysis. There may be several reasons for this. One of which could be that there may have been imperfections as regards the concrete properties in the real topping. As cracks tend to form in the weakest parts of a structure this would most likely result in a somewhat earlier crack initiation. Also

possible is that the fastening of the bottom slab to the floor introduced some unintended stresses in the topping that were not anticipated by the FE simulations.

If the results of the FRC specimens are looked upon it can be concluded that the crack development was somewhat different. Unlike the case for the PC the crack zones were established at approximately the same time in the FE analysis as in reality, i.e. for FRC II:4.

3.3 Crack distribution

The maximum distributions of longitudinal strains along the upper faces of the toppings are presented in *Figure 9 (a)-(d)*. Also shown are contour plots obtained from the FE analysis at the corresponding time. In order to improve the legibility of the plots the displacements have been magnified 200 times. The colour scale gives an indication of the distribution of longitudinal stresses in the structure. Here, dark shaded areas represent the peak tensile stresses while a somewhat lower stress is indicated by the lighter colour. (However, the main intention of showing the contour plots is not to provide exact illustrations of the stress distribution but rather to show the overall responses of the simulated toppings).

When studying the results shown in the various graphs it is possible to draw some conclusions regarding both the effect of the interface properties between topping and slab as well as the influence of fibres, or rather the residual tensile strength. On the subject of bond it is clear that poor interfacial properties resulted in substantially greater deformations near free edges as was also discussed previously (compare (a) with (c) and (b) with (d)). From the contour plots it is further evident that this effect was even more pronounced when FRC properties were employed. The fact that the de-bonded zones were considerably greater for the poor bond situation also resulted in fewer cracks (compare (c) and (d) with (a) and (b)) in the analysis.

Regarding the influence of the concrete properties it is clear from the good bond situation that the magnitude of the positive strain peaks, that represent cracks, were slightly smaller for the FRC as compared to the PC (compare (a) with (b)). This is due to the better post cracking tensile properties specified for the FRC. In this case the material characteristics assumed approximately corresponded to the stress versus crack opening displacement relationship obtained for concrete with 30 kg/m^3 of steel fibres (test FRC I:1). For test FRC II:4, however, the amount was 60 kg/m^3 . In other words, it would perhaps be reasonable to assume even better residual strength in the simulations. The reason as to why this was not done here was due to numerical instabilities that became more accentuated as the residual response of the concrete was improved.

Considering the poor bond situation, *Figure 9 (c) and (d)*, it is clear from the contour plot that the distribution of appearing cracks was somewhat different for the FRC as compared to the PC simulation. The reason for this was possibly that the de-bonded areas of the FRC topping were considerably greater as compared to the corresponding PC specimen. Thus, as the de-bonded zones influenced the fractures of these specimens extensively it is not reasonable to draw any conclusions based on these results.

Differences may further be observed when comparing the calculated and measured strain distributions. For the plain concrete it is clear that the recorded crack widths were substantially greater as compared to the results from the numerical modelling. Strain peaks of up to 1400 and 2300 $\mu\text{m/m}$ were recorded for the two appearing cracks of PC II:4 while the

corresponding peak values foreseen in the FE analysis were only about 600 to 800 $\mu\text{m}/\text{m}$. An explanation for this may be that the establishment of the two crack zones in PC II:4 was followed by de-bonding along the interface in the vicinity of the cracks. This was noticed as water leaked through the cracks and came out underneath the topping near the cracks.

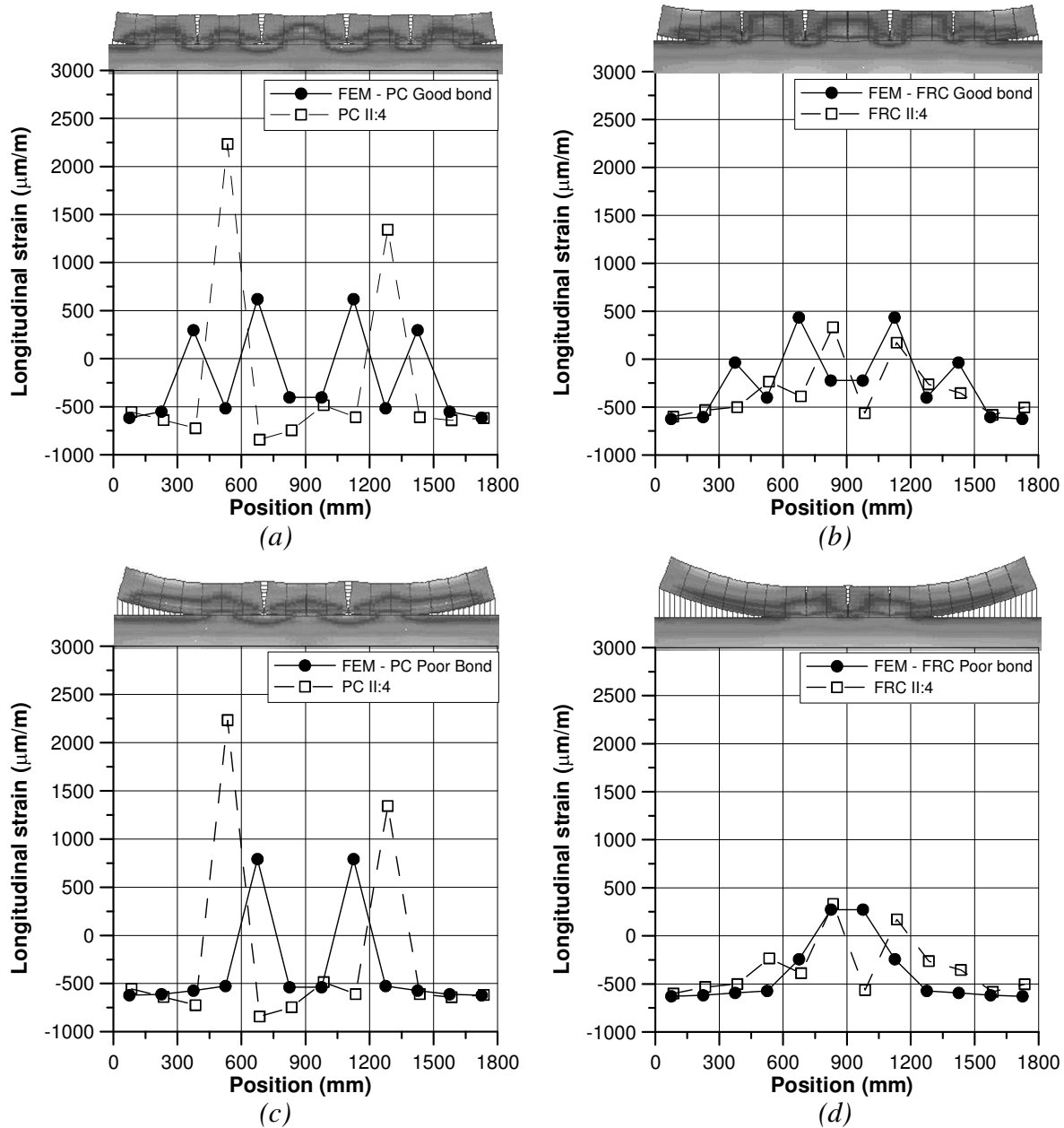


Figure 9 – Maximum longitudinal strain distribution from FEM and experiments, i.e. test II:4, and contour plots from FE-analysis at the corresponding time. PC and FRC with good bond in (a) and (b) respectively and PC and FRC with poor bond in (c) and (d) respectively.

It is also possible to distinguish this effect from the graphs shown in Figure 9 (a) and (c). If the strains near the cracks of PC II:4 are looked upon, in particular the widest one, it can be seen that the contractions are substantially greater than what was estimated by the FE analysis. Directly to the right of the widest crack a minimum strain of about $-800 \mu\text{m}/\text{m}$ was recorded as compared to a calculated value of only about $-500 \mu\text{m}/\text{m}$. This indicates that de-bonding has occurred for PC II:4 in parts located near the crack zones, at least close to the widest one. For the FE simulations, on the other hand, de-bonding did not take place to the

same extent. The reason for this may be that the reactions of the interface elements in vertical and horizontal direction are not connected, i.e. separate elements were employed in each direction. This implies that the vertical displacements, i.e. lifting due to vertical bond failure, is not necessarily followed by horizontal slip, as is normally the case in reality.

4. SUMMARY AND CONCLUSIONS

A non-linear Finite Element Model has been set up to simulate the response of restrained concrete toppings exposed to temperature related deformation. The main ambitions of the analysis were to demonstrate the significance of the interfacial bond between topping and substrate and the softening properties of the concrete as regards the fracture response of such structures. The results from the analysis were also compared to experimental results as described in more detail in *Carlswärd* [2].

On the subject of bond between overlay and substrate, two different situations were studied, poor and good bond. As expected the analysis indicated that a poor bond situation would result in greater end displacements due to de-bonding. A consequence of this was also that fewer cracks developed with somewhat greater widths.

The favourable effects of fibres were accounted for by improving the tension softening response of the concrete. For the properties employed here, which approximately corresponded to a concrete with 30 kg/m^3 of steel fibres, it was shown that somewhat greater end displacements were achieved for the FRC as compared to the PC. This indicates that the demands on the bond quality may increase as the post-cracking properties of the concrete improve.

Regarding the influence of steel fibres on the crack formation it was shown that the predicted crack widths were only slightly reduced due to the use of fibre reinforcement, i.e. for the properties assumed here. It was further shown that the distribution of cracks was rather similar for the PC as compared to the FRC, at least in the case of good bond.

When comparing computed results with experimental it was clear that the correlation was not particularly good, even though it seems as if the model was able to capture the various features of restrained toppings, i.e. edge lifting and cracking. There may be several explanations to this. For instance, there were a number of more or less unknown parameters applied in the analysis, e.g. interface properties, elastic modulus of concrete, friction between slab and floor, coefficient of thermal expansion etc. In addition, it is clear that some of the properties change due to variable temperature. This has not been considered in the analysis either. Moreover, creep effects were not accounted for in the analysis for the reason that visco-elastic behaviour was not an option for the interface elements applied to simulate discrete cracks.

Another possible source of error is that the load situation may have differed despite the fact that the same temperature field was used in the analysis as was measured in the test. This suspicion is based on the fact that there were differences between predicted and measured vertical displacements of the ends of the toppings, which indicates that the measured temperatures may not have been representative for the complete set-up. Also the fact that the real toppings were exposed to the surrounding environment some time before the actual tests were initiated may have influenced the load situation. This means that stresses may have

developed in the toppings in advance as a consequence of differential shrinkage. In the analysis, however, the concrete was unstressed at the initiation of the temperature test.

It is further important to mention that the analysis was rather complicated in the sense that small variations in assumed material parameters often resulted in numerical instabilities. This limited the span within which the different features could be varied.

ACKNOWLEDGEMENTS

The research project is included as a part of the Doctors of Engineering Programme initiated and partly financed by the Scancem Group (now Heidelberger Zement, Northern Europe). Financial support has also been provided by the Swedish Research Council for Engineering Sciences, TFR, and Betongindustri AB.

REFERENCES

1. DIANA, "DIANA release 7 – Finite Element analysis," TNO Building and Construction Research, Division of Engineering Mechanics and Information Technology, 1998.
2. Carlswård, J., "Steel Fibre Reinforced Concrete toppings exposed to temperature deformation – Part I: Experimental study," Nordic Concrete Research, Publication no 28, The Nordic Concrete Federation, 2003.
3. Groth, P., "Fibre Reinforced Concrete – Fracture mechanics methods applied on self-compacting concrete and energetically modified binders," Doctoral Thesis 2000:04, Luleå University of Technology, Division of Structural Engineering. ISSN: 1402-1544. 2000.
4. Elfgren, L., "Fracture Mechanics of Concrete Structures – From theory to applications," *RILEM REPORT*, edited by L. Elfgren, 1989.
5. The concrete handbook - Material, "Betonghandbok – Material," *Svensk Byggtjänst*, Stockholm, (In Swedish), 1994.
6. Dettling, H., "Die Wärmedehnung des Zementsteins, der Gesteine und der Betone," Technische Hochschule Stuttgart, Otto-Graf Institut, Schriftenreihe Heft3, Stuttgart, 1968.
7. Wiegler, H., and Fischer, R., "Betong bei temperaturen von 100 bis 750°C," *Beton*, 1968:2, pp. 33-46.
8. Silfwerbrand, J., "Effekter av differenskrämpning, krypning och fogytans egenskaper på bärförmågan hos samverkansplattor av gammal och pågjuten betong," Meddelande nr 147, (In Swedish), Structural Engineering, Royal Institute of Technology, 1987.

Concrete Structures Subjected to Blast and Fragment Impacts



Joosef Leppänen, Lic. Sc., Research Assistant

E-mail: joosef.leppanen@ste.chalmers.se

Kent Gylltoft, Ph.D., Professor

E-mail: kent.gylltoft@ste.chalmers.se

Department of Structural Engineering, Concrete Structures,
Chalmers University of Technology,
S-412 96 Göteborg, Sweden



ABSTRACT

Concrete structures subjected to explosive loading in a combination of blast and fragment impacts respond very differently from statically loaded structures. A literature study is made with emphasis on gathering the work that deals with blast waves, fragment impacts, dynamic behaviour and damage in concrete structures. The behaviour of concrete exposed to blast and fragment impacts leads to damage in the form of severe cracking as well as spalling. When fragments penetrate concrete deeply, scabbing may occur at the reverse side of a wall, or even perforation, with a risk of injury to people inside the structure.

Key words: concrete, blast waves, fragment impacts, penetration, perforation, dynamic loading.

1. INTRODUCTION

Concrete structures, usually massive, are used for protection, e.g. civil defence shelters. For these shelters, the main threat arises from explosions caused by military weapons, such as conventional and nuclear weapons. A bomb explosion generates a blast wave and fragments fly in all directions. Chalmers University of Technology is collaborating with the Swedish Rescue Services Agency, to study the behaviour of concrete structures subjected to blast loads and fragment impacts; see Johansson [1], Leppänen [2] and Leppänen and Gylltoft [3].

A blast load is characterized by its short-duration. By computations, Johansson [1] showed how a shelter subjected to a blast wave responded at the most critical stage, i.e. the first few milliseconds. If the load was applied fast enough, some parts of the structure were not affected by the loading, while other parts of it had already failed. Furthermore, it was shown that the civil defence shelter could withstand the design load of the blast, according to the Swedish Rescue Services Agency, Shelter Regulations [4].

In addition to the blast wave, the detonation of a General Purpose (GP) bomb causes fragments to fly against the civil defence shelter. In Leppänen [2], the effects of fragment impacts were

studied. To examine what happens when a fragment strikes a concrete structure, there are several factors that must be taken into account. These include fragment impacts and damage mechanisms in concrete, as well as the dynamic behaviour of concrete under high pressures.

The present paper is intended to contribute to improved understanding in the field of concrete structures subjected to explosive loading. Section 2 treats blast waves, reflections, and fragmentation. The behaviour of concrete under dynamic loading is discussed in Section 3, and Section 4 deals with damage to concrete structures.

2. BLAST WAVES, REFLECTIONS AND FRAGMENT IMPACTS

To understand the behaviour of concrete structures subjected to severe loading from military weapons, the nature and physics of explosions and the formation of a blast wave and reflections from a bomb must be understood. When the blast wave hits a concrete surface, a stress wave propagates through the concrete. An explosion is characterized by a physical or chemical change in the explosive material; this happens when there is a sudden change of stored potential energy into mechanical work, which generates a blast wave and a powerful sound, see Engberg and Karevik [5]. The explosive material can react in two ways, as a deflagration or as a detonation. For deflagration, the explosive material burns at a speed below the sonic speed, while for a detonation, the chemical reaction occurs faster than the sonic speed. In military situations, detonations are the most common; for example, if a TNT charge explodes, this means that it decays as a detonation. In this work, explosion is used to designate a detonation, unless otherwise stated.

2.1 Blast waves

A shock wave resulting from an explosive detonation in free air is termed an air-blast shock wave, or simply a blast wave. The blast environment differs according to where the explosion takes place. In an airburst, when the blast wave hits the ground surface, it is reflected. The reflected wave coalesces with the incident wave, forming a Mach front, as shown in Figure 1. The point at which the three shock fronts meet – incident wave, reflected wave and the Mach front – is termed the triple point; this is further discussed in Section 2.2.

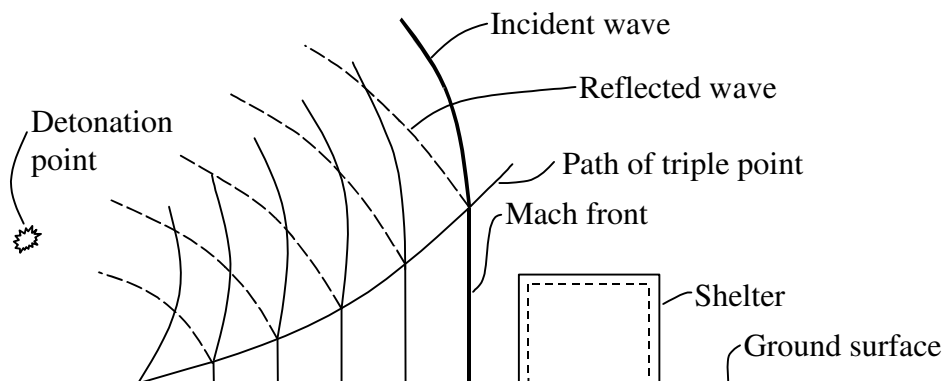


Figure 1 – Blast environment from an airburst, based on Krauthammer [6].

When there is a surface burst, the reflection occurs instantaneously from the ground surface, which generates a shock wave; this is termed a ground-reflected wave, as shown in Figure 2. At a short distance from the burst, the wave front can be approximated by a plane wave.

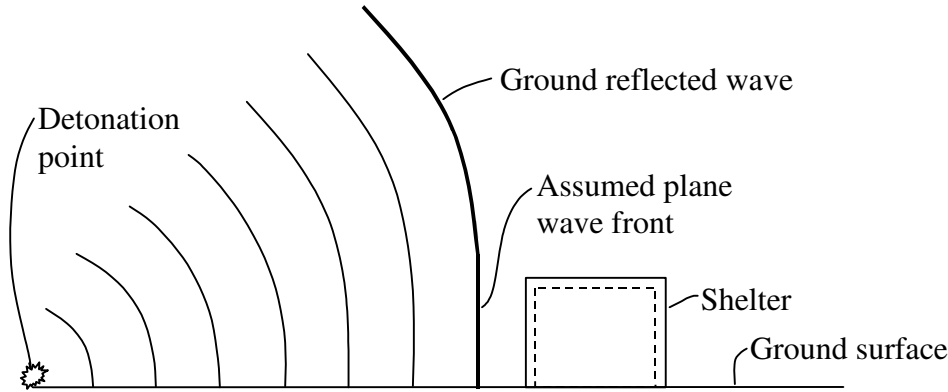


Figure 2 – Surface burst blast environment, based on Krauthammer [6].

The pressure–time history of a blast wave can be illustrated with a general curve as shown in Figure 3. The illustration is an idealization of an explosion. The pressure–time history is divided into positive and negative phases. In the positive phase, maximum overpressure, $p_0 + P_s^+$, rises instantaneously and then decays to atmospheric pressure, p_0 , with time, T^+ . The positive impulse, i^+ , is the area under the positive phase of the pressure–time curve. For the negative phase, the maximum negative pressure, $p_0 - P_s^-$, has a much lower amplitude than the maximum overpressure. The duration of the negative phase, T^- , is much longer than that of the positive one. The negative impulse, i^- , is the area below the negative phase of the pressure–time curve. The positive phase is more interesting in studies of blast wave effects on concrete buildings because of the high amplitude of its overpressure and the concentration of the impulse.

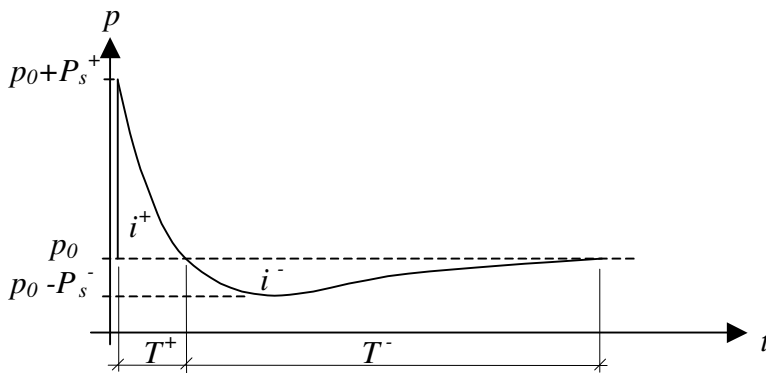


Figure 3 – Pressure–time history from a blast.

The following exponential form expresses the pressure–time history in Figure 3, first noted by Friedlander (1939), according to Bulson [7]:

$$p(t) = p_0 + P_s^+ \left(1 - \frac{t}{T^+}\right) e^{-bt/T^+} \quad (1)$$

where $p(t)$ is the overpressure at time t and T^+ (the positive duration) is the time for the pressure to return to the atmospheric level p_0 . By selecting a value for the constant b various pressure-time histories can be described. The peak pressure $p_0 + P_s^+$ depends mainly on the distance from the charge and the weight of the explosives. In addition, if the peak pressure, the positive impulse and the positive time duration are known, the constant b can be calculated, and then the pressure-time history can be obtained.

Equation (1) is often simplified with a triangular pressure-time curve; see Bulson [7]:

$$p(t) = p_0 + P_s^+ \left(1 - \frac{t}{T^+}\right) \quad (2)$$

Conventional high explosives usually produce different magnitudes of peak pressure. As a result, the environments produced by these chemicals are not the same. To establish a basis for comparison, other explosives are rated according to equivalent TNT values, which can be found in the literature, as in Krauthammer [6], with the pressure range for various chemicals.

A scaling parameter is introduced, first noted by Hopkinson (1915); see Bulson [7]. With the parameter Z it is possible to calculate the effect of a detonated explosion, conventional or nuclear, as long as the equivalent weight of charge in TNT is known:

$$Z = \frac{R}{W^{1/3}} \quad (3)$$

where R is the distance from the detonation and W is the equivalent weight of TNT. The peak pressure, the positive duration time and the positive impulse are now functions of Z , and the pressure-time history in Figure 3 can be described:

$$\begin{aligned} P_s^+(Z) \\ \frac{T^+}{\sqrt[3]{W}}(Z) \\ \frac{i^+}{\sqrt[3]{W}}(Z) \end{aligned} \quad (4a-c)$$

In the literature there are several empirical formulas for the expressions in equations (4a-c); see Bulson [7]. In a US Army technical manual [8], there are tables and diagrams for a range of about twenty explosive materials.

2.2 Blast wave reflections

When a blast wave strikes a surface which is not parallel to its direction of propagation, a reflection of the blast wave is generated. The reflection can be either normal or oblique. There are two types of oblique reflection, either regular or Mach; the type of reflection depends on the incident angle and shock strength.

Normal reflection

A normal reflection takes place when the blast wave strikes perpendicular to a surface, as shown in Figure 4. The medium (normally air) has a particle velocity U_x before the incident shock wave U_s passes through the medium; after passage the particle velocity increases to U_p . Furthermore, the overpressure increases from p_x to p_y (p_x usually refers to atmospheric overpressure), the temperature rises from θ_x to θ_y and the sonic speed rises from a_x to a_y (a_x is approximately 340 m/s in undisturbed air).

When the blast wave hits a rigid surface, the direction is abruptly shifted, and, as a consequence, the particles at the surface possess a velocity relative to those further from the surface: this relative velocity is equal in magnitude and reversed in direction from the original particle velocity. This has the effect of a new shock front moving back through the air: the reflected shock U_r . However, since the air conditions have changed, the reflected shock does not have the same properties. The reflected overpressure increases to p_r , temperature rises to θ_r and sonic speed is a_r .

For shock waves it is common to describe the velocity as a Mach number, which is defined as the actual velocity (of the shock front) in the medium, divided by the sonic speed of the undisturbed medium. For example, the shock front has a velocity, with a Mach number, M_r , through air that had a velocity of M_x when the incident shock occurred, as shown in Figure 4.

Incident shock at M_x Reflected shock at M_r

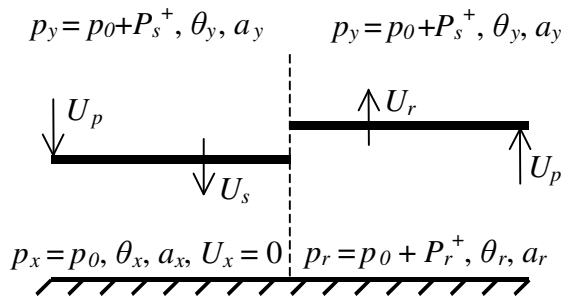


Figure 4 – Normal reflection in air from a rigid wall, based on Baker [9].

The properties of the reflected blast wave can be described in terms of a reflection coefficient, defined as the ratio of reflected overpressure to the overpressure in the incident blast wave. It can be shown that for an ideal gas, with a specific gas constant ratio of 1.4, the reflection coefficient A is, according to Baker [9],

$$A = \frac{p_r - p_x}{p_y - p_x} = \frac{8M_x^2 + 4}{M_x^2 + 5}. \quad (5)$$

From equation (5) it can be seen that for a shock front moving with M_x equal to one, i.e. at sonic speed, the reflection coefficient is two. This means that the overpressure is doubled in the reflected blast wave. As the speed of the shock front M_x rises, the reflection coefficient approaches eight. However, this applies to ideal gas with a specific gas constant ratio of 1.4. In a

real blast wave, the specific gas constant ratio is not constant, and the coefficient is pressure-dependent, see Johansson [10]. The reflection coefficient rises with increasing pressure.

Regular reflection

In a regular reflection, the blast wave has an incident shock at M_x with an angle of β , and reflection takes place. The reflected shock at M_r has an angle of δ as shown in Figure 5. The angle of reflection is not usually equal to the angle of incidence. The air conditions in front of the incident shock (Region 1) are still at pressure p_x and temperature θ_x . Behind the incident shock (Region 2), the air is the same as for open-air shock, with pressure p_y and temperature θ_y . The air conditions from the reflected shock (Region 3), have pressure p_r and temperature θ_r .

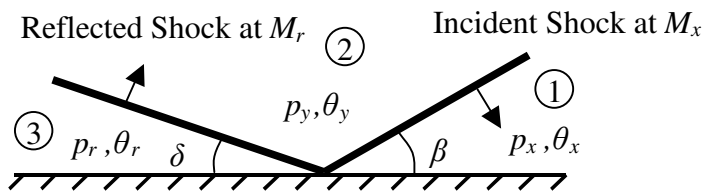


Figure 5 – Oblique reflection, based on Baker [9].

Mach stem formation

There is a critical angle, related to the shock strength, at which there cannot be an oblique reflection. According to Baker [9], Ernst Mach [Mach and Sommer (1877)] showed that the incident shock and the reflected shock coalesce to form a third shock front. This third shock front, termed the Mach stem or Mach front, moves approximately parallel to the ground surface, as shown in Figure 6, as the shock front rises. The point at which the three shock fronts meet is termed the triple point. The Mach front and the path of the triple point are also shown in Figure 1.

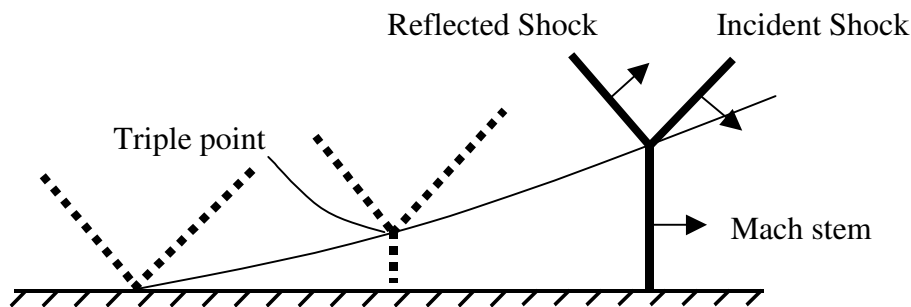


Figure 6 – Mach stem formation, based on Baker [9]. The arrows indicate the directions of the shock waves.

2.3 Fragment impacts

When high explosives such as grenades, bombs, torpedoes, missiles or robots detonate, fragments fly out in all directions when the casing is broken. The fragments from the same kind of weapon can be of different sizes. The damage to concrete depends on the properties of the

fragments, i.e. the striking velocity, mass and area density [kg/m^2]. In the literature there are empirical formulas, such as the ones proposed by Engberg and Karevik [5], Krauthammer [6], ConWep [11] or Janzon [12], for estimating the velocity of the fragments.

The initial velocity of the fragments is determined by the amount of explosive material and size of the casing, which can be estimated with an equation, where Q is the charge weight [kg] and M_h is the weight of the casing [kg], see Engberg and Karevik [5]:

$$v_i = 2400(1 - e^{-2Q/M_h}) \quad [m/s]. \quad (6)$$

The fragment velocity is retarded in the air, depending on the initial fragment velocity, the fragment mass and the type of fragment. The velocity is retarded differently after a distance r , and for steel fragments can be calculated as, see Janzon [12]:

$$v_r = v_i e^{-0.00456r/\sqrt[3]{m_f}} \quad [m/s] \quad (7)$$

where r is the distance [m], v_i is the initial fragment velocity from equation (6) and m_f is the fragment mass [kg]. Fragments from an explosion can fly through the air over very long distances, more than 1000 m for heavy fragments, see Engberg and Karevik [5].

According to Swedish Rescue Services Agency [4], a shelter must be able to resist the effect of a 250 kg GP bomb (with 50 weight per cent TNT) that bursts freely outside at a distance of 5 m from the shelter. The masses of fragments from a 250 kg GP bomb are normally distributed from 1 to 50 gram, see Engberg and Karevik [5]. When using equations (6) and (7), the impact velocity at a distance of 5 m varies between 1650 and 1950 m/s for fragments with mass of 1 to 50 gram. The velocities of fragments from a 250 kg GP bomb are shown in Figure 7 for six fragment weights, ranging from 5 to 400 gram.

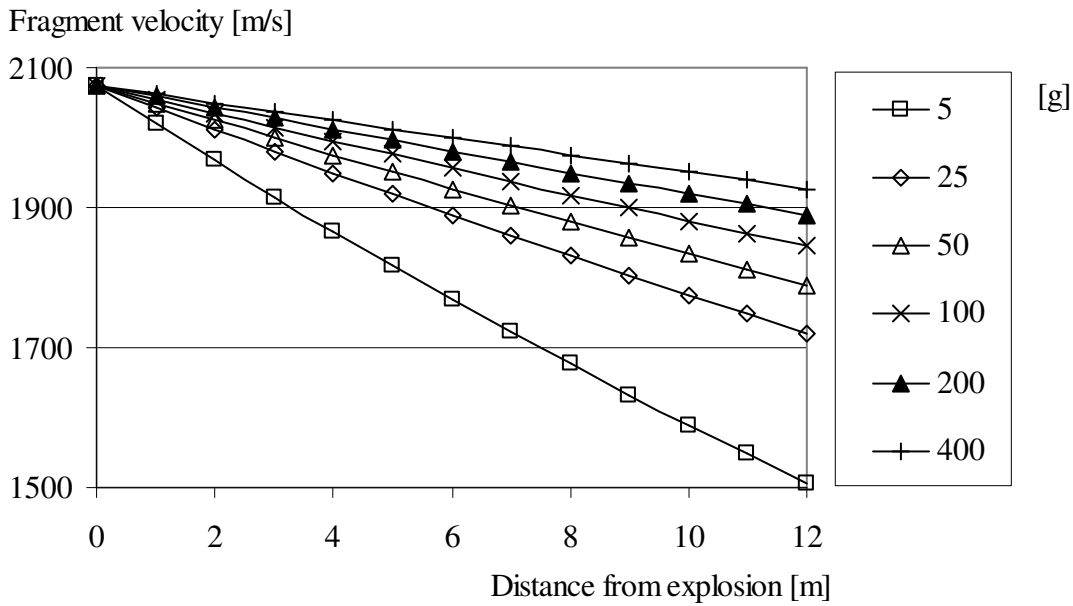


Figure 7 – Fragment velocity from a 250 kg GP bomb (with 50 weight per cent TNT) that bursts freely outside, for fragment weights from 5 to 400 gram, based on equations from Engberg and Karevik [5].

3 BEHAVIOUR OF CONCRETE UNDER DYNAMIC LOADING

3.1 Comparing dynamic and static loading

The behaviour of concrete differs for dynamic loading and static loading. For dynamic loading, the initial stiffness as well the ultimate strength increases, in both compression and tension. Furthermore, the concrete strain capacity is extended in dynamic loading.

At Delft University, Zielinski [13] followed a phenomenological approach when he compared static and impact tensions. He observed a changing geometry of the fracture plane. With increasing loading rate, the amount of aggregate fracture became greater. Furthermore, multiple fractures were observed at high loading rates, as shown in Figure 8. These fracture mechanisms have a direct influence upon the stress-strain relationship for concrete in dynamic loading; the energy absorption is much higher for the multiple fracture planes. Moreover, the stiffness is increased; stress levels at failure for high loading rates and deformation capacity are higher. In addition, the elastic stiffness is increased. This is schematically shown in Figure 9.

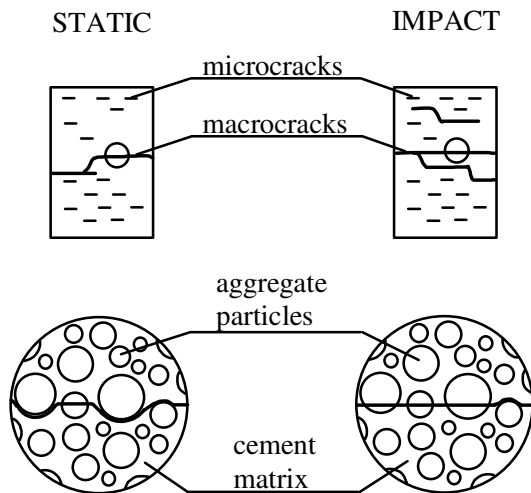


Figure 8 – Crack path for tensile static and dynamic loading; based on Zielinski [13].

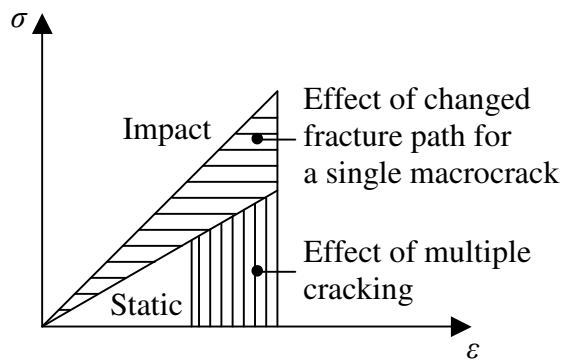


Figure 9 – Schematic view of the effect of fracture mechanisms on the stress - strain relationship, based on Zielinski [13].

3.2 Behaviour of concrete under static loading

Concrete is often characterized with the uniaxial stress-strain relationship as shown in Figure 10. Concrete is weak in tension; for normal-strength concrete, the ultimate tensile strength is less than one tenth of the ultimate compressive strength. However, real structures are subjected to multiaxial stresses. Richart *et al.* [14] observed that confined concrete has greater strength and stiffness, and furthermore, strains are extended. In Figure 11 the stress-strain relationship for concrete in compression is shown for increasing lateral pressure (confined concrete).

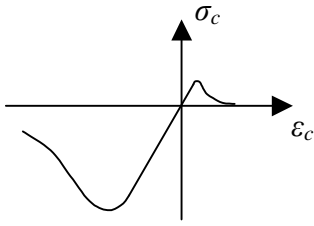


Figure 10 – Concrete stress-strain relationship under uniaxial loading.

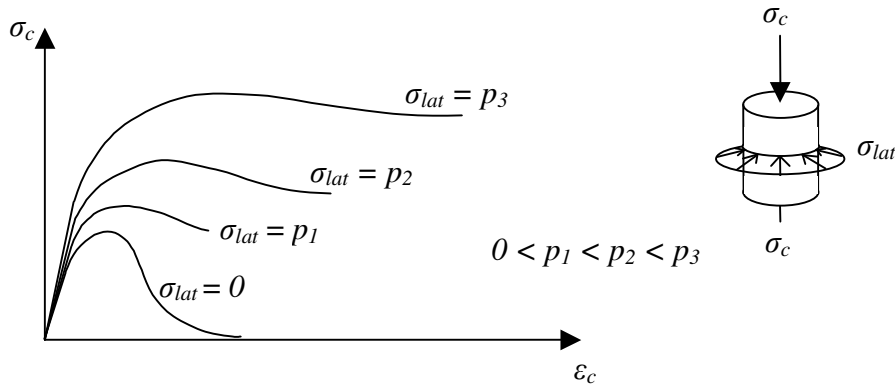


Figure 11 – Schematic view of stress-strain relationship for rising lateral pressure in compressed concrete. Based on research by Richart *et al.* [14].

When concrete is subjected to extremely high pressures, as in an impact situation, the lateral pressure suddenly becomes much higher. During fragment impacts, concrete is exposed to enormous confining pressures and behaves plastically, dissipating a large amount of energy. In addition, civil defence shelters have heavy reinforcement, which provides further confinement effects. The confining pressure in impact loading can be several hundred MPa. In a standard static triaxial test, the ultimate strength of concrete can increase enormously. Experiments by Bažant *et al.* [15], with a uniaxial compressive strength of 46 MPa, showed that the ultimate strength increased up to 800 MPa, and the strains were extended as shown in Figure 12.

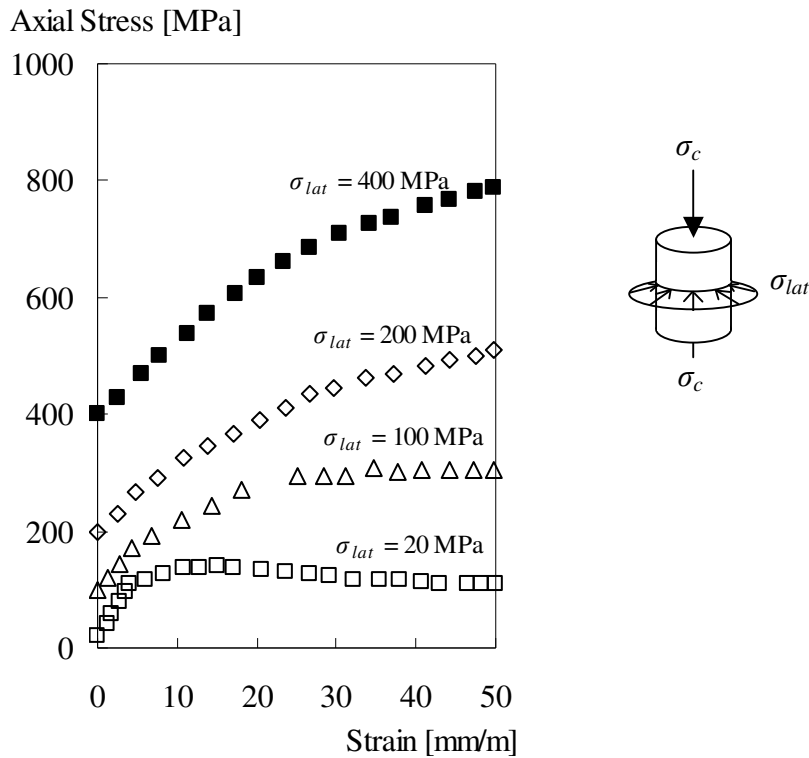


Figure 12 – Stress-strain relationship for confined concrete, based on triaxial compression test data from Bažant et al. [15].

If concrete is subjected to hydrostatic pressure ($\sigma_1 = \sigma_2 = \sigma_3$), the relationship between hydrostatic pressure (mean value of the stress components σ_1 , σ_2 and σ_3) and density becomes non-linear at a certain pressure level. Initially, for low-pressure levels the relationship is linear (elastic loading). With further loading, micro cracking occurs in concrete. Since concrete is porous, the pores collapse and the material is compacted. At a very high-pressure level, all of the pores are collapsed, and the relationship between hydrostatic pressure and density becomes linear again. The equation of state (*EOS*) relates the pressure to the local density and the local specific internal energy. In Figure 13 the equation of state is illustrated for concrete. The initial density is noted as $\rho_{initial}$ and the solid density is noted as ρ_s which is defined as the density at zero pressure of the fully compacted solid. The phase when the material is compacting is the plastic compaction phase.

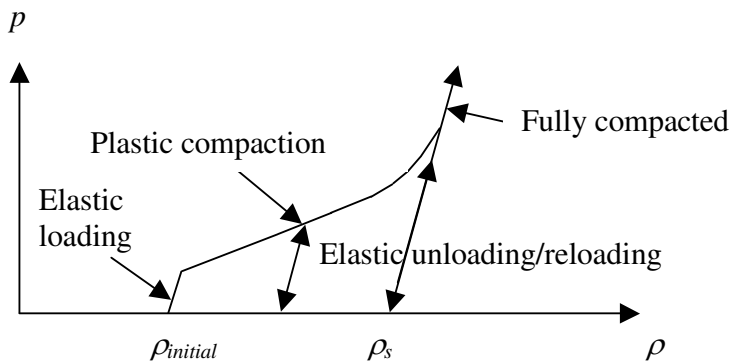


Figure 13 – Equation of state for concrete. Based on AUTODYN Manuals [16].

3.3 Strain rate effects for concrete under uniaxial loading

The behaviour of concrete is determined by the loading rate; this is called the strain rate effect. The strain rate in the material depends on the type of loading, as shown in Figure 14 for five kinds of loading such as creep, static, earthquake, hard impact and blast loads.

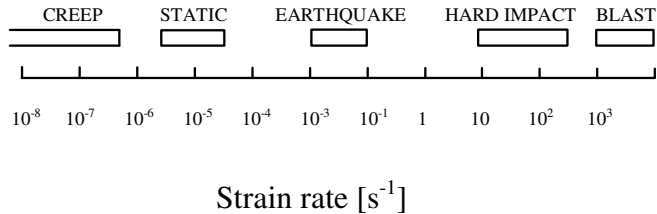


Figure 14 – Strain rates on different loading cases; based on Bischoff and Perry [17].

The strength, deformation capacity, and fracture energy are important parameters for characterizing and describing the response of concrete. For dynamic loading, these parameters are not the same as for static loading. When concrete is subjected to impact loading, the material strength becomes greater. The dynamic increase factor (*DIF*) is the proportional rise of the dynamic ultimate strength relative to the static ultimate strength. According to CEB-FIB Model Code 1990 [18] the *DIF* dependence on strain rate can be described as shown in Figure 15.

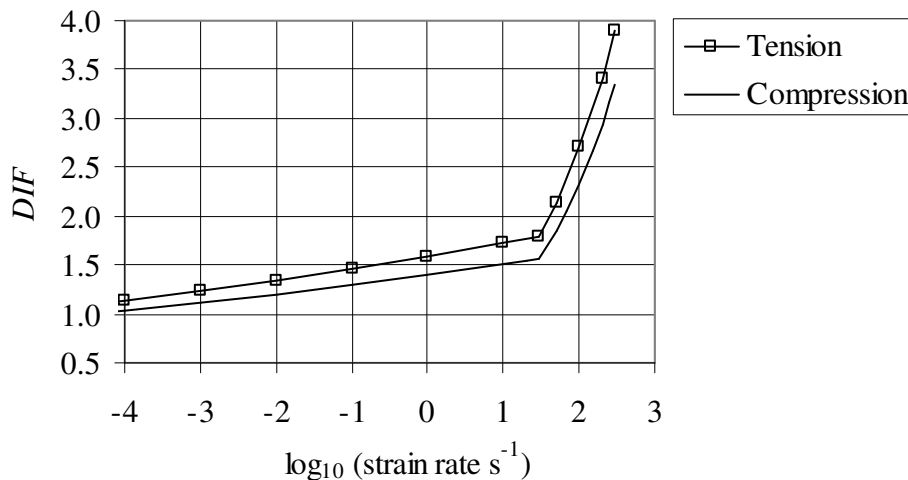


Figure 15 – *DIF* according to CEB-FIB Model Code 1990 [18].

For dynamic loading, the ultimate compressive strength can be more than doubled, see Bischoff and Perry [17]. Moreover, according to Ross *et al.* [19], the concrete ultimate uniaxial strength in tension increases by multiples of 5 to 7 at very high strain rates. The greater strength is explained by the change in the fracture plane. At a higher loading rate, concrete is subject to multiple fractures, and the amount of aggregate fracture increases, see Figure 8. Other explanations of the increased strength are the viscous effects and the forces of the inertia.

The viscous effects are explained by the following. When concrete is subjected to compressive loading, the pores in the concrete, which are filled with water, tend to close. Due to the viscosity

of the water, an inner pressure is developed in the pores. As a consequence, the strength of the material becomes greater. For concrete in tension, the resistance force is generated when the pores that are filled with water are opening. The *DIF* curve has a flat part and a steep part as shown in Figure 15. For concrete in tension, when the strain rate is less than approximately 1 s^{-1} , the viscous effects dominate (flat part), and when the strain rate exceeds approximately 10 s^{-1} , the forces of inertia dominate (steep part). When concrete is compressed, the forces of inertia dominate at strain rates of approximately $60\text{-}80 \text{ s}^{-1}$, see Ross *et al.* [19].

4 DAMAGE ON CONCRETE STRUCTURES

4.1 Introduction

During extreme loading, a concrete structure shakes and vibrates, severe crushing of concrete occurs and a crater forms (spalling) at the contact point; for deep penetration, scabbing may occur at inside of the wall, or even perforation, with a risk of injury for people inside the structure. Fragments are released from the bomb casing, and fly against the structure. The fragment size, area density [kg/m^2] and striking (impact) velocity are important parameters for the fracture mechanism in concrete. Prediction of the depth of penetration is a crucial factor for design of protective structures.

4.2 Penetration of steel fragments into different kinds of materials

The depth of penetration is determined by the fragment mass, form, velocity and inclination angle of impact, and the material of the target. For spherical fragments, it has been empirically found by Janzon [12] that the minimum velocity needed for perforation at different thicknesses of steel plates is

$$v_p = \frac{d}{C \times m_f^{1/3} \times \sin \alpha} \quad [\text{m/s}] \quad (8)$$

where C is a constant that takes into account the form of the fragment and the target material. The inclination of the impact is α , the mass of the fragments is m_f [kg], and the thickness of the steel plate is d [m]. An example of penetration into soft steel by fragments from a 155 mm bursting shell is shown in Figure 16, with an impact inclination of 90° . The approximate depth of penetration into materials other than steel is given by multiples of the depth of penetration for soft steel by using a factor; the factors are given in Table 1.

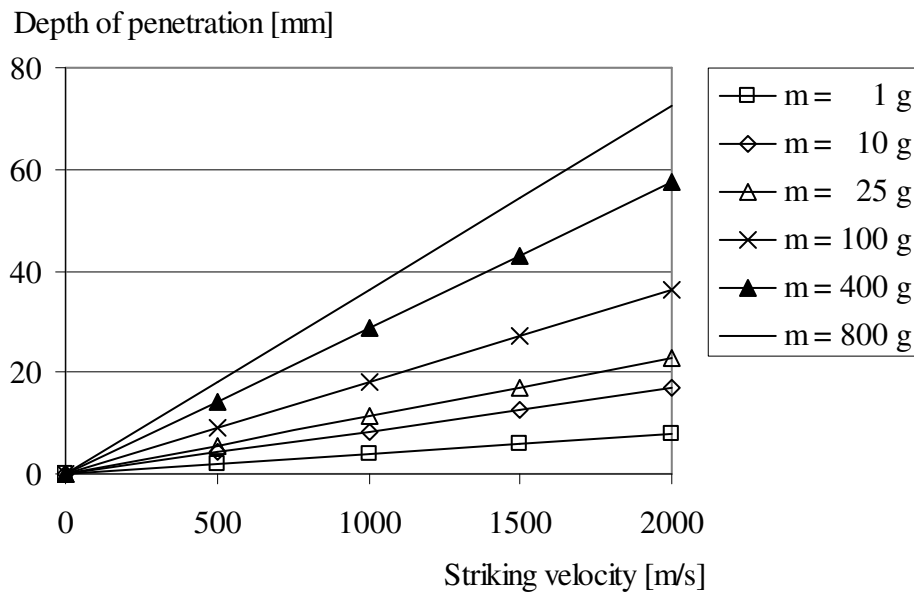


Figure 16 – Depth of penetration into steel, from equation (8), impact inclination 90° , $\theta = 39 \times 10^{-6}$, see Janzon [12].

Table 1 – Penetration depth of common materials, Engberg and Karevik [5].

Material	Factor
Armour-plate	0.75
Soft steel	1.0
Aluminium	2
Reinforced fibre-glass plastic	4
Concrete (K40, reinforced)	6
Pine wood	15
Sand	18
Water	50
Wet snow	70
Dry snow	140

By using a direct formula, from ConWep [11], the depth of penetration, x (in inches) can be estimated for fragments penetrating massive concrete:

$$x = \frac{0.95m_f^{0.37}V_s^{0.9}}{f_c^{0.25}} \quad \text{for } x \leq 1.4m_f^{1/3} \quad (9)$$

or

$$x = \frac{0.464m_f^{0.4}V_s^{1.8}}{f_c^{0.5}} + 0.487m_f^{1/3} \quad \text{for } x > 1.4m_f^{1/3} \quad (10)$$

where m_f is fragment weight [oz.], V_s is the fragment striking velocity [kfps] and f_c is the concrete compressive strength [ksi]. By using conversion factors, as shown in Table 2, the penetration depth of fragments can be calculated in SI-units.

Table 2 – Conversion factors: Inch-pound to SI-units (metric), according to ACI Manual of Concrete Practice 2002 [20].

To convert from	to	multiply by
inch	millimeter [mm]	25.4
foot	meter [m]	0.3048
kip-force/square inch [ksi]	megapascal [MPa]	6.895
ounce-mass [oz]	gram [g]	28.34

The penetration depth of fragments into massive concrete is shown in Figure 17. The depth of penetration is a function of the fragment weight, the striking velocity and the concrete compressive strength. However, it should be noted that for a concrete structure, when there is 70 % penetration, perforation may be expected; see Krauthammer [6].

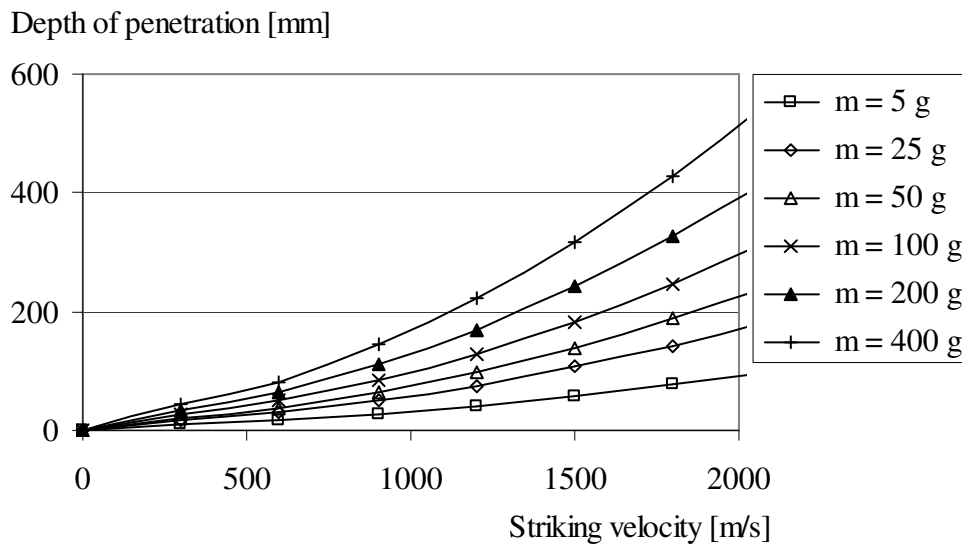


Figure 17 – Penetration of fragments into massive concrete, compressive strength 30 MPa, for fragment weights from 5 to 400 gram with striking velocities up to 2000 m/s, based on equations from ConWep [11].

According to Swedish Rescue Services Agency shelter regulations [4], shelter above ground must have a minimum thickness of 350 mm. For the normally distributed (1–50 gram) fragments from a 250 kg GP bomb with 125 kg TNT, perforation would not be a problem. However, if single fragments of larger size than approximately 100 gram are released from the bomb, at a distance of 5 meters, perforation may occur anyway.

Table 3 shows the thickness required for a concrete wall that just prevents perforation by fragment weights from 5 to 400 gram with striking velocities up to 3000 m/s. As shown, both the striking velocity and the mass are vital factors in the design of protective structures. The area marked grey indicates a thickness above 350 mm massive concrete (the required minimum thickness of a civil defence shelter above ground). The thickness of a concrete wall that just prevents perforation, d_{pf} , can be estimated with the following equation, from Krauthammer [6]:

$$d_{pf} = 1.09xm_f^{0.033} + 0.91m_f^{0.33} \quad \text{inches} \quad (11)$$

where x is the depth of penetration from equations (9) and (10), and m_f is the fragment weight in ounce-mass [oz]. To convert to SI-units, see Table 2.

Table 3 – Thickness of concrete wall that just prevents perforation, compressive strength 30 MPa, for fragment weights from 5 to 400 gram with striking velocities up to 3000 m/s, based on equations from Krauthammer [6].

Striking velocity [m/s]	Fragment mass [g]					
	5	25	50	100	200	400
300	22	39	50	65	84	108
600	30	54	70	91	118	153
900	39	74	97	127	167	220
1200	53	101	134	177	235	312
1500	70	135	180	239	318	424
1800	90	175	233	312	416	556
2100	112	220	295	394	528	707
2400	138	271	363	487	653	877
2700	166	327	439	590	792	1064
3000	196	389	522	702	943	1268

4.3 Spalling and scabbing

A fragment or projectile impact causes severe cracking and crushing in the concrete, which must be supported by reinforcement to prevent failure. When a fragment or a projectile strikes a concrete structure, it penetrates into the concrete and the impact causes crushing of the material at the point of contact (spalling) and possible scabbing on the reverse side of the wall, see Figure 18. When 50 % penetration is achieved, scabbing may become a problem, see

Krauthammer [6]. When a stress wave propagates through the concrete and reaches the inside of a structure, it will reflect as a tensile wave; as concrete is weak in tension, this leads to scabbing at the inside. The amount of reinforcement is a highly critical parameter in regard to scabbing. Experiments show that the scabbing is reduced by increasing the amount of reinforcement since the reinforcement holds the concrete in place (confinement effect), see Jonasson [21].

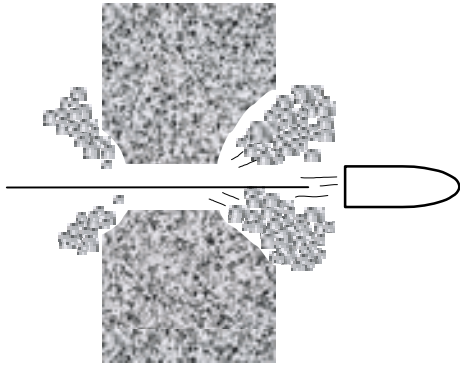


Figure 18 – Spalling and scabbing. Spalling on the exposed side of the concrete wall and scabbing on the reverse side of the wall. Based on Engberg and Karevik [5].

4.4 Combined blast wave and fragment impact loading

A building is exposed not only to fragments or only a blast wave: the loading from a bomb is a combination of both the blast wave and flying fragments. Experiments show that a concrete building which is exposed to a combination of blast wave and fragments collapses more easily than one exposed only to a blast wave or to fragments, see Forsén and Edin [22]. The load from a detonation can be separated into a blast wave and a stress wave which is caused by the direct impact of the fragments. Depending on the charge and the distance between the bomb and the target, the fragments may strike the concrete surface before, at the same time as, or after the blast wave. Figure 19 shows an example of a 250 kg GP bomb (with an equivalent charge weight of 125 kg) to compare the arrival time of the blast wave calculated according to ConWep [11] and the arrival time of the fragments, yielded by equation (7). For this type of bomb, the arrival times for the blast and the fragments coincide at a distance of approximately 5 m; at a greater distance, the fragments strike the target before the blast wave.

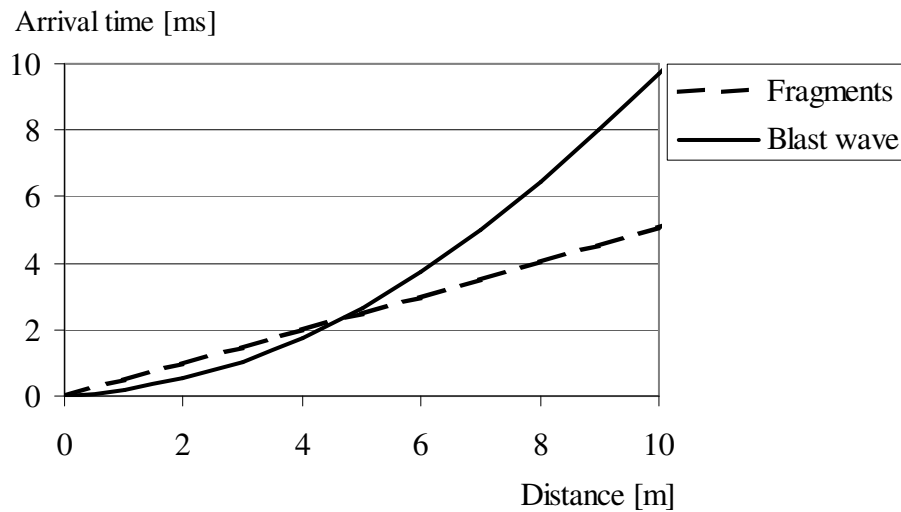


Figure 19 – Calculated arrival time for a blast wave and fragments from a 250 kg GP bomb.

The difference in arrival time for a blast and fragments is less important for short distances, see Forsén and Nordström [23]. This is due to the fact that the response time of a reinforced concrete wall is usually much longer than the difference between the arrival times of a blast and the fragments. The wall is going to be damaged by the fragments before it is deformed. A very good estimation of the deflection can be made by simply superposing the impulse of the fragment impacts on the positive impulse of the blast wave, at the maximum blast pressure. Then the impulse can be simplified and estimated with a triangular shape; and the resistance of the wall can be assumed to be reduced by the fragments, which comprise in the very beginning of the load, see Forsén and Nordström [23].

However, as the impulse of the fragment impacts is relatively small compared with the impulse from the blast wave, the greater damage of the structure caused by the combined blast and fragment impacts remains unexplained. The damage mechanisms are not known in detail. A possible explanation is that when a fragment strikes a concrete wall, the wall accelerates both horizontally and vertically; at same time as the blast wave hits the wall, the wall is suddenly displaced and any mass above accelerates, which increases the normal vertical force of the wall. By taking into account the accelerating mass and the reduced cross section caused by the fragments, the combination of blast and fragment impacts increases the risk of structural collapse.

A detonation inside a building causes more damage than one outside the building. The reason for this is that, in addition to the short duration of a blast wave, there is a long-duration wave added by gas and heat from the explosion, which cannot escape from the limited space. If the amplitude and the duration of the pressure are great enough, the walls and roof may be jerked apart. An important parameter for buildings is the relationship between openings, known as the leakage area. With large leakage areas, the duration of the blast wave can be shortened and the damage possibly reduced.

5 CONCLUSIONS

The load generated by an explosion is characterized by a very short-duration with high pressure. When a bomb detonates, a blast wave and fragments from the bomb casing strike the target. The blast environment (pressure-level) differs depending on where the explosion takes place. During extreme loading the structure shakes and vibrates, severe crushing of concrete occurs and craters forms (spalling) in the exposed side of a concrete wall; for deep penetration, scabbing may occur at the inside of the wall, or even perforation, with a risk of injury for people inside the structure.

For the design of protective structures, their penetration by fragments is an important issue; traditionally, empirical equations are used to predict the depth of penetration. In the literature there are empirical equations to predict the depth of penetration for fragments that strike concrete targets. Although the empirical equations give a good prediction of the depth of penetration, they do not describe fracture mechanisms and the structural behaviour of a concrete building.

For deeper understanding there is need for more research in the field of concrete structures subjected to blast and fragment impacts. Traditionally, experiments in this field are in large-scale; for example, walls, slabs or even whole structures. And often, there is a lack of discussion of the behaviour of concrete for dynamic loading. For gain further knowledge, small-scale experiments combined with numerical methods have been started at Chalmers University of Technology, where the material fracture mechanisms will be studied in detail.

6 ACKNOWLEDGEMENTS

This research project was financed by the Swedish Rescue Services Agency. The authors wish to thank the reference group members of the project, "Dynamic behaviour of concrete structures subjected to blast and fragments": Björn Ekengren, M.Sc., the Swedish Rescue Services Agency, Mario Plos, Ph.D., Chalmers University of Technology, and Morgan Johansson, Ph.D., Reinertsen AB.

7 REFERENCES

1. Johansson, M., "Structural Behaviour in Concrete Frame Corners of Civil Defence Shelters, Non-linear Finite Element Analyses and Experiments", Doctoral Thesis, Department of Structural Engineering, Concrete Structures, Chalmers University of Technology, Göteborg, Sweden, 2000, 204 pp.
2. Leppänen, J., "Dynamic Behaviour of Concrete Structures subjected to Blast and Fragment Impacts", Licentiate Thesis, Department of Structural Engineering, Concrete Structures, Chalmers University of Technology, Göteborg, 2002, 71 pp.
3. Leppänen, J. and Gylltoft, K., "Numerical simulation of concrete penetration with a steel projectile", *XVIII Symposium on Nordic Concrete Research*, Elsinore, Denmark, 2002, pp. 273-275.
4. Swedish Rescue Services Agency, "Skyddsrumregler SR - Produktion och vidmakthållande, (Shelter Regulations - Production and Maintenance. In Swedish)", Publication B54-141/98, Karlstad, Sweden, 1998.

5. Engberg, T. and Karevik, S., "FortH1, Fortifikationshandbok del 1, Kapitel 1-3 (In Swedish)", Försvarets läromedelscentral (FLC), Stockholm, Sweden, 1987, 50 pp.
6. Krauthammer, T., "Modern Protective Structures, Design, Analysis and Evaluation", Course notes, Pennsylvania State University, State College, PA, 2000, 358 pp.
7. Bulson, P.S., "Explosive loading of engineering structures", E & FN Spon, London, 1997, 233 pp.
8. "US Army Fundamentals of Protective Design (Non-nuclear)", Department of Army Technical Manual TM5-855-1, Washington, D.C., 1965.
9. Baker, W.E., "Explosions in Air", Univ. of Texas Press, Austin, TX, 1973, 268 pp.
10. Johansson, M., "Stötvågsutbredning i luft (in Swedish)", Publication B54-223/02, Swedish Rescue Service Agency, Karlstad, Sweden, 2002.
11. ConWep, "Collection of conventional weapons effects calculations based on TM 5-855-1, Fundamentals of Protective Design for Conventional Weapons, U. S. Army Engineer Waterways Experiment Station", Vicksburg, VA, USA, 1992.
12. Janzon, B., "Grundläggande Stridsdelfysik (in Swedish)", C 20261-D4, FOA Rapport, Försvarets forskningsanstalt, Stockholm, Sweden, 1978, 164 pp.
13. Zielinski, A.J., "Fracture of concrete and mortar under uniaxial impact tensile loading", Doctoral Thesis, Delft University of Technology, 1982.
14. Richart, F.E., Brandtzaeg, A. and Brown, R.L., "A Study of the Failure of Concrete under Combined Compressive Stresses," *Bulletin* No. 185, University of Illinois, Engineering Experimental Station, Urbana, Illinois, USA, November 1928, 104 pp.
15. Bažant, Z.P., Xiang, Y.Y., Adley, M.D., Prat, P.C. and Akers, S.A., "Microplane Model for Concrete: II: Data Delocalization and Verification," *Journal of Engineering Mechanics-ASCE*, Vol. 122, No. 3, Mar 1996, pp. 255-262.
16. AUTODYN Manuals, "AUTODYN Manuals, Version 4.2", Century Dynamics, Inc. 2001, Sam Ramon, USA.
17. Bischoff, P.H. and Perry, S.H., "Compressive behaviour of concrete at high strain rates," *Materials and Structures*, Vol. 24, 1991, pp. 425-450.
18. CEB-FIB Model Code 1990, "CEB-FIB Model Code 1990, Design Code, Thomas Telford", Lausanne, Switzerland, 1993, 437 pp.
19. Ross, C.A., Jerome, D.M., Tedesco, J.W. and Hughes, M.L., "Moisture and strain rate effects on concrete strength," *ACI Materials Journal*, Vol. 93, No. 3, May-June 1996, pp. 293-300.
20. ACI Manual of Concrete Practice 2002, "ACI Manual of Concrete Practice 2002, American Concrete Institute, Farmington Hills, MI, USA, 2002.
21. Jonasson, T., "Kontaktverkan 1, Sprängladdningars kontaktverkan på armerade betongplattor", C 20809-2.6, FOA rapport, Sundbyberg, Sweden, 1990, 58 pp.
22. Forsén, R. and Edin, K., "Vapenverkan mot flervånings betongbyggnad III. Bestämning av skador från splitterladdningar mot husfasad i skala 1:4 (in Swedish)", C 20860-2.3, FOA report, Sundbyberg, Sweden, 1991, 40 pp.
23. Forsén, R. and Nordström, M., "Damage to Reinforced Concrete Slabs Due to the Combination of Blast and Fragment Loading (In Swedish)", B 20101-2.6, National Defence Research Establishment (FOA), Tumba, Sweden, 1992, 12 pp.